

**SEA ICE TRANSPORT THROUGH NARES STRAIT
BETWEEN 2003 AND 2012**

by

Patricia Anderson Ryan

A dissertation submitted to the Faculty of the University of Delaware in partial fulfillment of the requirements for the degree of Doctor of Philosophy in Marine Studies

Spring 2018

© 2018 Patricia Anderson Ryan
All Rights Reserved

**SEA ICE TRANSPORT THROUGH NARES STRAIT
BETWEEN 2003 AND 2012**

by

Patricia Anderson Ryan

Approved: _____
Mark A. Moline, Ph.D.
Director of the School of Marine Science and Policy

Approved: _____
Estella Atekwana, Ph.D.
Dean of the College of Earth, Ocean and Environment

Approved: _____
Ann L. Ardis, Ph.D.
Senior Vice Provost for Graduate and Professional Education

I certify that I have read this dissertation and that in my opinion it meets the academic and professional standard required by the University as a dissertation for the degree of Doctor of Philosophy.

Signed: _____
Andreas Münchow, Ph.D.
Professor in charge of dissertation

I certify that I have read this dissertation and that in my opinion it meets the academic and professional standard required by the University as a dissertation for the degree of Doctor of Philosophy.

Signed: _____
Helga S. Huntley, Ph.D.
Member of dissertation committee

I certify that I have read this dissertation and that in my opinion it meets the academic and professional standard required by the University as a dissertation for the degree of Doctor of Philosophy.

Signed: _____
I. Pablo Huq, Ph.D.
Member of dissertation committee

I certify that I have read this dissertation and that in my opinion it meets the academic and professional standard required by the University as a dissertation for the degree of Doctor of Philosophy.

Signed: _____
Mary Louise Timmermans, Ph.D.
Member of dissertation committee

I certify that I have read this dissertation and that in my opinion it meets the academic and professional standard required by the University as a dissertation for the degree of Doctor of Philosophy.

Signed: _____

Helen Johnson, Ph.D.
Member of dissertation committee

ACKNOWLEDGEMENTS

I'd like to thank all of the people who supported me throughout the process of completing this research. Most importantly, my husband who has been cheerleader, caretaker, proofreader and the most patiently supportive partner for whom anyone could ever hope. All three of my children (Sean, Briega and Jose) who make me feel loved and special always - but most especially, my daughter Briega who never doubted me; her ability to speed read through my drafts was incredibly helpful. The CATS science team who worked so hard to get the data behind this work, especially Humfrey Melling and Dave Riedel who answered many questions with patience and insight, often answering the question I should have asked in addition to the one I did. The crew of the Henry Larsen (CCGC), who oversaw our safety, during deployment and recovery of our instruments, their professionalism ensured our success and their attitude made it a pleasure to be at sea with them. The members of my dissertation committee who listened and guided, provided insight and encouragement; I hope they know how invaluable that has been. The students of Robinson 210 who actually made going back to school fun, especially Berit Rabe, Joseph Senne, Alex Davies, Joe Brodie and Peter Washam; there are too many to name them all but their ability to accept a "mature student" into their midst was heartwarming. Finally my advisor, Andreas Münchow whose patience I have tried on more occasions than I'm willing to admit and whose faith in me and support of me I will never be able to repay.

TABLE OF CONTENTS

LIST OF TABLES	ix
LIST OF FIGURES	x
ABSTRACT	xiv
 Chapter	
1 INTRODUCTION	1
1.1 Description of Nares Strait	3
1.2 A Nine Year Study of Nares Strait	6
1.3 Sea ice in Nares Strait	8
1.4 Research Questions	8
1.4.1 Outline of this dissertation	10
2 ICE OBSERVATIONS IN NARES STRAIT 2003-2012	12
2.1 Introduction	12
2.2 Methods	12
2.2.1 Ice draft	15
2.2.2 Ocean density and speed of sound	19
2.2.3 Atmospheric forcing	20
2.2.4 Quasi-Lagrangian frame	20
2.3 Time Series	21
2.3.1 Ice drafts and velocity	21
2.3.2 Seasonality	22
2.4 Ice Draft Distributions	26
2.4.1 Definition and sources	26

2.4.2	Near-decadal time scale	26
2.4.3	Annual time scales	27
2.4.4	Across-channel variability	31
2.4.5	Thick ice	34
2.5	Ice Bridge Control and Implications	35
2.5.1	Impacts of land-fast seasons	36
2.5.2	Free-flow ice years	37
2.6	Discussion and Conclusions	38
2.7	Appendix A: Error Sources and Ice Draft Sensitivity	41
2.8	Appendix B: Atmospheric Model	46
2.9	Appendix C: Spatial Domain Derivation	46
3	A SEMIANALYTIC MODEL OF CHANNEL FLOW	48
3.1	Introduction	48
3.1.1	Observations	49
3.2	Model	53
3.2.1	Geostrophic solution	55
3.2.2	Wind stress solution	56
3.3	Adding an Ice Cover to the Model	57
3.4	Applying the Model to Nares Strait	58
3.4.1	Parameterization	58
3.4.2	Run 1	59
3.4.2.1	Low viscosity	59
3.4.2.2	High viscosity	61
3.4.3	Run 2	62
3.4.4	Run 3	62
3.4.5	Run 4	64
3.4.5.1	High viscosity	67
3.4.5.2	Low viscosity	67
3.5	Conclusions	67

4	ICE FLUX THROUGH NARES STRAIT 2003-2009	71
4.1	Introduction	71
4.2	Data Methods	72
4.2.1	Ice flux and volume transport	72
4.3	Across-channel Variability	74
4.3.1	Ice draft	74
4.3.2	Ice velocity	74
4.3.3	Piece-wise linear velocity profile	75
4.4	Ice Flux	76
4.4.1	Analysis	76
4.5	Conclusion	81
5	DISCUSSION OF FINDINGS	83
5.1	Ice Draft and Velocity	83
5.2	Multi-year Ice Trends	83
5.3	Semianalytic Model of Channel Flow	84
5.4	Ice Flux	84
5.5	Conclusion	85
5.6	Future Work	85
	BIBLIOGRAPHY	87

LIST OF TABLES

2.1	Instruments by deployment.	14
2.2	Landfast season characteristics	24
3.1	Parameter values for model runs.	60
4.1	Ice transport statistics.	81

LIST OF FIGURES

1.1	Map of Canadian Arctic Archipelago with enlargement of Nares Strait	4
1.2	MODIS images of surface temperature in Nares Strait during each winter season between 2003 and 2012. Ice bridges near 83°N and 79°N appear as cold arches adjacent to a relatively warm zone that lies just south of them with temperature gradients larger than 20°C.	5
1.3	Original mooring deployment in cross-section of Nares Strait at 80.5° N.	6
2.1	Mooring Locations. a) Map of Nares Strait, b) inset map showing details for Kennedy Channel section where dark lines spanning the channel indicate the mooring locations. Panels c) thru f) show a cross section view of the channel and moored instruments of each deployment which were used to derive ice draft and velocity in this chapter. Note that the 2009-2012 deployment was located north of those in previous years and the IPS instrument was raised from 100 m to 75 m depth.	13
2.2	IPS mooring configuration.	16
2.3	Ice draft cartoon. Ice is located at A, its intercept point is at a distance R and an angle α to the IPS. B is directly above the IPS. .	17
2.4	Probability distribution of all observations during the month of August. Dotted black line shows a Gaussian distribution with zero mean and standard deviation = 0.1m.	19
2.5	Draft observations on 1 April 2004 (15 second interval). Gray lines show mean (solid), \pm one standard deviation of observations (short dashes), and \pm our error estimate (long dashes).	20
2.6	Bottom topography of ice measured on 8 August, 2005 from 4:00 to 4:45 GMT. Near zero values indicate open water.	21

2.7	Left column shows daily median ice drafts at KS30 (2003-07), KS25 (2007-09) and KF30 (2009-12). Right column shows along-channel ice velocities nearest these stations. Negative velocities are southward. Gray shading indicates fast-ice periods as defined in section 2.3.2.	23
2.8	Mean of daily ice draft statistics, 5th percentile, median and 95th percentile, during the months of September, October and November for each year.	25
2.9	Cumulative percentages of ice observations for all years. The distribution is adjusted for ice velocities and, therefore, the 2006-07 ice year is excluded.	28
2.10	Ice volume fraction by draft. Each bin spans 0.1 m and the percent shown is the relative volume of ice. The distribution is adjusted for ice velocities and, therefore, the 2006-07 ice year is excluded.	28
2.11	Annual probability distribution of ice drafts as a percent of all ice by year (adjusted for velocity). Bins are in 0.1 m increments. Inset at upper right provides statistics of the annual distributions. Note that the 2006-07 ice year is not included as velocity data are unavailable.	29
2.12	Cumulative probability distribution of ice drafts shown in Figure 2.11. Black symbols are associated with early record (2003-2006) and white symbols with later period (2009-2012).	30
2.13	Annual ice volume fraction by draft. Each bin spans 0.1 m and the percent shown is the relative volume of ice. The distribution is adjusted for ice velocities. The inset at the top is a chart of the modes and the median of each distribution.	32
2.14	Probability distribution of ice at KS20 (black line) compared to ice at KS30 (gray shade). Inset chart shows 5th, 50th and 95th percentile for each of these distributions.	33
2.15	Ice velocity at KS20 (black) compared to KS30 (blue).	34
2.16	Distribution of thick ice on a log-linear graph (large graph). Symbols indicate observation year. Inset graph shows the <i>e</i> -folding scale of the analytic function for each year's ice distribution.	35

2.17	Water column characteristics for 2003-09. Depth averaged density and speed of sound for the upper 100 m of the water column from CT/D moorings adjacent to IPS (blue: west, black: east).	43
2.18	Water column characteristics for 2009-12. Depth averaged density and speed of sound for the upper 75 m of the water column derived from CT/D moorings adjacent to IPS (blue: west, black: east). . .	44
2.19	Salinity and temperature measurements from 10 hourly CTD casts performed adjacent to KS09 on 22 August 2007.	45
3.1	Reproduction of the 2 flow regimes in Nares Strait from Rabe et al. [2012] . Sections of mean geostrophic velocity at seasonal timescales during each (a) mobile-ice and (b) fast-ice season. Zero geostrophic velocity is denoted in white and positive velocities are to the south [cm s^{-1}]. Each black triangle denotes the horizontal position of a midpoint between two density profiles; the vertical resolution is 1 m. The contour interval is 2 cm s^{-1}	50
3.2	Observations of flow in Nares Strait. Average annual along-channel flow velocity for 2008 (A), the third day of a period of strong up-channel winds (B) and the second day of very strong down-channel winds (C).	52
3.3	Observations of flow in Nares Strait during land-fast ice season of 2008-09.	53
3.4	Coordinate system for model domain. Dotted line (positive x) is out of the page.	54
3.5	Run 1 - Modeled geostrophic velocities. Ekman depth is 12 m (top) and 350 m (bottom).	61
3.6	Scatter plot for wind velocity.	63
3.7	Profile of wind stress applied to the model to account for the canyon-like geometry of Nares Strait.	64
3.8	Run 2 - Modeled velocities with wind effects and amplified drag coefficient for open water. Windspeed is 4.3 m s^{-1} from the North (A) and 5.4 m s^{-1} from the south (B). These are the average along-channel wind velocities during the observation periods for the respective panels of Figure 3.2	65

3.9	Run 3 - Modeled velocities with wind effects amplified drag coefficient for rough ice. Windspeed is 4.3 m s^{-1} from the North (A) and 5.4 m s^{-1} from the south (B). These are the average along-channel wind velocities for the respective panels of Figure 3.2.	66
3.10	Run 4 - Modeled velocities for a land-fast ice cover. Ekman depth is 350 m (A) and 70 m (B).	68
3.11	Schematic cross-section of a coastal upper layer flow of speed u (out of the page) driven by a sea-surface slope $\eta(y)$; the lower layer, of density ρ_2 is at rest because the interface $h(y)$ slopes in a direction opposite to that of the free surface. y_0 is the distance from the coast at which the thickness of the upper layer vanishes. [LeBlond, 1980].	69
4.1	Cross-section of Nares Strait with symbols showing location of the IPS and ADCP moorings between 2003-2006.	73
4.2	Cross-section of Nares Strait with symbols showing location of the IPS and ADCP moorings between 2007-2009.	73
4.3	Mean ice velocity during free flow ice periods 2003-06 (red) and 2006-09 (blue). Black symbols indicate mean velocity assumption between 2003 and 2006. Dotted lines connect observations separated by more than 6 km.	75
4.4	Ice flux through Nares Strait from 2003 to 2006 and from 2007 to 2009. A low-pass Lanczos filter was applied (~ 30 days half-power point). Positive values are down-channel outflows.	79
4.5	Annual ice transport through Nares Strait from 2003 to 2006 and from 2007 to 2009. My estimates (red) are compared to those of Kwok et al. [2010] (blue).	80

ABSTRACT

This dissertation focuses on sea ice observations in Nares Strait between 2003 and 2012. Ice transported via the channel contributes to freshwater flux through the Canadian Arctic Archipelago (CAA). Nares Strait, which forms the eastern boundary of the CAA, is second only to Fram Strait for volume outflow from the Arctic basin. Flow through the channel is described by two regimes. The distinction between these is the presence or absence of a land-fast ice bridge blocking ice transport. During the beginning and end of this study, ice bridges form each year and last for 3 to 6 months. However, ice flows virtually uninhibited for four years beginning in 2006. Data gathered from ice profiling sonars (IPS) moored in the channel are used to measure ice draft. Ice is found to be thicker in the western channel and to have highest velocity in the central channel. The statistical distribution of ice is assessed at seasonal and inter-annual scales temporally. Whereas ice in the Arctic Basin has been thinning, thick multi-year ice continues to flow through Nares Strait. With a goal to estimate ice volume flux through the channel, use of a steady state semianalytic channel flow model to supplement spatial and temporal gaps in ice velocity data is evaluated. Specifically, its ability to reproduce geostrophic flow characteristics and surface velocities in a cross-section of Nares Strait is assessed by comparison to well-resolved observational data. Surface forcing due to winds, the presence of mobile ice and land-fast ice cover conditions are implemented in the model. In order to replicate ice velocity at the water surface, the model requires extreme values for viscosity and amplified drag coefficients. A time series of ice flux is finally derived. Annual ice volume transport through Nares Strait averages 171 ± 62 km³ when an ice bridge blocks the channel as compared to 472 ± 126 km³ when ice flows freely year-round. Thus, Nares Strait transports between 6 and 21% of the volume of ice transported by Fram Strait.

Chapter 1

INTRODUCTION

Arctic sea ice influences global climate. Since the albedo of sea ice is ten times that of open water, the reflective property of sea ice reduces the amount of solar energy that can be absorbed by the ocean it covers. Thus loss of a perennial ice cover exposes the underlying ocean and results in increased warming. Multi-year ice (MYI), that forms the perennial Arctic ice cover is measured by both areal extent and thickness. Annual minimum Arctic sea ice extent records were broken in 2005 [Comiso and Nishio, 2008], 2007 [Stroeve et al., 2008] and again in 2012 [Laxon et al., 2013]. Since increased ice-free areas provide a mechanism for positive climate feedback, this fueled concerns about an ice-free Arctic. Global climate models predict an ice-free summer before 2100 [Kay et al., 2011, Meehl et al., 2012, Stroeve et al., 2012, Vavrus et al., 2012]. Whereas satellite data provide information on extent of the ice, measurements of ice thickness via remote sensing is less precise. In-situ ice thickness measurements provide crucial data to validate models and may lead to better estimates of the time it will take for the Arctic to become free of MYI.

Ice observations are achieved by various methods. These range from drilling through ice to measure its properties directly at a single point [Johnston, 2014, Eicken and Lange, 1989] to utilizing remotely sensed satellite data which provide estimates of surface properties including sea ice area over vast regions [Stroeve et al., 2012]. Along survey tracks, submarine acoustic studies provide ice thickness from below [Wadhams et al., 1979, Blidberg et al., 1981, Bourke and Garrett, 1987], and electromagnetic devices, such as laser altimeters and radars, aboard helicopters and fixed wing aircraft measure this property from above [Haas et al., 2006, Farrell et al., 2012, Kurtz et al., 2013]. Others use discretely moored ice profiling sonars to measure ice thickness from

below as time series [Melling and Riedel, 1995]. It is this method that will be presented herein.

Satellite data, collected since 1978, demonstrate the rapidly declining Arctic sea ice extent [Stroeve et al., 2012]. However, sea ice loss is not restricted to reduction in areal coverage. Observations indicate that the perennial ice cover that remains in the Arctic has also been thinning. This thinning is documented using varied methods including satellite altimeters, submarine and moored sonar measurements, satellite microwave sensor data and electromagnetic instruments [Kwok et al., 2009, Shibata et al., 2013, Renner et al., 2014]. Perovich et al. [2014] and Kwok and Cunningham [2010] attribute this thinning to melting of multi-year ice. An increased export of MYI from the Arctic could also lead to thinner perennial Arctic ice cover.

Studies have focused on the relationship of atmospheric conditions on ice motion in the Arctic Basin. Thorndike and Colony [1982] find that in time scales of days to weeks, more than 70% of the variance in ice motion is explained by local geostrophic winds. Vihma et al. [2012] determined that a large part of the inter-annual variance of ice velocity is explained by atmospheric forcing. They identify Central Arctic Index, that is the sea level pressure difference between 270°E and 90°E at 82°N as the most relevant circulation index. When the index is high, strong geostrophic winds drive ice motion along the Transpolar Drift Stream (TDS), whereas when it is low, weaker geostrophic winds drive ice motion from the Central Arctic towards the Canadian Arctic. However, Thorndike and Colony [1982] found that none of the variance in divergence was attributable to local geostrophic winds. Kwok et al. [2013] finds that recent increases in drift speed are related to changes in ice thickness rather than wind forcing. Screen et al. [2011] associates the cyclones of late spring/early summer with variability in the perennial ice cover at the fall minimum. They suggest that cyclones have preconditioning effects on the ice and found large decreases in MYI when cyclone activity in the central Arctic is low.

Ice advects from the Arctic Ocean to the North Atlantic Ocean via two pathways. These are Fram Strait to the east and the CAA to the west of Greenland. Past

observations indicate that Fram Strait dominates ice export year-round [Aagaard and Carmack, 1989], while the thickest ice may leave the Arctic via the CAA. For Fram Strait, Hansen et al. [2013] analyzed trends in ice advection with moored sonars since 1990. They found no increased advection of ice with thickness above 5 m; in fact, their study revealed that the ice leaving the Arctic via Fram Strait has been thinning. However, Bourke and Garrett [1987] found the thickest ice in the Arctic to the north of the CAA from submarine surveys. This finding was confirmed by Haas et al. [2006] and Maslanik et al. [2007] who found thickening of ice in the region adjacent to the CAA, as well as by Kwok and Cunningham [2016] who found the area covered by thick ice to have increased. This study relates to the advective flux of this thick Arctic ice to the south through Nares Strait. Whereas previous estimates of ice flux through the channel have relied on remote sensing [Kwok, 2005, Kwok et al., 2010], discretely moored ice profiling sonars were used to record the data presented in this work. These observations will increase understanding of ice transport through Nares Strait in a changing Arctic climate.

1.1 Description of Nares Strait

Nares Strait is a 500 km long channel which connects the Arctic Ocean in the north to Baffin Bay in the south between Ellesmere Island and North Greenland (Figure 1.1). Steep orography channels the atmospheric flow that is generally along the strait from north to south [Samelson et al., 2006]. Winds impact the advection of ice [Samelson et al., 2006] as does the ocean circulation [Münchow and Melling, 2008, Münchow, 2016]; however, ice motion ceases at our mooring location after an ice arch forms at the southern end of Nares Strait [Dumont et al., 2009], as it does in most years. Thermal imaging, such as Figure 1.2, reveals these ice arches as strong temperature gradients between thin ice or water (warm) and thicker ice (cold) [Vincent et al., 2008]. Such ice arches form each winter at many locations throughout the CAA [Smith et al., 1990]. After the ice in Nares Strait is blocked, open water or thin ice covers a large area to the south of it as winds continue to advect newly formed ice into

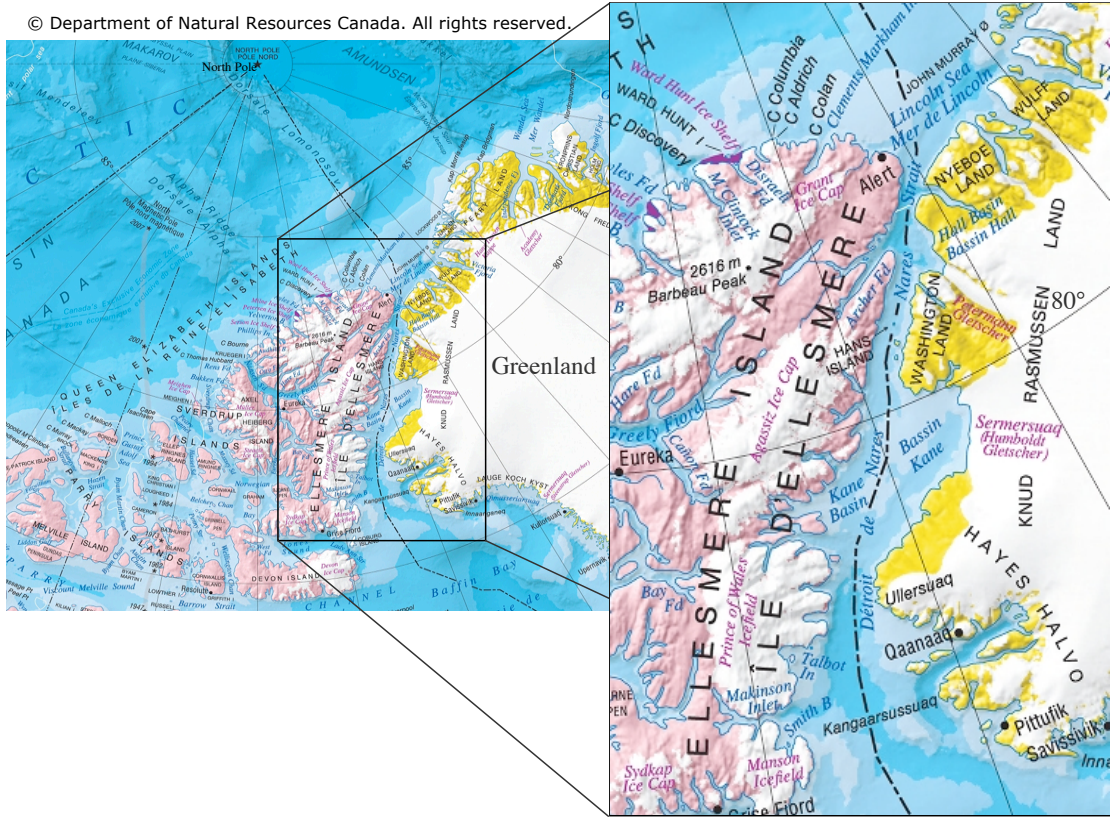


Figure 1.1: Map of Canadian Arctic Archipelago with enlargement of Nares Strait

Baffin Bay south of the arch and a latent heat polynya forms [Melling et al., 2001]. This so-called North Water polynya exhibits high biological productivity [Dunbar and Dunbar, 1972]. Evidence of formation of this polynya for at least the last 800 years lies in viking artifacts dating to the 12th century found at Inuit settlements near Smith Sound [Schledermann, 1980]. Using airborne radar, Dunbar [1973] documented the formation and spatial extent of this polynya in 1971 and 1972. Preußer et al. [2015] analyzed the characteristics of the polynya between 1978 and 2015 with remotely sensed data. Kwok et al. [2010] summarizes formation and duration of all Nares Strait ice arches from 1997 to 2007, while Figure 1.2 shows the spatial surface temperature distribution for a typical day for each year that we analyze in this study.

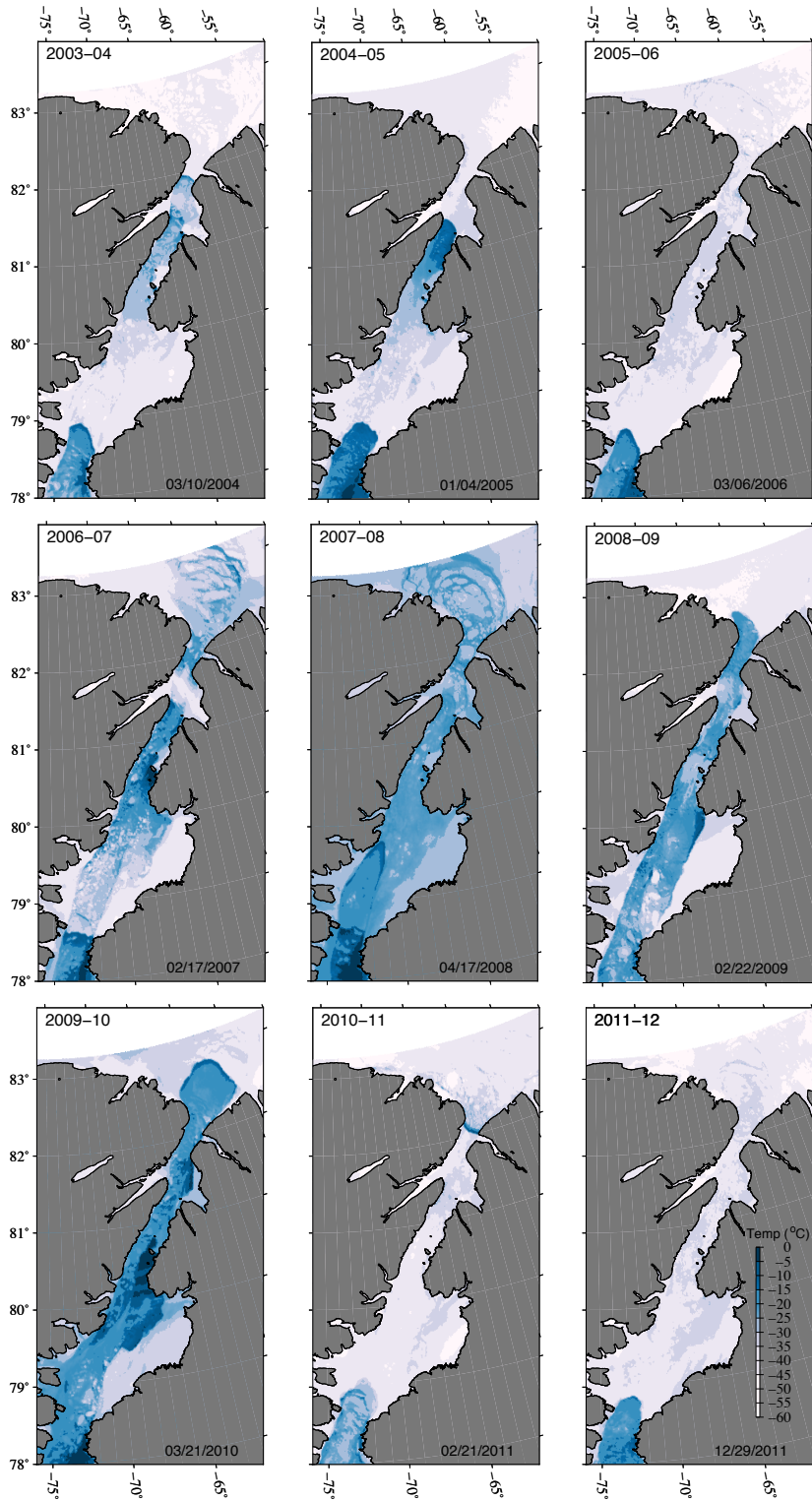


Figure 1.2: MODIS images of surface temperature in Nares Strait during each winter season between 2003 and 2012. Ice bridges near 83°N and 79°N appear as cold arches adjacent to a relatively warm zone that lies just south of them with temperature gradients larger than 20°C.

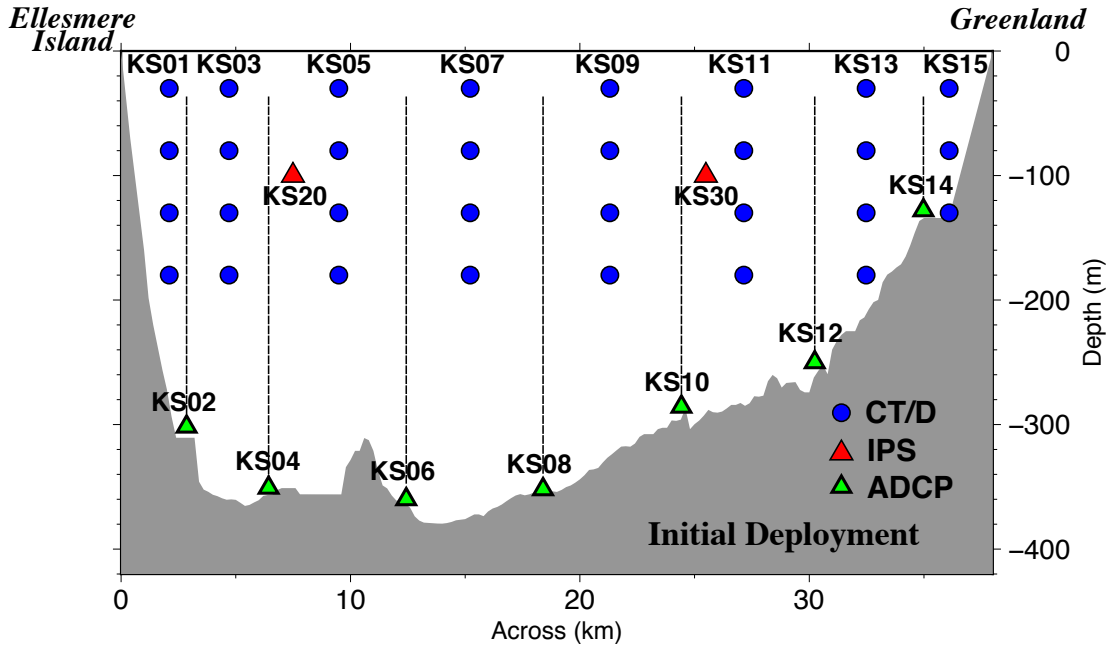


Figure 1.3: Original mooring deployment in cross-section of Nares Strait at 80.5° N.

1.2 A Nine Year Study of Nares Strait

In 2003, an international group of scientists initiated the observational research project known as the Canadian Archipelago Throughflow Study (CATS). They sought to explore the effects of remote and local forces on the dynamical response in Nares Strait. Moored instruments to record data about water and ice flowing through the channel were deployed for several years at a time. They were periodically recovered to capture the data and then were redeployed to chronicle conditions in Nares Strait through 2012.

The moored instruments included acoustic Doppler current profilers (ADCP) to measure velocities, probes to monitor conductivity (as a proxy for salinity), temperature, and depth (CTD), and ice profiling sonars (IPS) to measure ice drafts. Figure 1.3 shows the layout of the moorings that spanned the channel for the first deployment. Additionally, tide gauges were deployed in inlets to measure along-channel pressure gradients in the channel [Münchow and Melling, 2008].

Observations obtained via ship-based instruments provided insights to flow

through Nares Strait. For example, [Münchow et al. \[2006\]](#) utilized observations gathered during the first deployment cruise to estimate total and freshwater flux through the channel. They found these values to be 0.8 ± 0.3 Sv and 25 ± 12 mSv respectively. While [Münchow et al. \[2007\]](#) used chemical analysis of water samples collected to determine that 39% of this volume was of Pacific origin.

While the prior findings are based on data collected over days to weeks and may be specific to that time or season, moored instruments provide a record spanning multiple years. They therefore record data which allow variability from tidal to inter-annual scales to be explored. [Münchow and Melling \[2008\]](#), introduced the time series from moored ADCPs. They found mean volume water transport through the channel below 30 m depth to be 0.57 ± 0.09 Sv and to vary seasonally by 30 to 50%.

[Rabe et al. \[2010\]](#) utilized a novel approach to derive properties in the channel. By exploiting vertical movement of CTDs they derived a two-dimensional field of temperature and salinity. That lead to estimates of geostrophic flow between 2003 and 2006 [[Rabe et al., 2012](#)]. Over the first six years of the deployment, [Münchow et al. \[2011\]](#) identified a near-bottom warming trend between 2003 and 2009. Finally, [Münchow \[2016\]](#) provided volume and freshwater flux as well as ice velocities from ADCPs. Without the latter, this work would not have been possible.

Modeling efforts have shed light on characteristics of Nares Strait like wind velocity and atmospheric pressure and temperature at regional scales. Among these, [Samelson et al. \[2006\]](#) analyzes the relationship between modeled winds and ice motion derived from satellite data during 2004. One of these periods lasted 30 days and the other 45 days. They found ice flux through the Strait to be controlled by wind stress and atmospheric cooling. While [Samelson and Barbour \[2008\]](#) documents a regional atmospheric model for Nares Strait. This model simulates the strong along-channel winds and provides atmospheric pressure utilized herein. Models have also been used to study ice and ocean dynamics in the channel [[Rasmussen et al., 2010, 2011, Shroyer et al., 2015](#)].

Previous studies of the ice of Nares Strait have relied on remote sensing that

provides ice extent at scales of 100s of meters to kilometers. The focus of long-term studies has been on the ice that enters the channel through the Lincoln Sea. Prior to my work, no analyses were published with the data provided by the ice profiling sonars deployed by the CATS team in 2003. I herein provide the time series of ice drafts recorded over nine years at frequencies of four to ten per minute. I analyze statistical properties of the ice in both time and space. To accomplish this, I developed an algorithm for ice draft calculation and implemented it in Fortran. The calculation of draft requires signal return times recorded by the IPS as proxies for distances, instrument pressure, pitch and roll, atmospheric pressure, concurrent speed of sound derived from in-situ CTDs, and ice velocities from moored ADCPs [Ryan and Münchow, 2017]. The algorithm is described in Chapter 2 of this work.

1.3 Sea Ice in Nares Strait

To add to the understanding of the role of Nares Strait in the context of Arctic processes, I focus attention on the ice that passes through the channel. The CATS data set provides an unprecedented opportunity to study the channel under variable ice conditions. The record includes winters with up to six months of ice flow cessation due to land-fast ice as well as a three year period when no persistent ice arch formed to block the channel, resulting in year-round free-flowing ice.

1.4 Research Questions

With this observational data, my research seeks to answer the following questions.

- How thick is the ice that flows through Nares Strait during our nine year study and how does it change seasonally?

Ice profiling sonars moored in Nares Strait provide a time series of ice draft measurements over nine years. As the first study of the data gathered by ice profiling sonars, I present the time series of ice draft observations.

- Are there any temporal trends evident in observations of multi-year ice?

The loss of multi-year ice in the Arctic is a source of concern among climate scientists. I analyze time series of ice draft observations in the channel to find temporal trends. Since ice velocity varies seasonally and inter-annually, I will employ seasonal matching and a quasi-lagrangian approach to remove velocity bias that would otherwise skew the data.

- How does the presence of a land-fast ice cover affect water flow in the channel?

Nares Strait is usually covered by land-fast ice for several months each year. This serves to uncouple the water flowing through the channel from the atmospheric forcing above. I implement an analytic model to study the effects on flow structure in the channel when it is covered by stationary ice as compared to when wind stress is applied to the water's surface.

- Can I replicate ice velocity in Nares Strait with an analytic model?

During one year of our study, there is no ice velocity data available. In another there is an 18 km gap in the central channel between ADCP moorings. If I can adequately model surface velocities under wind stress conditions with the model, I can substitute ice velocity observations with model output to find ice flux during these periods.

- How much ice passes through Nares Strait?

Nares Strait, a comparatively narrow channel, is generally parameterized rather than explicitly modeled in global climate models. Better estimates of ice transport will inform modelers and help improve their predictions. To this end, I estimate ice flux and annual volume transport from high frequency measurement of ice drafts and velocity in Nares Strait.

- How does ice transport through Nares Strait compare to that of Fram Strait?

To place ice flux through Nares Strait into a larger context, I will compare ice flux through the two primary outflow paths for ice from the Arctic basin.

- What is the impact on ice flux through Nares Strait when ice flows freely year-round?

The prolonged period of free flow between 2006 and 2009, when ice arches were absent from the channel, presents an opportunity to examine the role of Nares Strait’s ice bridges in constraining ice transport. I use estimates of ice flux and volume transport to answer this question.

1.4.1 Outline of this dissertation

I first present ice draft observations and analysis of how they vary in time and space. This is based on work published as [Ryan and Münchow \[2017\]](#). Ice profiling sonars deployed in Nares Strait between 2003 and 2012 measured the sound wave return time from the bottom ice surface. Implementing original programs, I derive the ice draft, that is ice depth below the water surface. I claim ice draft accuracy of 0.1 m. This is achieved by using contemporaneously deployed CTDs which provide frequent temperature and salinity measurements, yielding sound speed in the water column that is critical to ice draft calculation. To remove velocity bias that would result in the temporal domain, I derive statistical properties of ice using a quasi-lagrangian approach. This facilitates inter-annual comparisons of ice distributions and trend analysis. The technique employs ice velocities derived from ADCPs moored adjacently.

Initial work involved study of channel flow using a steady-state semianalytical model. Chapter 3 introduces an implementation of this model of a channel with wind stress forcing based on work by [Kasai et al. \[2000\]](#), [Valle-Levinson et al. \[2003\]](#), [Valle-Levinson \[2008\]](#), and [Reyes-Hernandez and Valle-Levinson \[2010\]](#). The model provides a velocity profile for a two dimensional channel cross-section with Nares Strait’s surveyed bathymetry. The model is modified to reflect the impact of strong along-channel winds typical of the Nares Strait in a method similar to [Huntley and Ryan \[2018\]](#). A land-fast ice cover is also implemented in the model.

In Chapter 4, I use ice draft and velocity observations to estimate ice flux and volume transport during two multi-year mooring deployments in Nares Strait. I exploit optimized spatial distributions of the observations from each deployment to inform and improve flux derivation during the other.

The final chapter summarizes my findings to the questions posed above. I also present suggestions for future work.

Chapter 2

ICE OBSERVATIONS IN NARES STRAIT 2003-2012

2.1 Introduction

Here I present the ice draft time series recorded by ice profiling sonars deployed throughout the Canadian Archipelago Throughflow Study. I examine the seasonal, inter-annual and across-channel variability of ice draft distributions, the impact of the presence of wintertime ice bridges and associated polynyas as well as temporal trends in these distributions, specifically of thick MYI. The remainder of this chapter is based largely on [Ryan and Münchow \[2017\]](#).

2.2 Methods

Starting in 2003, we deployed an array of instruments in Nares Strait (Figure 2.1). Final recovery of the instruments occurred in August 2012. Figure 2.1 (Panels c through f) illustrate the cross-sectional distribution of sensor systems we will use to estimate ice draft for each deployment period. Since ice in the channel is at its lowest level in August, recoveries/redeployments occurred during that month. This results in data gaps of varying lengths during August. We therefore define an ice year as the period from 1 September through 31 July for inter-annual comparisons. Our study period covers nine ice years.

The instruments deployed included acoustic Doppler current profilers (ADCP) to measure water and ice velocity vectors [[Münchow, 2016](#)], conductivity, temperature, and depth profilers (CT/D) to measure temperature, salinity and pressure [[Rabe et al., 2010](#)], and ice profiling sonars (IPS) to measure ice drafts [[Melling et al., 1995](#)]. Table 2.1 lists salient details of the instruments used.

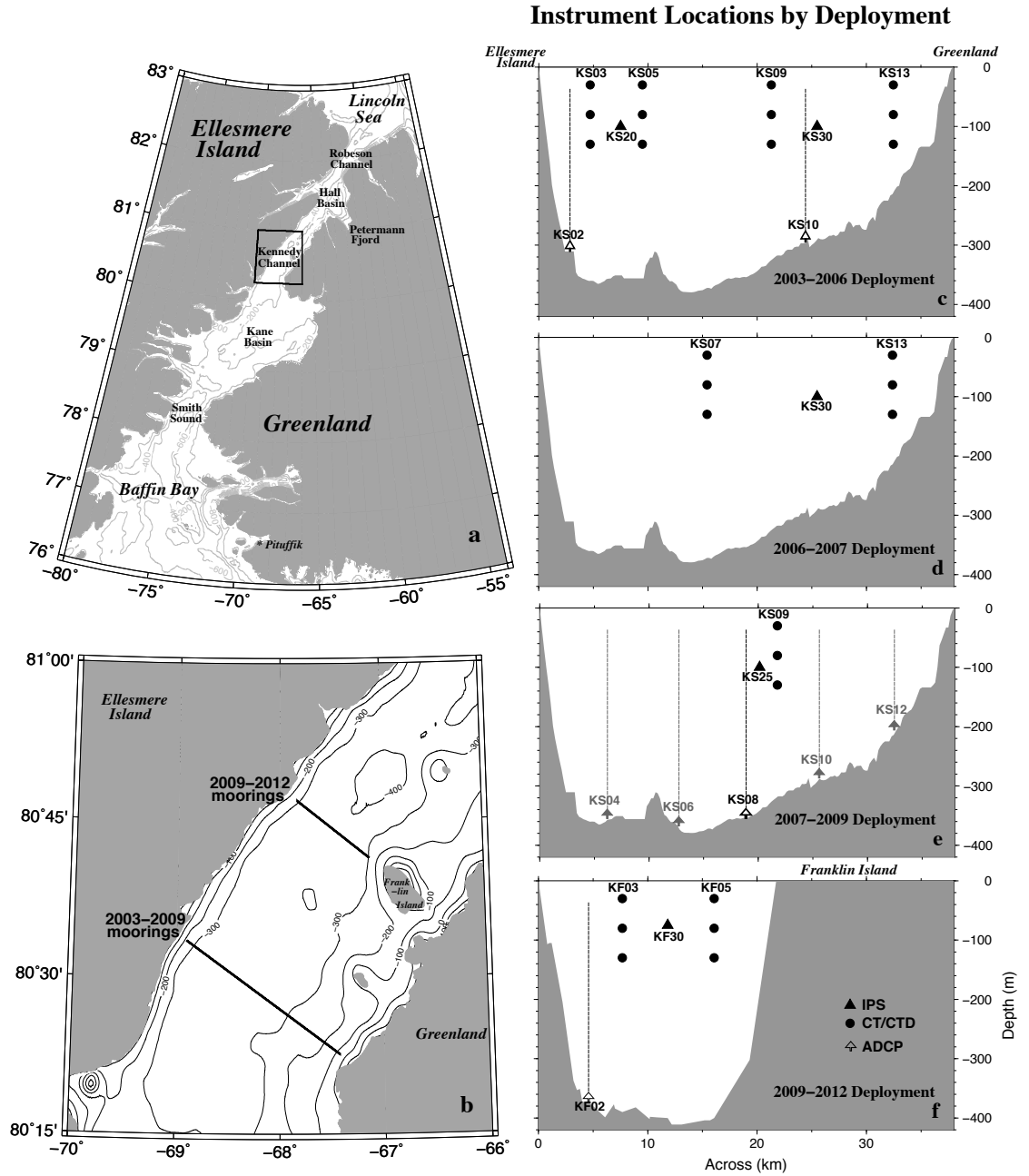


Figure 2.1: Mooring Locations. a) Map of Nares Strait, b) inset map showing details for Kennedy Channel section where dark lines spanning the channel indicate the mooring locations. Panels c) thru f) show a cross section view of the channel and moored instruments of each deployment which were used to derive ice draft and velocity in this chapter. Note that the 2009-2012 deployment was located north of those in previous years and the IPS instrument was raised from 100 m to 75 m depth.

2.2.1 Ice draft

We estimate ice draft from sonars manufactured by ASL Environmental Sciences Inc. (Model 4) at locations we refer to as KS20 and KS30 (2003-07), KS25 (2007-09) and KF30 (2009-12). Figure 2.2 shows the mooring design that consists of an anchor below two Teledyne Benthos Inc. 866A acoustic releases, external battery cases, and three subsurface steel floats. The sounder is attached to the top float at a nominal depth of 100 m between 2003 and 2009 or 75 m between 2009 and 2012.

The sonar sends acoustic pulses into the water column and measures the time for them to return. Most energy is reflected from the water-ice or, in the absence of ice, the water-air interface. At nominal depth, the narrow angle of the IPS sonar results in a footprint of 7.7 m² between 2003 and 2009 or 4.4 m² between 2009 and 2012 at the water surface. The measured travel time is converted to a distance R to the interface, provided the speed of sound is known. This distance from the sonar to the interface is then converted to an ice draft D provided the vertical location η and beam orientation α of the sonar are known (Figure 2.3).

The IPS also measures pressure with a Paroscientific Inc. 2200A-101 as well as pitch and roll with an Applied Geomechanics Model 900 unit.

Assuming a constant speed of sound $SS_a=1440$ m s⁻¹, the IPS records the measured 2-way travel time t as range R_{IPS} , i.e.,

$$R_{\text{IPS}} = SS_a * t/2 \quad (2.1)$$

The true range R requires the true speed of sound SS , the derivation of which we describe in the next section. That is, we apply a correction factor

$$\beta = SS/SS_a \quad (2.2)$$

to find the true range

$$R = \beta R_{\text{IPS}} \quad (2.3)$$

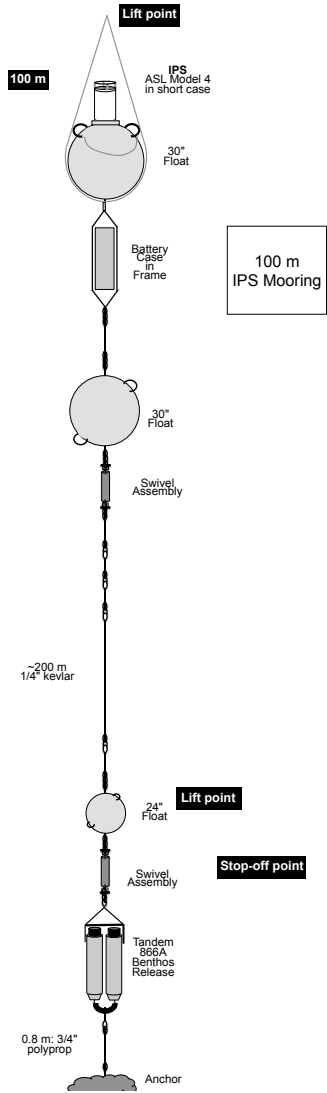


Figure 2.2: IPS mooring configuration.

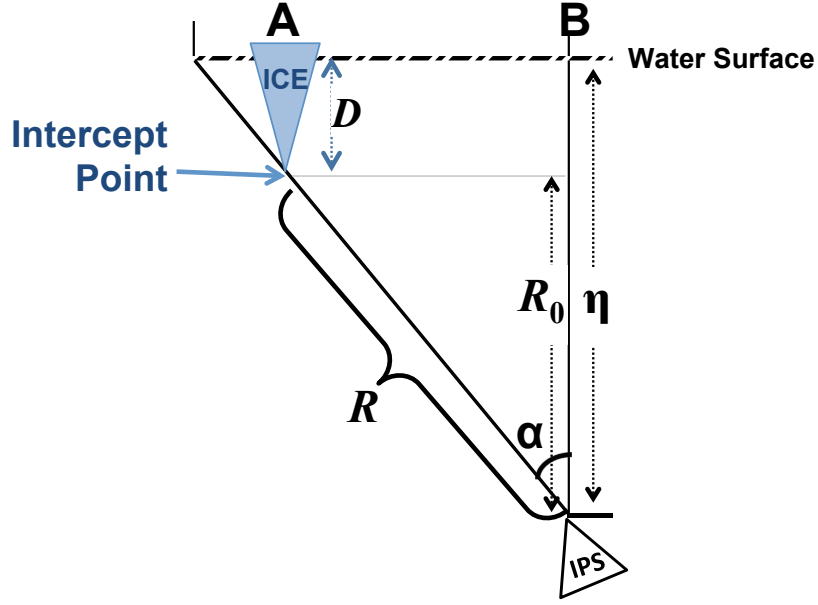


Figure 2.3: Ice draft cartoon. Ice is located at A, its intercept point is at a distance R and an angle α to the IPS. B is directly above the IPS.

Furthermore, we correct for the measured sensor tilt $\alpha = (\text{tilt}_x^2 + \text{tilt}_y^2)^{\frac{1}{2}}$, where tilt_x and tilt_y are the pitch and roll measured by the IPS. Hence we determine the vertical distance from the sonar to the reflecting interface R_0 as

$$R_0 = R \cos(\alpha) \quad (2.4)$$

Finally the draft D of the ice is defined as (Figure 2.3)

$$D = \eta - R_0 \quad (2.5)$$

where the water level

$$\eta = (P_I - P_a)/(\rho * g) + d_t \quad (2.6)$$

and P_I is the pressure measured at the IPS, P_a is atmospheric pressure, ρ is the depth averaged density of the water column above the instrument, g is the acceleration due to gravity and $d_t = -0.066$ m is the distance from the transponder to the pressure

gauge on the IPS.

Pitch, roll, and pressure were sampled at 60 second intervals. The range, however, was recorded at intervals of 3 seconds for August through January and 5 seconds for February through July from 2003 to 2009 while from 2009 to 2012 we chose recording intervals of 2 seconds for July through January and 3 seconds for February through June. When deployments exceeded two years, ranges were recorded at the longer time interval of said deployment.¹ This variable time step was intended to conserve power and data storage on the premise that ice velocities are higher during mobile versus land-fast ice seasons. We subsampled these data to a uniform 15 second sampling for the 2003-09 deployments and 6 second sampling for the 2009-12 deployment using linearly interpolated tilt and pressure values to the frequency of the IPS range measurement.

In Section 2.7 we describe our error budget which shows our ice draft estimates to be accurate to within a standard deviation of 0.1 m or about 0.1% of the range measurement. In order to achieve this accuracy we used daily vertical temperature and conductivity profiles from concurrent, nearby mooring locations (Table 2.1) to estimate the true speed of sound, (SS). We exploit the relatively high occurrence of open water during the month of August to assess these methods. Figure 2.4 shows the probability distribution of August observations as well as the number of days for which data are available that month. If all observations were open water, we would expect to see a normal or Gaussian distribution centered at the 0 m draft bin. The black outline in the figure shows a Gaussian distribution represented by the formula

$$f(x|\mu, \sigma) = \frac{1}{\sqrt{2\sigma^2\pi}} e^{-\frac{(x-\mu)^2}{2\sigma^2}} \quad (2.7)$$

where the mean $\mu = 0$ m and the standard deviation $\sigma = 0.1$ m. Since there is still some ice in the channel, there is additional overlay of ice for the period. As one would expect variability about the mean of zero during periods of open water due to surface

¹ Between August 2005 and January of 2006 and between August 2008 and January 2009 range was recorded at 5 second intervals. Between July 2011 and January 2012 range was recorded at 3 second intervals.

waves, we are well within our error estimate. Figure 2.5 shows draft observations for an entire day, 1 April 2004. This is a representative period during the land-fast ice season when the scale of variability in ice drafts should be limited to the roughness of the ice that is stationary over our instruments. We find that the ice drafts vary between 0.72 and 0.93 meters with a mean of 0.88 m and a standard deviation of 0.03 m. This again is well within our error estimate.

Figure 2.6 shows the bottom topography derived from ice draft observations on 10 August 2005 between 4:00 and 4:45 GMT. We convert time to distance as described in Section 2.2.4, below. During this time, ice of drafts exceeding 10 meters passed our instruments after a period of open water. As we measure sea surface during these open water periods the draft observations are within a few centimeters of zero.

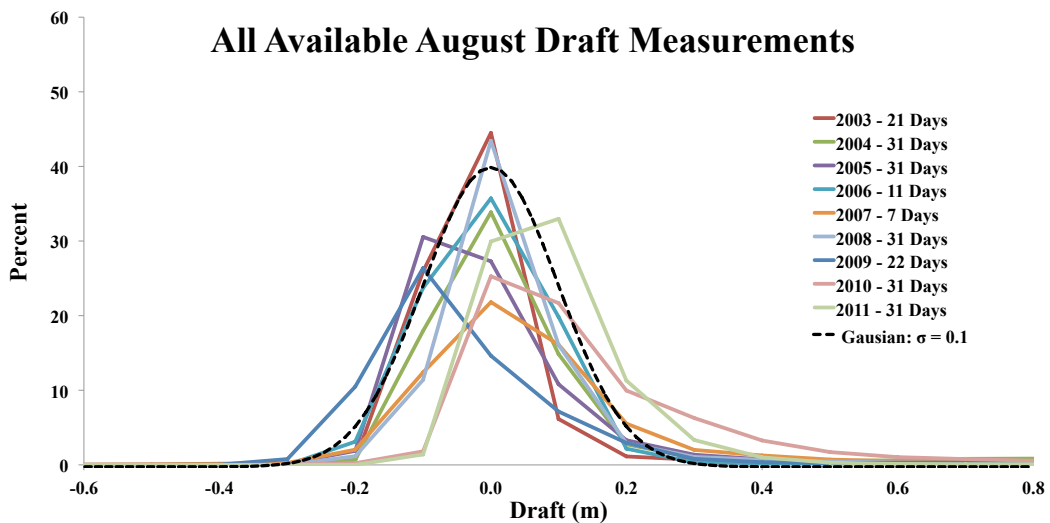


Figure 2.4: Probability distribution of all observations during the month of August. Dotted black line shows a Gaussian distribution with zero mean and standard deviation = 0.1m.

2.2.2 Ocean density and speed of sound

Equation 2.2 requires SS , the true speed of sound, while equation 2.6 requires ρ , the depth-averaged density. We derive these time-varying parameters from CT/D moorings first described by Rabe et al. [2010]. These moorings near the IPS locations

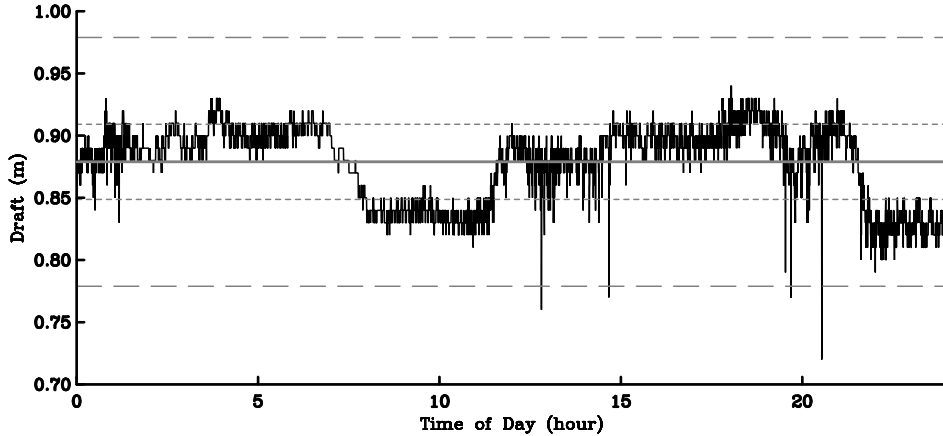


Figure 2.5: Draft observations on 1 April 2004 (15 second interval). Gray lines show mean (solid), \pm one standard deviation of observations (short dashes), and \pm our error estimate (long dashes).

contain SBE37sm CT/D sensors at nominal depths of 30, 80, and 130 m. Figures 2.1 (c through f) identify the locations of the instruments that recorded data at 15 minute intervals. Using the regression analysis described in Rabe et al. [2012], we construct time series of density and speed of sound for the water column above the sonar. Section 2.7 provides further details.

2.2.3 Atmospheric forcing

Equation 2.6 requires P_a , atmospheric pressure, to remove the inverted barometric pressure effect. Since there was no contemporaneous meteorologic data at the mooring site, output from a regional atmospheric model provided a substitute [Samelson and Barbour, 2008] at hourly intervals. Values were interpolated linearly to the sampling interval of IPS range measurements. Section 2.8 provides further details.

2.2.4 Quasi-Lagrangian frame

We measure ice draft and velocity in a spatially fixed or Eulerian frame. However, the ice passing our observing array consists of discrete particles during the mobile season and a fixed surface during the land-fast season. This bimodal character of ice motions leads to biased statistics. We therefore present ice draft probability density

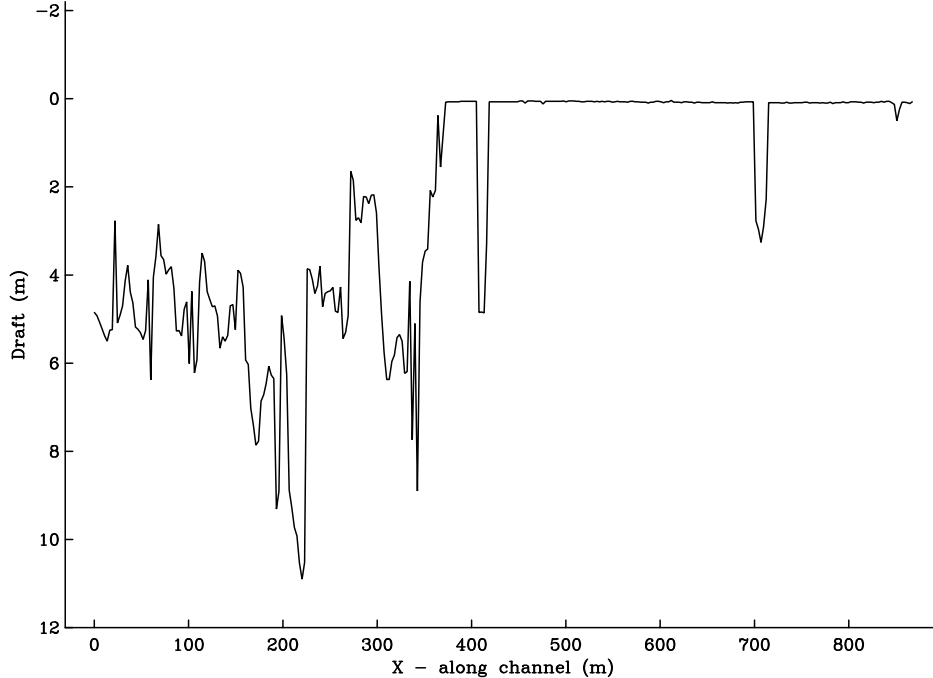


Figure 2.6: Bottom topography of ice measured on 8 August, 2005 from 4:00 to 4:45 GMT. Near zero values indicate open water.

functions by transforming our Eulerian observations of ice draft $D(t)$ into a quasi-Lagrangian frame $D(x(t))$, where $x(t) = U_{ice} * t$. We used ADCPs to estimate ice velocity, U_{ice} . We used the Doppler shift from the vertical bin that contains a near-surface maximum of acoustic backscatter to derive this velocity. The root-mean-square error is less than 5 cm s^{-1} . The largest errors always occur within 5 km of the Ellesmere Island coast [Münchow, 2016]. After introducing the time series in the next section, we provide all statistical ice properties in this quasi-Lagrangian frame. Ice thickness distributions thus are weighted by ice velocity not time.

2.3 Time Series

2.3.1 Ice drafts and velocity

Our instruments measured ice drafts in Nares Strait for nine years between 2003 and 2012. We observe open water in 25% of all observations. This percentage varies

inter-annually from 21% in 2008-09 to 33% in 2007-08. The daily median draft for ice observations are shown in Figure 2.7 (left). Day-to-day variability ranges from zero to almost ten meters with an annual mean that varies from 0.95 m (2003-04) to 1.98 m (2006-07). The largest daily median ice draft in our record is 9.3 m on 16 February 2008.

Figure 2.7 (right) shows the along-channel ice velocity, U_{ice} , from an adjacent ADCP mooring. Dominant flow in Nares Strait is from the Arctic Ocean to Baffin Bay with a mean along-channel velocity during our record of 0.25 m s^{-1} . During mobile ice season this mean rises to 0.35 m s^{-1} .

2.3.2 Seasonality

Our data describe two distinct ice seasons in the channel. The first is characterized by periods of variable ice draft caused by the rapid advection of thick and ridged MYI that originates in the Arctic Ocean. A second season occurs during periods of little variability when the ice is not moving but grows slowly in place. Gray shading in Figure 2.7 indicates those times when ice is land-fast.

Time series of ice velocity allow us to distinguish the mobile from land-fast seasons. We thus define the land-fast season to begin when daily averaged ice speed remains below 0.025 m s^{-1} for ten successive days and to end when it exceeds 0.06 m s^{-1} for a single day. For all other times we define the ice to be mobile. For each ice year our definition results in a single continuous land-fast interval, the onset and duration of which we list in Table 2.2. The longest land-fast season, persisting 190 days, occurred in 2011-12. In contrast, ice is mobile year-round in 2006-07 [Münchow and Melling, 2008, Kwok et al., 2010], 2008-09 and 2009-10.

Generally during the land-fast season, we observe thermodynamic growth in the ice that is held stationary above our moorings; this is evident in a gradually increasing daily median ice draft (Figure 2.7). There are two exceptions; these occurred during 2007-08 and 2011-12. During the first of these, the brief 47 day land-fast season of 2007-08, we observe high variability in the median ice draft. This indicates that there

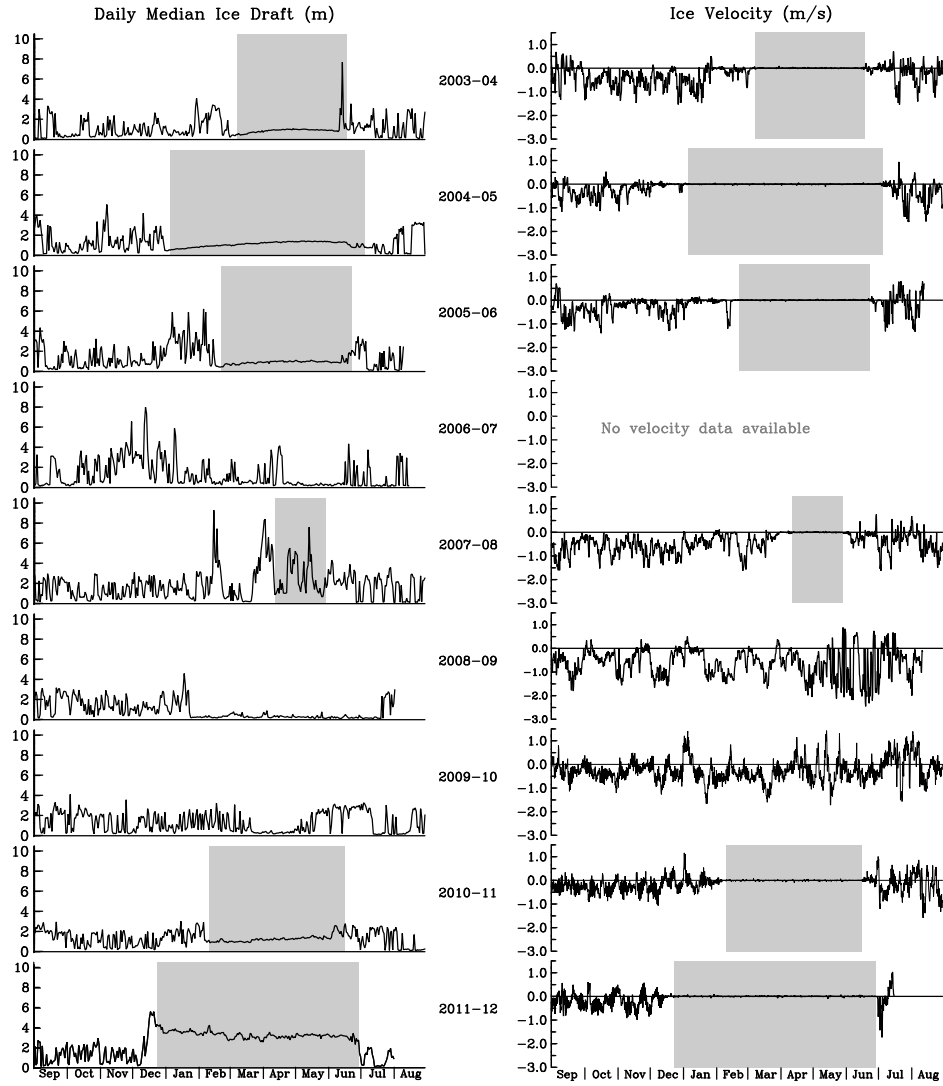


Figure 2.7: Left column shows daily median ice drafts at KS30 (2003-07), KS25 (2007-09) and KF30 (2009-12). Right column shows along-channel ice velocities nearest these stations. Negative velocities are southward. Gray shading indicates fast-ice periods as defined in section 2.3.2.

Table 2.2: Landfast season characteristics

Year	Land-fast Season		North Bridge	South Bridge	Collapse Date
	Onset Date	Duration (days)	Onset Date	Onset Date	
2003-04	8 Mar 2004	102	14 Feb 2004	11 Mar 2004	21 Jul 2004
2004-05	4 Jan 2005	182	7 Dec 2004	31 Dec 2004	6 Aug 2005
2005-06	22 Feb 2006	122	22 Feb 2006	18 Feb 2006	6 Aug 2006
2006-07		0			
2007-08	12 Apr 2008	47		1 Apr 2008	8 Jun 2008
2008-09		0	16 Jan 2009		9 Jul 2009
2009-10		0	17 Mar 2010		15 May 2010
2010-11	10 Feb 2011	127	16 Jan 2011	30 Jan 2011	30 Jun 2011
2011-12	23 Dec 2011	190	3 Dec 2011	10 Dec 2011	11 July 2012

Ice bridge data for the first 6 years are as identified in [Kwok et al. \[2009\]](#), except when we find a northern bridge formed in February 2006 within Nares Strait. The remainder of ice bridge formation dates are estimates to within ± 3 days derived from MODIS imagery.

was ice above our instruments that varied greatly in thickness. This median ice draft variability may be attributable to pitch and roll of the moored IPS allowing us to observe each type of ice for a different percent of a given day. This variability is most likely the result of the lack of a northern bridge; this is the only year in which a southern bridge formed but a northern one did not. Without a northern bridge to halt ice motion north of our instruments, small scale ice motion or dynamic ice processes during this period would cause our instrument to observe different types of ice throughout the land-fast season and our statistical median ice draft to vary accordingly. We intend to address this period in detail in a future paper. The second land-fast ice period where we fail to see evidence of growth in the stationary ice at our mooring location is during the final year of our study. In this instance, we find that the ice above our instruments at the onset of the land-fast season is thicker than in any prior year. We discuss this further in section 2.5, below.

Focusing on the mobile season, we investigate how ice draft changes for the

September/October/November Mean of Daily Ice Draft Percentiles

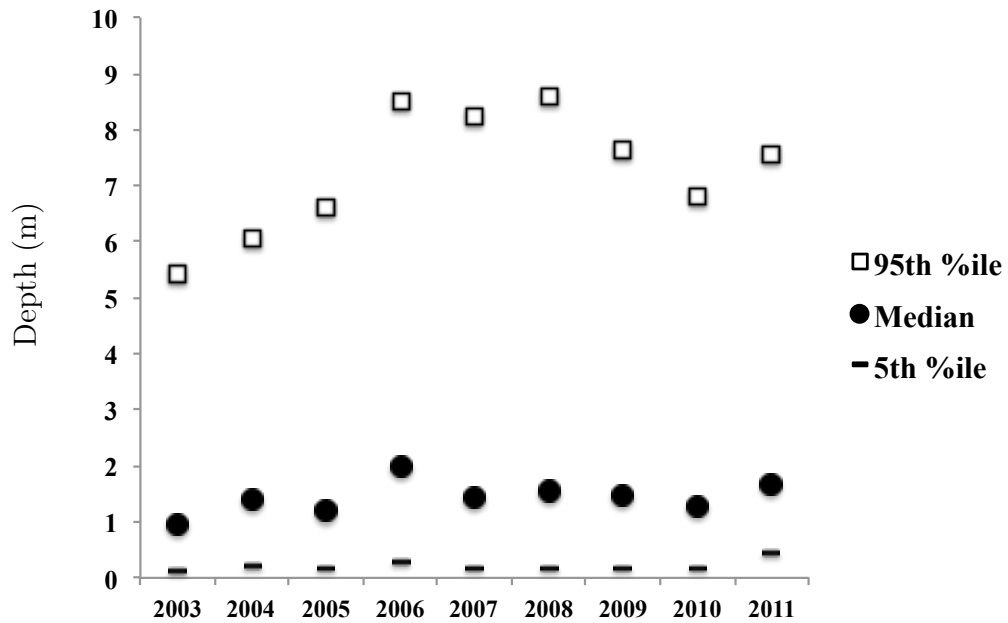


Figure 2.8: Mean of daily ice draft statistics, 5th percentile, median and 95th percentile, during the months of September, October and November for each year.

September, October and November periods when ice velocities are at their maximum and to the south. Figure 2.8 shows the 5th, 50th and 95th percentile ice draft for these three months in each year. For the first eight of our nine deployment years, we found the 5th percentile measurement to vary between 0.13 and 0.27 m but in 2011, this value reached 0.43 m, exceeding twice the average of all preceding years. The range for the median varies between 0.95 and 1.98 meters. The 95th percentile ice ranges from 5.43 m (2003) to 8.57 m (2008), indicating high variability in the thick ice of Arctic origin that is advected through the channel.

2.4 Ice Draft Distributions

2.4.1 Definition and sources

The ice found in Nares Strait varies from nilas that is millimeters thin to glacial ice that can exceed 80 m in thickness [Münchow et al., 2014]. The accuracy of our measurements is 0.1 m (Section 2.7) and is thus insufficient to distinguish nilas from open water; hence we consider any measured draft less than 0.1 m to be water and exclude it from our distributions. We thus define 5 ice categories using the nomenclature of the World Meteorologic Organization for sea ice thickness, “Young Ice” [0.1 m,0.3 m), “Thin First Year Ice” [0.3 m,0.7 m), “Medium First Year Ice” [0.7 m,1.2 m), “Thick First Year Ice” [1.2 m,2.0 m) and “Old Ice” [2.0 m, ∞). Since our measurements are of draft which accounts for roughly 90 percent of sea ice thickness, we have converted thickness h to draft D by

$$D = h * 0.9 \tag{2.8}$$

In terms of origin, young ice is likely to have formed within Nares Strait. We postulate that it entered the channel as seawater, land or glacial runoff, or ice that subsequently melted and refroze locally. In contrast, old ice is formed in the Arctic Ocean where rafting and ridging may occur as the result of forcing by winds and currents [Thorndike et al., 1975]. These dynamic processes result in sea ice exceeding the thickness attainable by purely thermodynamic processes. Old ice enters Nares Strait via the Lincoln Sea in the Arctic Ocean [Kwok, 2005]. We know least about the origin of first year ice which may have formed locally during the land-fast season or been advected from the north into Nares Strait.

2.4.2 Near-decadal time scale

Young ice accounts for one quarter of our ice observations. The first year categories comprise 38 percent in total, with thin ice at 19%, medium ice at 10% and thick at 9% of all ice. Old ice accounts for 37 percent of our observations.

We construct histograms considering only ice greater than 0.1 m in thickness and using the pseudo-Lagrangian method described in Section 2.9. Ice draft counts were grouped in 0.1 m bins. Figure 2.9 shows the cumulative distribution of ice in the channel for the 2003 to 2012 period, excluding that for the 2006-07 ice year for which we did not have velocity data. The mode of the distribution is found in the thinnest ice bin, 0.1-0.2 m. Nearly 25% of all ice measured was of draft 0.2 m or less. The median ice draft is 1.0 m.

Figure 2.10 shows the histogram of the contribution to ice volume which passed our instruments by draft. That is, $D \frac{N_D}{\sum N_i D_i}$, where D is the draft of the ice observation, N_i is the number of observations of ice of draft D_i . Each bin spans 0.1 m. We find a bimodal distribution with primary mode at the 2.0-2.1 m bin, thin old ice, and a secondary mode at the 0.2-0.3 m bin, young ice. The tail of the distribution will be discussed in Section 2.4.5.

2.4.3 Annual time scales

Figure 2.11 shows the annual ice distributions as histograms for each year. The mode is always found in the thinnest category (0.1-0.2 m) and its magnitude each year is close to 15%, except in 2008-09, when it exceeds 20%. With the only ice bridge that year located in Lincoln Sea to the north, MYI does not pass from the Arctic Basin. Therefore, the distribution during 2008-09 is weighted by markedly thinner ice that was mobile throughout the year in Nares Strait. In the first three years, the distribution exhibits decay until increasing near drafts of 1 m. We associate these observations of ice ≈ 1 m with thickening of first year ice (FYI) during the land-fast ice seasons lasting three to six months. This is not observed in the ice distributions of subsequent years. A much smaller increase in probability is observed in ice of approximately 2 m draft.

Figure 2.12 shows the cumulative histogram for each year. The extreme years were 2007-08 when ice was thick and 2008-09 when it was thin. The first of these represents a year without any ice bridges and the second, a year with a long-lasting northern ice bridge (Figure 1.2).

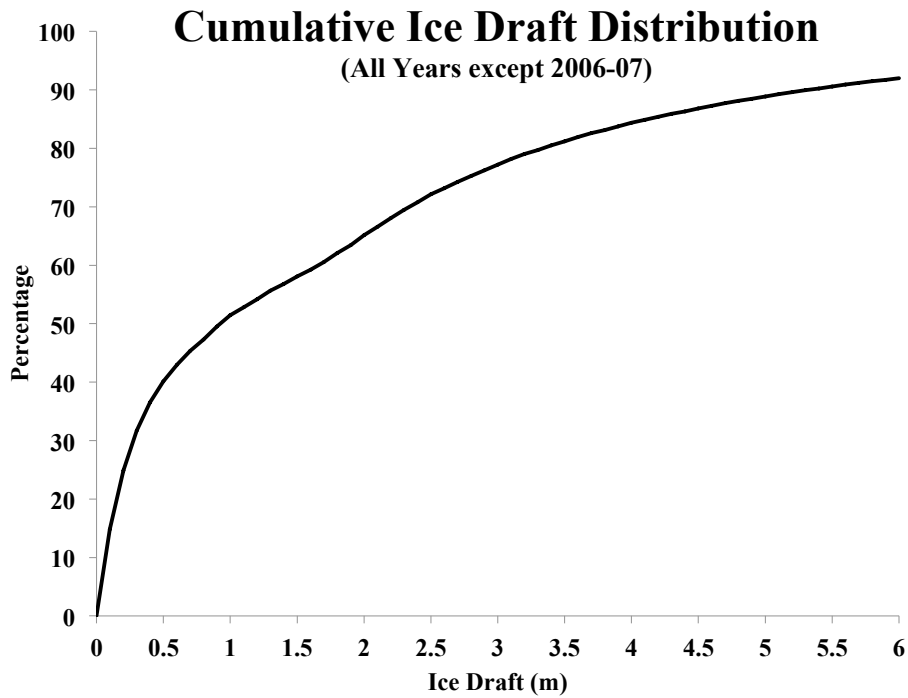


Figure 2.9: Cumulative percentages of ice observations for all years. The distribution is adjusted for ice velocities and, therefore, the 2006-07 ice year is excluded.

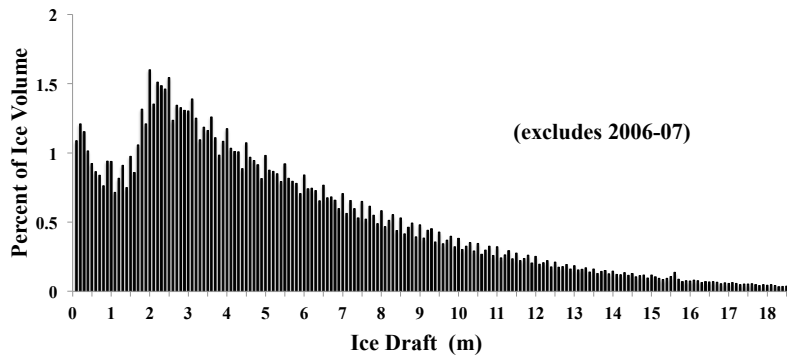


Figure 2.10: Ice volume fraction by draft. Each bin spans 0.1 m and the percent shown is the relative volume of ice. The distribution is adjusted for ice velocities and, therefore, the 2006-07 ice year is excluded.

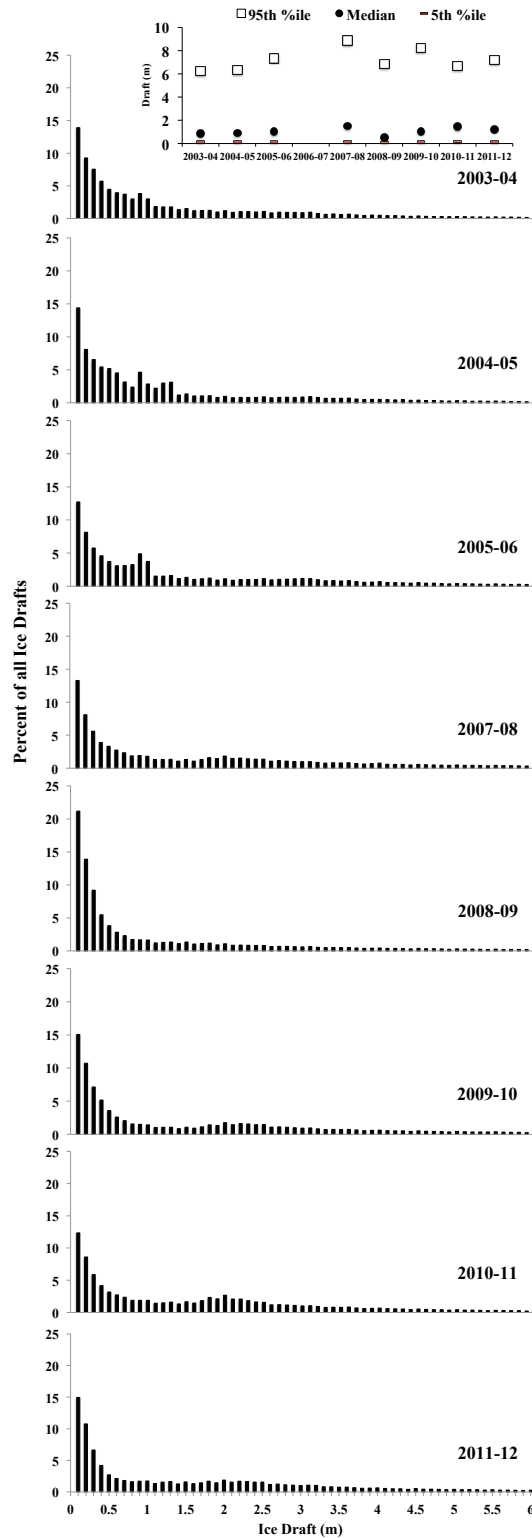


Figure 2.11: Annual probability distribution of ice drafts as a percent of all ice by year (adjusted for velocity). Bins are in 0.1 m increments. Inset at upper right provides statistics of the annual distributions. Note that the 2006-07 ice year is not included as velocity data are unavailable.

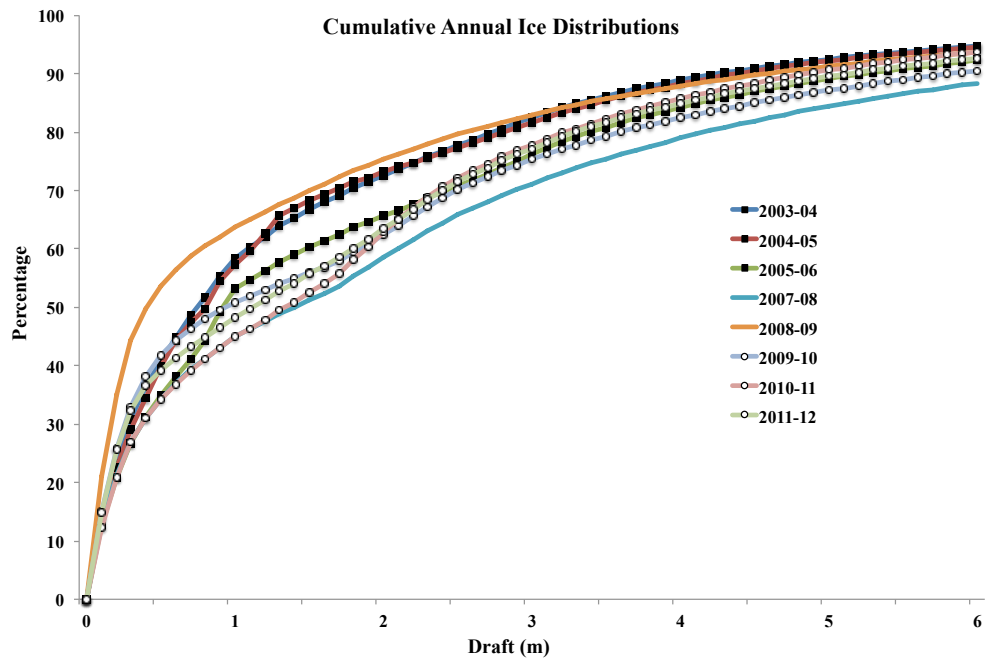


Figure 2.12: Cumulative probability distribution of ice drafts shown in Figure 2.11. Black symbols are associated with early record (2003-2006) and white symbols with later period (2009-2012).

Furthermore, Figure 2.12 suggests that the first three years of our nine year record, identified with black symbols, are dominated by thin ice categories while the last three years, marked by white symbols, contain substantial amounts of ice in both thin and thick ice categories. The two extreme years are the transition towards a thicker ice regime. We speculate that the presence, duration and location of ice arches (Table 2.2) control ice thickness distributions for a given ice year.

Figure 2.13 shows histograms of the contribution to ice volume which passed our instruments by draft for each year. Each bin spans 0.1 m, however for ease of reading we will discuss bins by their mid-point. We find bimodal distributions with primary mode for the first three years in the 0.95 m bin and a secondary mode at 3.15 m. In 2007-08 the primary mode is found in the 2.05 m bin and the secondary is at 0.25 m. 2008-09, dominated by thin ice, has a primary mode in the 0.25 m bin with a secondary at 2.05 m. The remaining years are characterized by a primary mode in the thicker 2.05 or 2.55 m bin and the secondary mode in the 0.25 m bin. These statistical properties of the distributions are shown in the inset of Figure 2.13.

2.4.4 Across-channel variability

The flow of water in Nares Strait varies across the channel. Rabe et al. [2012] identified a jet below 30 m depth of intense along-channel flow in the water column close to the coast of Ellesmere Island. Remote sensing studies suggest that thick ice moves southward along the strait with a preference for the Ellesmere Island coast. This is consistent with a buoyancy-driven geostrophic flow. The across-channel variability of ice flow, however, has not been quantified. During three years of our study, 2003-2006, we measured ice draft and velocities at two locations, KS20 and KS30. These stations are separated by 18 km, with KS20 located 7.5 km from the coast of Ellesmere Island. Figure 2.14 shows the probability density functions of ice drafts in 0.1 m bins of KS20 and KS30 separately; the inset graph provides the 5th, 50th and 95th percentiles for each of these distributions. We find that the ice is generally thicker at KS20. This

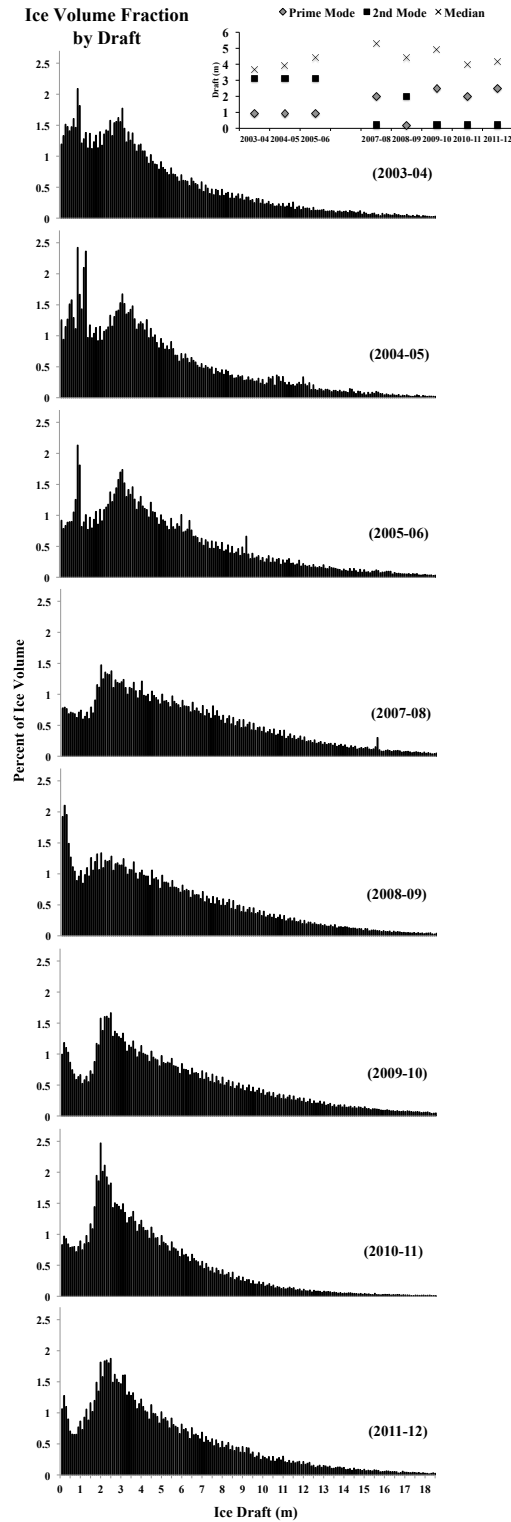


Figure 2.13: Annual ice volume fraction by draft. Each bin spans 0.1 m and the percent shown is the relative volume of ice. The distribution is adjusted for ice velocities. The inset at the top is a chart of the modes and the median of each distribution.

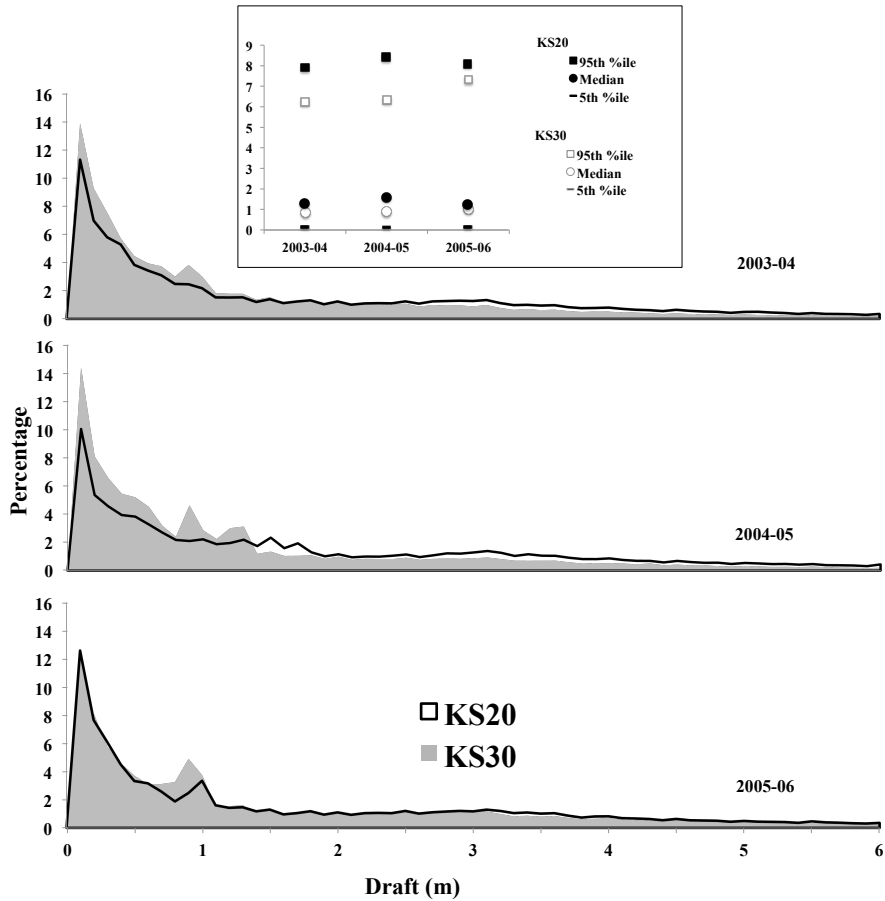


Figure 2.14: Probability distribution of ice at KS20 (black line) compared to ice at KS30 (gray shade). Inset chart shows 5th, 50th and 95th percentile for each of these distributions.

agrees with remote sensing imagery. During 2003-06, we found the average ice velocity to be 0.06 m s^{-1} at KS20 while it was 0.17 m s^{-1} at KS30 (Figure 2.15).

Although we only have ice draft data at one location between 2007 and 2009, we measured surface velocities at five locations across Nares Strait (Figure 2.1 panel e). Münchow [2016], utilized these data to show that along-channel ice velocities vary across the channel. During this period, Münchow [2016] also found that the velocity near Ellesmere Island at the KS20 location was somewhat lower than in the center of the channel at KS30.

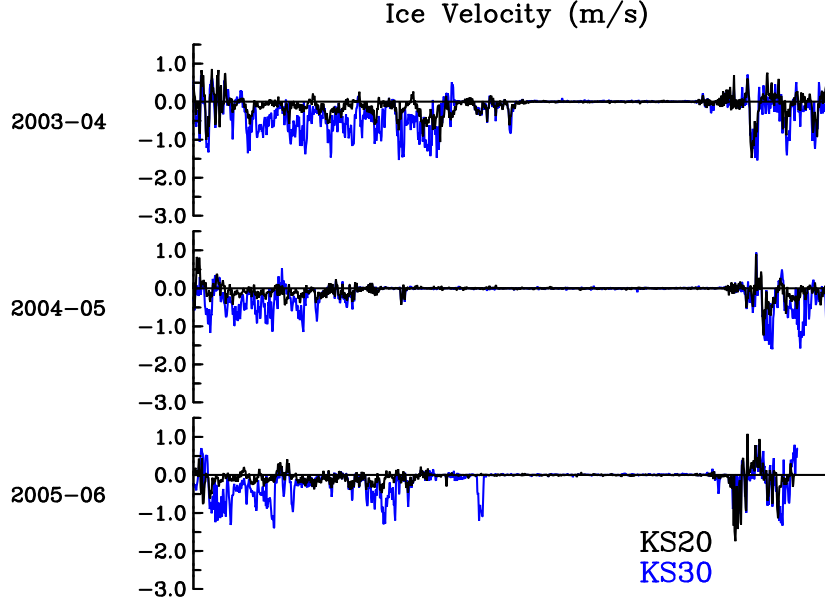


Figure 2.15: Ice velocity at KS20 (black) compared to KS30 (blue).

2.4.5 Thick ice

Wadhams [1981] found the distribution of thick ice in the Arctic Basin to be nearly exponential, i.e.,

$$g(D) = g_0 e^{-D/D_0} \quad (2.9)$$

Following Thorndike [2000], we derive the probability distribution for thick ice, $g(D)$, that has an e -folding decay scale, D_0 , and a probability at zero draft, g_0 . We estimate D_0 and g_0 by minimizing the least square error between the model $g(D)$ and our data (Figure 2.16). Episodically glacial ice is present in Nares Strait. Specifically, we see evidence of an ice island from Petermann Fjord passing our instruments on 22 September 2010, after a large calving event [Münchow et al., 2014]. We found that prior to this calving, less than 0.2% of all ice exceeded 18.5 m in any ice year and chose this value as an upper limit in our study.

We utilize $g(D)$ to evaluate the change of thick ice between 2003 and 2012. The inset of Figure 2.16 shows that the e -folding scale $D_0(t)$ ranges from 2.4 m in 2010-11

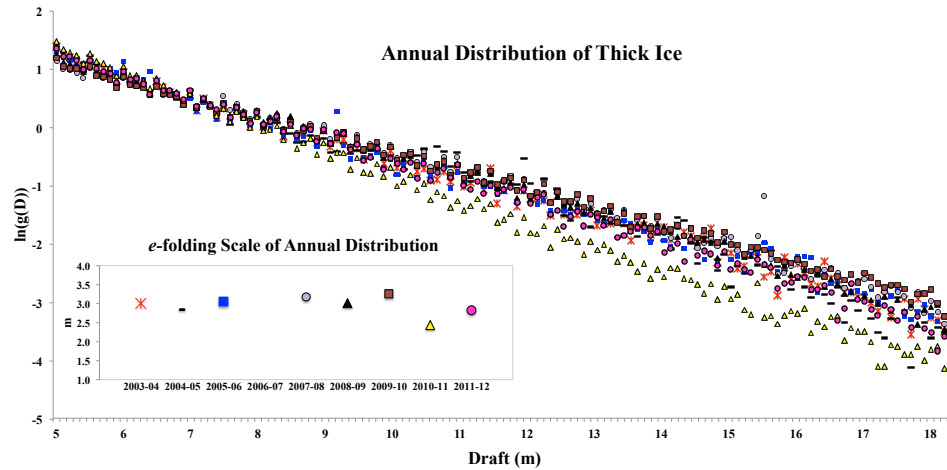


Figure 2.16: Distribution of thick ice on a log-linear graph (large graph). Symbols indicate observation year. Inset graph shows the e -folding scale of the analytic function for each year’s ice distribution.

to 3.3 m in 2009-10 with an average of 3.0 ± 0.2 m. A larger e -folding scale indicates a higher proportion of thicker ice. For comparison, [Thorndike \[2000\]](#) reports values of 1.9 m and 2.6 m for studies conducted in the Arctic Ocean in 1993 and 1996, respectively.

The temporal trend of $D_0(t)$ in Nares Strait is -0.03 ± 0.08 m yr⁻¹ which is statistically indistinguishable from zero. Thus we find variability to ice distributions over the period rather than a thinning or thickening trend in thick ice in Nares Strait from 2003 to 2012. In contrast, thick ice in Fram Strait was observed to become thinner [[Hansen et al., 2013](#)].

2.5 Ice Bridge Control and Implications

Seasonal ice bridges span Nares Strait and have the ability to block ice flow for many months at a time (Figures 1.2 and 2.7). The ice bridges control ice flow and influence ice thickness distributions. When a bridge forms at the southern location, the ice flow is halted throughout the strait. Thermodynamic ice growth is observed in thin and medium ice during these land-fast seasons.

2.5.1 Impacts of land-fast seasons

Ice is always mobile in Nares Strait from August to November when ice of all thicknesses passes over our moored array. In most years at some time between December and February the ice stops moving when a southern ice arch between Canada and Greenland shuts down all advection of ice. Our observations indicate that this event coincides with a prolonged period of slow and uniform increase of the ice draft at a time when air temperatures in Nares Strait are generally below -10°C [Samelson and Barbour, 2008].

The growth of stationary ice is evident in the daily median ice drafts during the land-fast ice seasons (Figure 2.7). In some years, when the ice is less than 2 m thick, we see a gradual increase in thickness of the ice that is immobile above our instruments. Towards the end of the land-fast season, ice thickness begins to fluctuate as the bridge collapses.

In the final year of our study, we do not see growth in the ice observed during the land-fast season. This year, the ice trapped above our instruments at the onset of the land-fast season is ~ 4 m thick. We explain the lack of ice growth in this year with the analytical results of Maykut and Untersteiner [1971]. They observe that ice stops growing when the heat flux into the ice from the ocean equals the heat flux out of it into the air. The heat flux across the ice-ocean and ice-air interfaces depend on factors such as the wind speed, snow cover, thermal conductivity of sea ice, ocean mixed layer turbulence, etc. [Hibler, 1979], but ice in the Arctic Ocean generally stops growing thermodynamically when it reaches a thickness of about 3 m. Consistent with this, we find no ice growth in the stationary ice above our instruments during the 2011-12 land-fast season, because the initial ice is more than 4 m thick. The thick ice insulates a warm ocean from the cold atmosphere above and thus thwarts the transfer of heat from the ocean to the atmosphere necessary to freeze sea water.

The southern ice arch in Nares Strait generally collapses by the last week of July [Canadian Ice Service, 2011] (Table 2.2). As ice starts moving again, median drafts fluctuate at daily time scales, because a variety of ice floes now pass over our sensors.

2.5.2 Free-flow ice years

Our 2003 to 2012 observational period covers three years when no southern ice arch forms and sea ice advects over our array throughout the year (Figure 1.2, Table 2.2). These free-flow years are 2006-07, 2008-09, and 2009-10, when daily median ice drafts initially fluctuate within the typical range between 0 and 10 meters until they stabilize below 2 meters for 1.5 to 6 months without any thick ice present. We explain this shutdown of the transport of old ice with the formation of an ice arch to the north of our mooring array. Remote sensing indicates a northern ice bridge in 2008-09 and 2009-10, but not in 2006-07. In none of these free-flow years did we see evidence of the period of thermodynamic growth that was observed during land-fast ice seasons of other years. With no southern bridge to block ice transport out of the channel, residence time of a floe was too short to detect local sea ice growth.

During free-flow ice years, ice advection through the channel is continuous and newly formed thin ice and medium ice is swiftly advected. We find these years, 2008-09 and 2009-10, to be characterized by lower median ice drafts. As these were the two years with only a northern ice bridge, advection of old ice into Nares Strait through the Lincoln Sea was inhibited for nearly 5 months in the former and two months in the latter, thus restricting the ice observation to young and first year ice. In 2008-09 there is a long period, beginning in late January and lasting through mid July when the daily median draft did not exceed 0.75 m, this coincides with the presence of the northern bridge. During this period we observed the largest southward ice velocities in our record, exceeding 2 m s^{-1} (Figure 2.7). This intensified flow, which rapidly flushes ice through the channel, frees the surface for the formation of new ice. We suggest that the enhanced production and advection of local ice within Nares Strait during this period would be equivalent to an evaporative process in the channel. Since the salt rejection rate decreases with ice age, when residence time in the channel is brief, enhanced salinization of the water of Nares Strait would be expected when only a northern bridge forms.

Model studies by Dumont et al. [2009] found that formation of an ice bridge

in such a channel is dependent on a supply of ice of sufficient thickness. They also found an upper boundary for ice thickness, above which the ice is too resistant to form an arch. Either a shortage of thick ice or an over-abundance of very thick ice may be related to ice flow patterns north of the Lincoln Sea. Kwok [2015] found that the oscillating convergent/divergent conditions in the Arctic Ocean were related to the longstanding patterns of oscillation known as the North Atlantic Oscillation and Arctic Oscillation. He defines convergent periods, as those during which ice flow tends to be towards shore in the central CAA. He derived an index to quantify convergence in the Arctic Basin; our free-flow ice years overlap a prolonged period of intensified convergence between November 2006 through January 2009.

2.6 Discussion and Conclusions

Thick multi-year sea ice exits the Arctic Ocean via Fram and Nares Straits to the east and west of Greenland, respectively. While the sea ice advected southward in the East Greenland Current has been well documented with both in-situ [Hansen et al., 2013] and airborne sensors [Renner et al., 2014], the ice characteristics in Nares Strait are largely unknown. For example, Kwok et al. [2010] estimates ice flux from remote sensing. They assume first year ice to be 1.5 m thick and estimate MYI thickness from two crude snapshots per year. Our observations from 2003 through 2012 at 15 second intervals paint a more complete picture of the type, quantity and probability distribution of the sea ice in Nares Strait that does not always agree with prior assumptions. Our unique data contain substantial variability both from year to year and across Nares Strait but it also describes, two distinct patterns with and without year-round sea ice mobility related to ice arch formation and decay.

We measured ice draft across a 38 km wide section with two instruments for three years. The locations bracket the eastern and western edge of a strong baroclinic circulation where mean ocean speeds and ice velocities exceed 0.3 m s^{-1} and 1.0 m s^{-1} , respectively [Münchow, 2016]. The median ice draft is 1.33 m in the west, while it is 0.88 m in the east. This is consistent with an Ekman-layer response of the surface ocean

and sea ice to local winds from the north. This wind direction indeed dominates the atmospheric circulation [Samelson et al., 2006]. Furthermore, this Ekman-like response would move sea ice from Greenland towards Canada causing a surface divergence with upwelling off Greenland and surface convergence with downwelling off Canada.

We also find substantial inter-annual variability in across-channel ice draft differences that are partially explained by different winds in different years. For example, median ice draft to the east is 52%, 75%, and 23% larger in 2003-04, 2004-05, and 2005-06 while the mean along-channel winds for the same periods are 4.9, 4.3, and 3.9 m s⁻¹ from north to south. The correspondence of local along-channel winds and across-channel ice draft differences is not perfect, however, as other processes impact ice draft. One such process is the duration of ice arches that turn mobile FYI and MYI into a fixed frozen matrix of land-fast ice such as shown in Figure 1.2. These ice arches act as dams to shut down all upstream ice motion while the ocean beneath moves largely unimpeded. Large polynyas result [Dumont et al., 2009] and our 9-year record covers a range of ice arch configurations.

No ice arch formed in 2006-07 and thick multi-year sea ice moved unimpeded through Nares Strait [Kwok et al., 2010]. Median ice draft then was at its maximum during our 9-year observational period reaching 1.98 m while the 95th percentile draft exceeded more than 8 m. We conclude that the absence of any ice arch resulted in the southward export of a record volume of sea ice to exit the Arctic Ocean via Nares Strait. The following year the Arctic Ocean had a historical summer minimum in sea ice cover [Stroeve et al., 2008] that was partially caused by the large export of thick MYI from the Lincoln Sea during the previous winter. Maslanik et al. [2011] offer a range of additional processes all contributing to the thinning of Arctic Sea ice over the last decade that they refer to as "... evidence of a regional tipping point." We here add enhanced MYI export through Nares Strait to this list. We furthermore conclude that the ice flux estimate of Kwok et al. [2010] is likely biased low, because their assumed ice thickness is smaller than our direct in-situ observations.

Apart from a brief six week period, only a northern ice arch formed from 2007

through 2010 and our moorings were located downstream of this Lincoln Sea ice arch. Sea ice during this period was mobile all year, however, it was limited to thin FYI that in 2009 was flushed out of Nares Strait rapidly to result in an anomalous open water season that began in May and lasted until July after the ice arch broke. Thick MYI then streamed southward to our mooring location like a breaking dam. Hence ice navigation was more challenging during the summer in August with air temperatures of 0° C as compared to the winter in May when air temperatures are still at -10° C. Clearly, navigation of Nares Strait is impacted by location and stability of ice arches.

It is tempting to speculate, that this 4-year period of extended open water and thin sea ice in Nares Strait contributed to enhanced wind forcing and mixing to impact the stability of the floating ice shelf of Petermann Gletscher [Shroyer et al., 2017]. This large outlet glacier discharges glacier ice and freshwater into Nares Strait. It partially collapsed in 2010 and 2012 when it shed 1/3 of its floating ice in two large calving events [Münchow et al., 2014]. One of our sensors moored at 75 m below the surface was hit and damaged by a segment of an ice island in 2010.

The “normal” southern ice arch described by Dunbar and Dunbar [1972] formed predictably from 2003 through 2006, briefly in 2008 and again from 2010 to 2012. Furthermore, it has formed each year until 2016 (not shown). Median ice draft distributions in Nares Strait during these years are similar and, we posit, constitute the climatological mean ice conditions with a median ice thickness of about 1 m, however, more than 38% of the ice is old with drafts exceeding 2 m. Histograms of ice volume of all our data show a bimodal distribution with the primary and secondary mode in the 2.0 to 2.1 m and 0.1 to 0.3 m bins for sea ice draft, respectively. The histogram appears to decay exponentially for ice drafts exceeding 3 m. We analyzed the tails of these histograms at annual time scales to investigate the presence of a declining trend that one perhaps would expect with a diminished Arctic sea ice cover, but we find no such trend.

Multi-year sea ice with drafts exceeding 5 m constitute between 9% (2003-04) and 16% (2007-08) of the observed sea ice. The probability $g(D)$ of this thick, ridged,

multi-year ice decays exponentially with draft D at an e-folding scale D_0 of 3.0 ± 0.2 m. While this e-folding scale varies from year to year between 2.5 m in 2010-11 and 3.5 m in 2009-10, the temporal trend of $D_0(t)$ for the 2003 to 2012 data is zero within 95% confidence. We thus conclude that thickest MYI found in Nares Strait has not changed significantly during our observational period. We speculate that our observations document the final stage of the steady draining of the last reservoir of thick, old, MYI that resides in the Lincoln Sea to the north of northern Ellesmere Island and Greenland. Furthermore, the sea ice distribution in Nares Strait over the last decade has become more erratic with periods of thin ice and much open water when a southern ice arch fails to form and periods of year-round southward advection of MYI when no ice arch forms.

The apparent erratic inter-annual sea ice in Nares Strait suggests an ice-ocean system in transition. Hence it would be useful to deploy in-situ ice profiling sonar in Nares Strait to monitor this transition and to provide in-situ observations to ground-truth both air-borne (NASA Operation IceBridge) and space-borne altimeter/radar (ICESat-2, CryoSat-2) systems. Laser and radar altimeters hold much promise to quantify ice thickness and velocity distributions in space and time with which to quantify the sea ice flux from the Arctic to the Atlantic Ocean concurrently to the west and east of Greenland.

The present study allows us to tune and calibrate remote sensing studies that potentially will guide needed detail on how ice draft and velocity varies across Nares Strait and across Fram Strait. We next focus on the flux of sea ice from the Arctic to the Atlantic Ocean. Unlike sea ice draft or thickness, flux implies dynamics and a metric against which to evaluate climate model predictions and their changes over time.

2.7 Appendix A: Error Sources and Ice Draft Sensitivity

Environmental sources of error in the measurement of ice draft include non-ice bodies in the path of the beam, sea surface slope, surface waves, snow load and

variations in density and sound speed (functions of salinity, temperature and pressure in the water column). The incidence of non-ice bodies in the water column is thought to be quite small. Our handling of ice drafts, on the basis of medians and probability distributions over weeks to months, is expected to insure that these occasional errors will be so small in number as to be insignificant. Sea surface slope is a very small number that is well below our precision of measurement. With regard to surface waves, the water in Nares Strait is comparatively quiescent especially when ice is on the surface. On our research cruises we saw swells on the order of 10 to 20 cm. There is evidence of this in the probability distributions around open water modes where one can see open water peaks straddling the 0 m point with small negative values. This error should be symmetric in distribution so that in a statistical sense, positive and negative errors would offset each other. Snow load on the ice is beyond the scope of our measurement capabilities. Average annual precipitation at nearby Pituffik during this period was 0.20 m [Wong et al., 2015]. This provides an upper limit to the contribution of snow load to ice draft estimates.

The largest source of uncertainty in the calculation of ice draft, however, is attributable to the salinity and temperature characteristics of the water column, impacting the calculation of the water level η (predominantly salinity) and the true speed of sound SS (predominantly temperature). The partnered CT/D moorings deployed near those of the IPS are intended to provide contemporaneous measurements of these water qualities to minimize the error introduced by changes in these qualities over time. The mooring design for these instruments provides for measurements to be taken at varying depths in the water column, as the tethered instruments bow down in fast currents and rise towards their nominal depth at minimal current velocities. Since measurement of salinity and temperature are instantaneous at no more than two locations within the water column above the nominal depth of the IPS by the instruments at 30 m and 80 m depths, we take advantage of the vertical sampling of the water column over a day to obtain a higher vertical resolution in salinity and temperature, and use these to extrapolate speed of sound and density averaged over the 100 m and

110 m water column by the regression algorithm outlined in Rabe et al. [2012]. Time series of these data are shown in Figures 2.17 and 2.18.

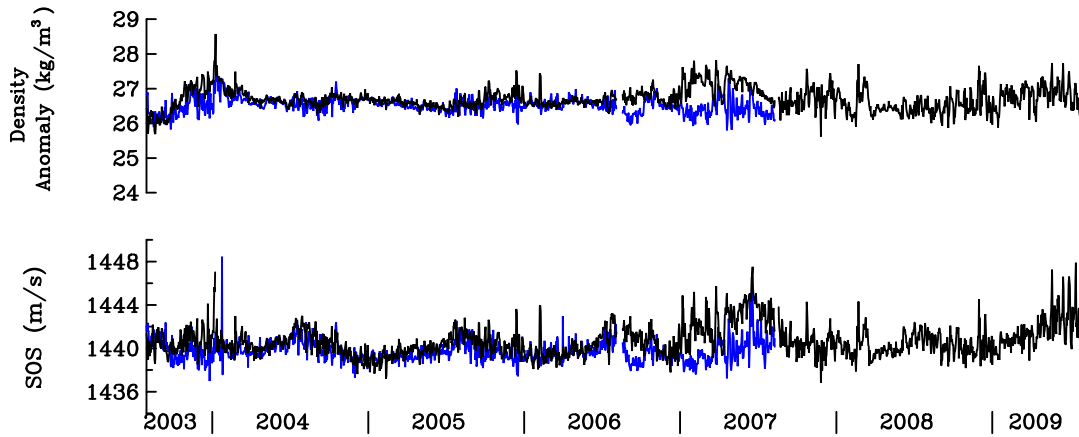


Figure 2.17: Water column characteristics for 2003-09. Depth averaged density and speed of sound for the upper 100 m of the water column from CT/D moorings adjacent to IPS (blue: west, black: east).

To assess the validity of this method, we utilized a series of 10 full water column CTD casts performed adjacent to KS09 on 22 August, 2007 at approximately 1 hour intervals (see Figure 2.19). Taking three randomly selected depths from each of the casts (one attainable by each of the 30 m, 80 m and 120 m moored SBE37s), we took the salinity and temperature measured at those depths and applied the regression method to derive a speed of sound representative of the top 100 meters (1441.54 m s^{-1}) and top 110 meters (1441.79 m s^{-1}). Comparing these to the true values for the water column averaged over all casts, 1440.70 and 1441.00 m s^{-1} it was found that difference in velocity would result in an error of .06 m and .05 m of ice draft respectively.

A daily profile for sound speed and density was then derived using the same regression method applied to the moored CT data for the 2003-2006 deployment. An analysis was performed to quantify the error introduced by the extrapolation of in-situ measurements gathered at circumstantially diverse depths to represent the entire water column. It was found that the variability of daily vertical averages with the 3-year time series are $\sim 1.4 \text{ kg m}^{-3}$ for density and $\sim 6.0 \text{ m s}^{-1}$ for speed of sound. These give us

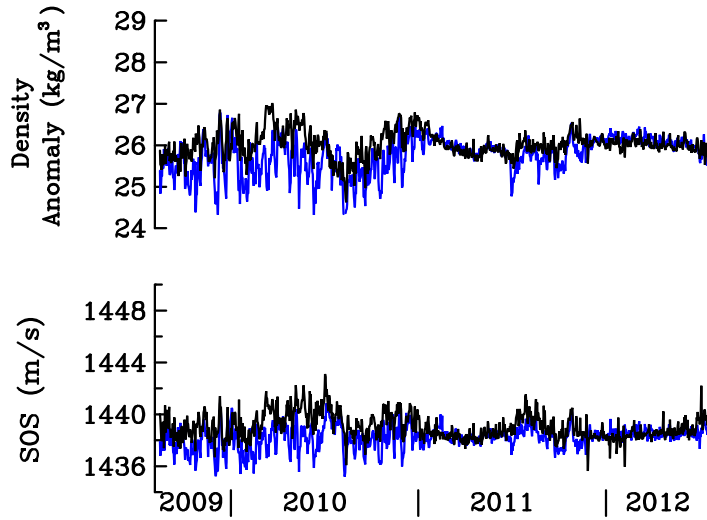


Figure 2.18: Water column characteristics for 2009-12. Depth averaged density and speed of sound for the upper 75 m of the water column derived from CT/D moorings adjacent to IPS (blue: west, black: east).

an uncertainty of $\pm 0.7 \text{ kg m}^{-3}$ and $\pm 3 \text{ m s}^{-1}$ if one assumes a vertical average that does not vary in time. The RMS misfit between data and multiple regression was found to be $\sim 0.1 \text{ kg m}^{-3}$ for density and $\sim 0.4 \text{ m s}^{-1}$ for speed of sound. We determined deviations of the magnitude of the stated uncertainty would result in an error in ice draft estimation of $\sim 0.06 \text{ m}$ for density and $\sim 0.21 \text{ m}$ for speed of sound.

The IPS rises and falls in the water column (with currents) and the water level above it rises and falls (with tides), its apex during the first deployment was at $\sim 97\text{m}$ depth and it often descended to $\sim 106\text{m}$ (on one occasion it reached a depth of $\sim 112\text{m}$). With the typical range of vertical motion found to constrain the depth between 100-110 m, we determined that there would be a variation to the vertical average of $< 0.12 \text{ kg m}^{-3}$ for density and $< 0.50 \text{ m s}^{-1}$ for speed of sound between 100 m depth and 110 m depth. Our calculations take into account these variations in depth to first order.

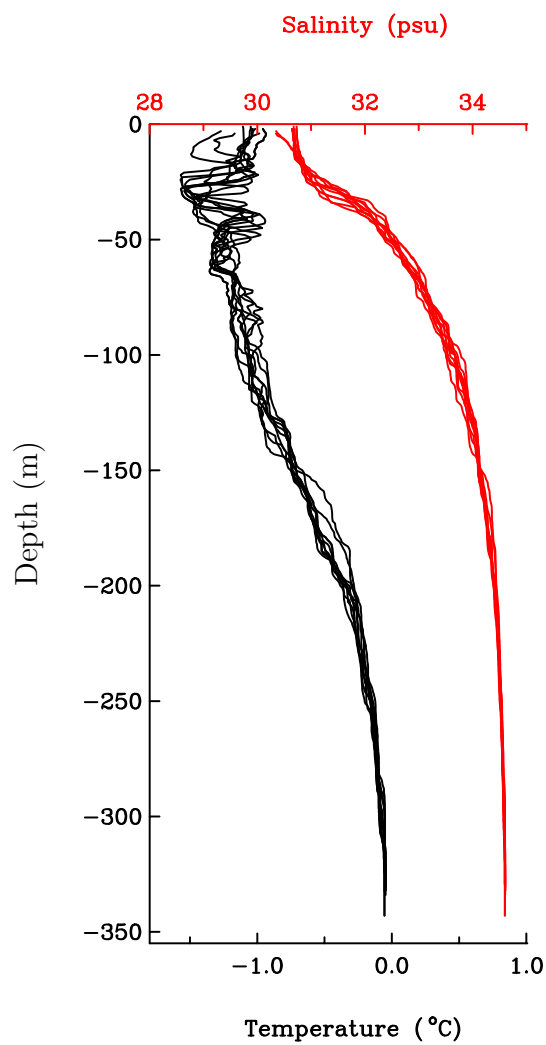


Figure 2.19: Salinity and temperature measurements from 10 hourly CTD casts performed adjacent to KS09 on 22 August 2007.

2.8 Appendix B: Atmospheric Model

When model data were not available due to intermittent gaps in model output, these were generally of sufficiently short duration (≤ 3 days) that a linear interpolation was used to span missing data. The limitation for this method was determined to be ~ 4 days by the decorrelation time scale. An alternative source for atmospheric pressure was sought for two long gaps (42 days in February/March of 2006 that are interrupted by a single day of data) as well as for the final deployment (2009-2012) during which substantial model data was unavailable. Atmospheric data measured at a NOAA meteorologic station at Pituffik, Greenland (available via FTP at <ftp://ftp.ncdc.noaa.gov/pub/data/g sod>) was used. This site provides daily measurements of atmospheric pressure. In order to derive a relationship between measurements at Pituffik and those provided by the atmospheric model, a linear regression analysis was performed using a daily average of the model data (centered at noon) and the daily Pituffik data for a 364 day period during which both data sets were gap-free. The regression model derived was:

$$P_{\text{model}} = 82.230931 * P_{\text{Pituffik}} + 18371.4417. \quad (2.10)$$

When this regression algorithm was tested against all mutually available data that had been excluded from the derivation phase, high agreement was achieved with $R^2=0.88$. Therefore, within the lengthy gap described above, the regression of daily Pituffik data was linearly interpolated to the frequency of the IPS range measurements.

2.9 Appendix C: Spatial Domain Derivation

Our measurements are in the time domain; we project them into the spatial domain using simultaneous velocity data. With spatial bins, each 0.1 m in length, each ice draft measurement is placed into the bin over the IPS location. All bins are assumed to move along the channel with the ice velocity. When multiple ice drafts are placed into a bin, the last one observed is used. For a given year, we then find

the draft of the ice that falls into each of the bins that has traversed the location of our instruments and derive a probability density function of ice drafts from these. Our ice year begins on September 1 and ends on July 31. In statistical comparisons, the month of August is excluded from the data unless explicitly noted to exclude data gaps resulting from the fact that all deployment/recovery cruises occurred in that month.

Chapter 3

A SEMIANALYTIC MODEL OF CHANNEL FLOW

3.1 Introduction

I here implement a semianalytic two-dimensional steady state model of channel flow under wind forcing with ice. I seek to assess the model's ability to replicate observed along-channel velocities of both water and ice in Nares Strait. The model I use is described in [Huntley and Ryan \[2018\]](#). Although the drag coefficient was held constant in that publication, the algorithm permits varying ice roughness through this parameter, thus amplifying the transfer of momentum due to wind stress when ice roughness is increased. I will explore a range of values for the drag coefficient to simulate mobile ice in the model. I will assume that ice flowing down the channel moves at the same velocity as the surface of the water. To assess the model results, I will compare the model's output surface velocity at the central channel to ice velocity observations at that location.

Having time series of ice velocity and draft observations over nine years allows the estimation of ice flux through Nares Strait. Adequately estimating this flux, requires a knowledge of how each of these quantities varies across the channel. During three years, ice was measured at two locations. This gives a sense of the spatial variability in ice thickness. However, while velocity was measured at multiple locations for much of our record, nearly all of our velocity data in 2003 through 2006 are within 14 km of Greenland and there were no velocity data between 2006 and 2007 [[Münchow and Melling, 2008](#), [Münchow, 2016](#)]. From 2007 through 2009, we have a robust velocity data set that spans the channel during a prolonged period of free flowing ice. I will compare the modeled velocities using a range of wind velocity and ice roughness

parameters with these data. If observed surface velocities can be reproduced by the model, I will utilize it in conjunction with modeled winds and ice draft roughness estimates to compensate for temporal and spatial gaps in ice velocity data. Thereby, ice flux estimates can be improved.

Nares Strait is a channel subject to very strong down-channel winds [Samelson and Barbour, 2008], with an along-channel pressure gradient that results in dominant flow from the Arctic Basin [Münchow, 2016]. Münchow [2016] found almost 60% of the variance of along-channel ice motion to be explained by the variance of the local winds. During summer, ice is mobile in Nares Strait. However, most years it is covered by land-fast ice for several months at a time. This ice cover acts as a barrier between the atmosphere and the water, thus removing the frictional effect of the wind at the ocean surface. Formation of ice bridges has been associated with a bimodal geostrophic flow structure in Nares Strait [Rabe et al., 2012]. During mobile ice season, a strong near-surface outflow is observed mid-channel. However, when an ice cover spans the channel, fast ice imposes a frictional drag to surface flow. During these land-fast ice periods, a strong jet forms in geostrophic flow within 10 km of Ellesmere Island, centered near 70 m depth (Figure 3.1).

3.1.1 Observations

I briefly review the observed flow structure in the channel and its response to frictional forcing by both wind and land-fast ice. I focus on the period between 2007 and 2009. During this time, ice flowed freely throughout Nares Strait with the exception one 6 week period of land-fast ice, and 5 ADCP's provide ice velocity data across the channel. Figure 3.2 shows observed along-channel flow velocities. Blue is outflow and red inflow. Velocities are measured in 8 m bins throughout the water column from near the bottom through 40 meters from the surface. Surface flow shown is measured ice velocities. Data between the surface and 40 m is interpolated with a biharmonic spline interpolation technique and a regular grid [McIntosh, 1990].

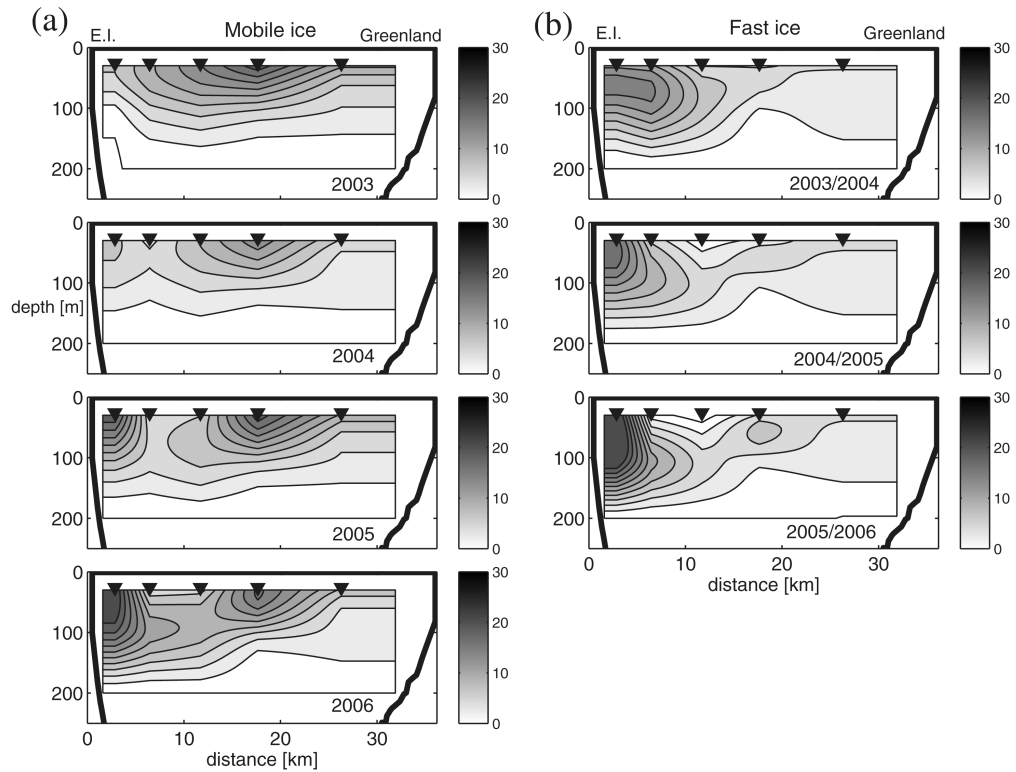


Figure 3.1: Reproduction of the 2 flow regimes in Nares Strait from [Rabe et al. \[2012\]](#). Sections of mean geostrophic velocity at seasonal timescales during each (a) mobile-ice and (b) fast-ice season. Zero geostrophic velocity is denoted in white and positive velocities are to the south [cm s^{-1}]. Each black triangle denotes the horizontal position of a midpoint between two density profiles; the vertical resolution is 1 m. The contour interval is 2 cm s^{-1} .

Figure 3.2 (A) shows an annually averaged along-channel velocity from data gathered in 2008. Strong outflow in the central channel dominates the unidirectional flow. Measured water velocities exceed 0.25 m s^{-1} and ice velocities exceed 0.35 m s^{-1} . As ice flowed freely for most of the year, I compare this to the geostrophic flow identified by Rabe et al. [2012], the flow structure is similar to the 2003 and 2004 seasons when ice is mobile. However, we do not see the intensified jet observed near Ellesmere Island in geostrophic flow for the mobile ice seasons of 2005 and 2006.

Although down-channel winds dominate in Nares Strait, when they reverse as they did in 2008 between August 6 and 8, surface response can be dramatic. Figure 3.2 (B), reveals the effects of strong up-channel winds that averaged 5.4 m s^{-1} over three days. In this instance surface flow reverses for the eastern half of the channel and ice velocities at the station closest to Greenland averaged nearly 0.5 m s^{-1} on August 8. Two days later, the winds reversed again averaging 7.6 m s^{-1} down-channel and the response in the flow of Nares Strait is shown in Figure 3.2 C for August 11. Note that the scale is changed to accommodate the strong ice velocities that approached 1 m s^{-1} spanning the channel. Evidence of the prior up-channel wind may be observed in the return flow throughout the water column at the station closest to Greenland. These markedly different flow structures mere days apart, lend credibility to the atmospheric wind model in a qualitative sense. They also demonstrate how impactful the local winds are to flow of both ice and water in Nares Strait.

Winds in Nares Strait influence the flow of ice and water in the channel until a land-fast ice cover forms as it did on 12 April 2008. Figure 3.3 shows a 30-day average of along-channel flow in Nares Strait during the land-fast ice season of 2008-09. This compares well with the geostrophic flow pattern identified by Rabe et al. [2012] during the fast ice season of all years. However, the intensified flow is centered 30 to 50 meters lower in the water column for the direct velocity observations of 2008 than the calculated geostrophic velocities of earlier years.

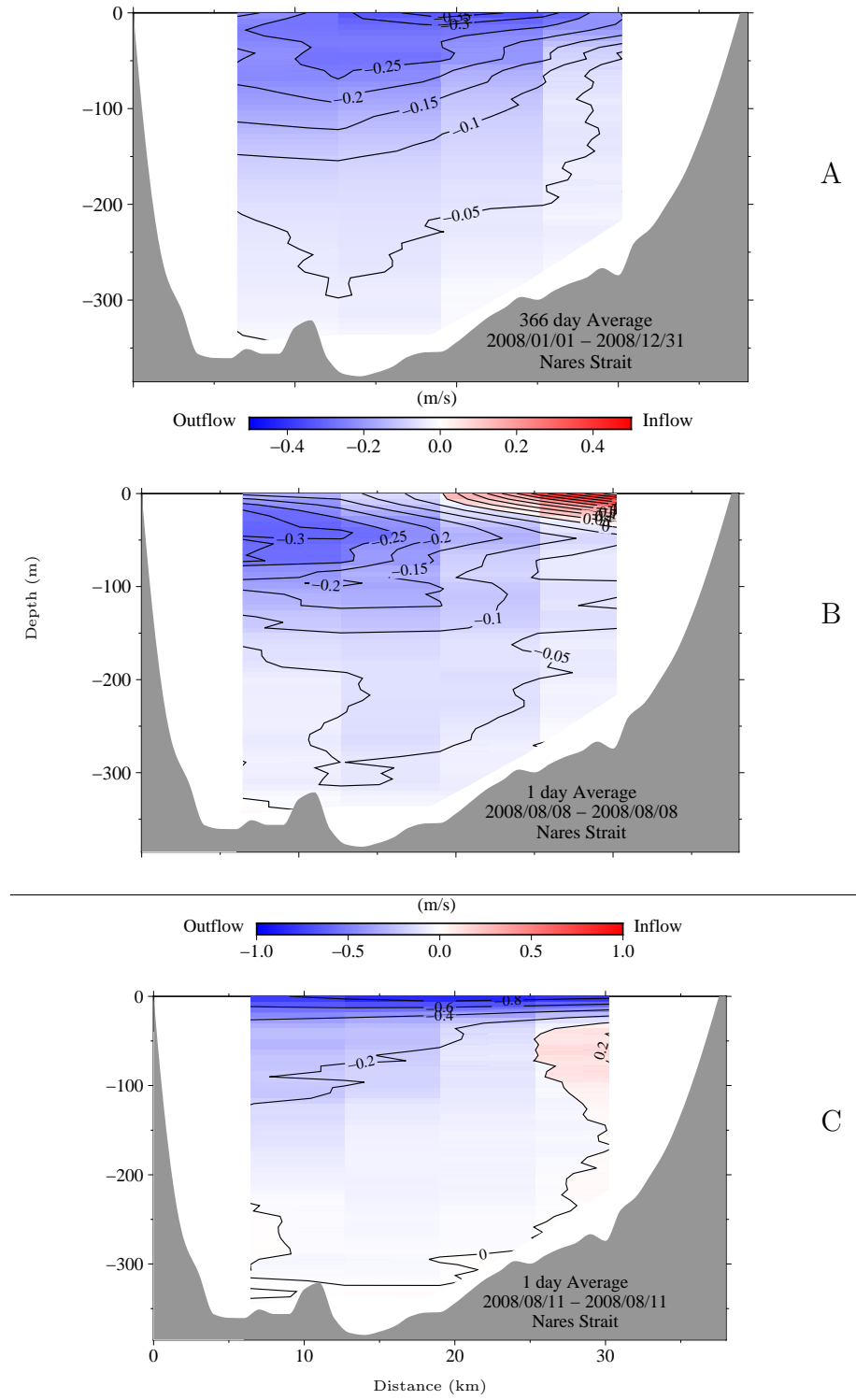


Figure 3.2: Observations of flow in Nares Strait. Average annual along-channel flow velocity for 2008 (A), the third day of a period of strong up-channel winds (B) and the second day of very strong down-channel winds (C).

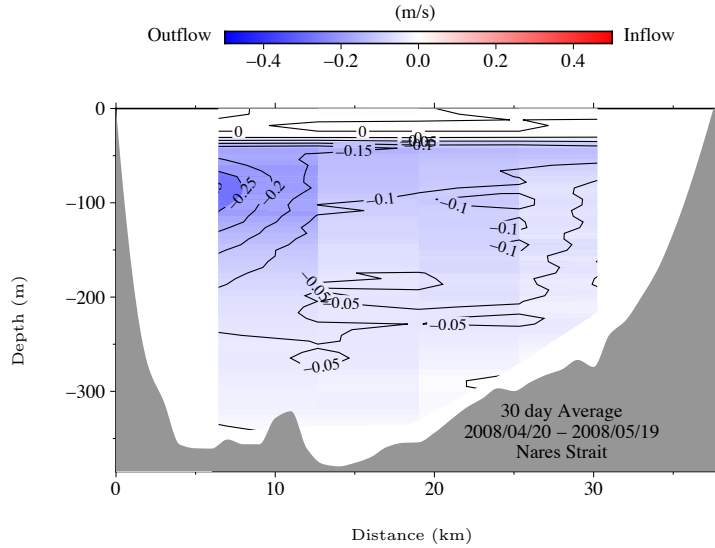


Figure 3.3: Observations of flow in Nares Strait during land-fast ice season of 2008-09.

3.2 Model

I implemented a semianalytic model in Fortran to study flow structure in an idealized strait. [Huntley and Ryan \[2018\]](#) describes the model in detail. It is based on work by [Kasai et al. \[2000\]](#), [Valle-Levinson et al. \[2003\]](#), [Valle-Levinson \[2008\]](#), and [Reyes-Hernandez and Valle-Levinson \[2010\]](#). These outline a solution for flow velocities in a cross-section of a channel with characteristic Ekman and Kelvin numbers. The Ekman number (E_k) is the ratio of frictional to rotational forces. It determines the Ekman depth, which is the extent into the water column that frictional effects at the surface and the bottom will be felt. The Kelvin number (K_E) is the ratio of the channel width to the internal Rossby radius of deformation. This length indicates the horizontal scale at which rotational effects become more important than buoyancy. Using these dimensionless numbers, E_k and K_E , allows one to categorize and compare the flows of otherwise disparate channels.

The model is a solution to the along and across channel momentum equations

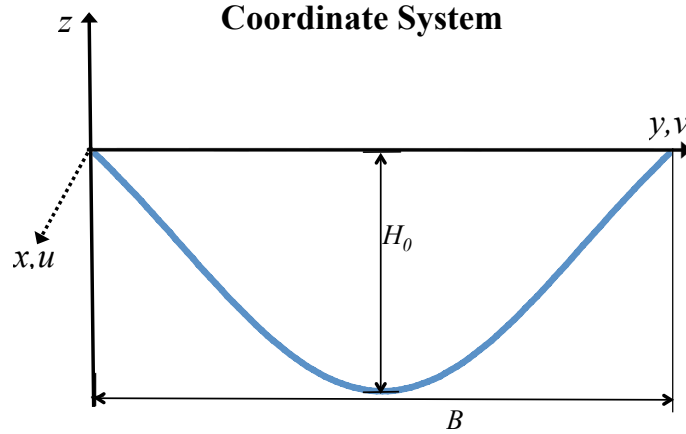


Figure 3.4: Coordinate system for model domain. Dotted line (positive x) is out of the page.

with hydrostatic balance. The governing equations are:

$$-fv = -\frac{1}{\rho_0} \frac{\partial p}{\partial x} + A_z \frac{\partial^2 u}{\partial z^2} \quad (3.1)$$

$$fu = -\frac{1}{\rho_0} \frac{\partial p}{\partial y} + A_z \frac{\partial^2 v}{\partial z^2} \quad (3.2)$$

and

$$\frac{\partial p}{\partial z} = -\rho g. \quad (3.3)$$

Here the variables are the Coriolis parameter (f), along and across-channel velocities (u , v), reference density (ρ_0), pressure (p), eddy viscosity (A_z), density (ρ) and the gravitational constant (g). The coordinate system is as shown in Figure 3.4.

The model requires along-channel volume flux and a prescribed surface slope. To account for non-zero net flux, I used the formulation by [Huntley and Ryan \[2018\]](#), who studied wind effects on flow in an ice-free Arctic channel. Defining a complex horizontal velocity, $\mathcal{U} = u + iv$, a solution in terms of barotropic, F_1 , and baroclinic,

F_2 , components of the form

$$\mathcal{U} = \mathcal{U}_g + \mathcal{U}_\tau = gNF_{1_g} + F_{2_g} + gNF_{1_\tau} + F_{2_\tau} \quad (3.4)$$

is sought where subscripts distinguish geostrophic (g) from wind (τ) induced flow. $N = N(y) = N_x + iN_y = \frac{\partial \eta}{\partial x} + i\frac{\partial \eta}{\partial y}$ is the complex sea surface slope, which varies only in y .

The net volume flux through the section is

$$R = \int_0^B \int_{-H}^0 \mathcal{U} dz dy. \quad (3.5)$$

To solve this, the eddy viscosity A_z is assumed constant and the vertical velocity w is derived from the incompressibility condition. Along-channel gradients in the flow field are assumed to be zero, therefore

$$\frac{\partial w}{\partial z} = -\frac{\partial v}{\partial y} \quad (3.6)$$

which is solved using the boundary condition of $w = 0|_{z=-H}$.

3.2.1 Geostrophic solution

To find the geostrophic velocity, a no-slip bottom boundary condition

$$u + iv|_{z=-H} = 0, \quad (3.7)$$

and a free slip top boundary condition,

$$\rho_0 A_z \frac{\partial(u + iv)}{\partial z} \Big|_{z=0} = 0 \quad (3.8)$$

are imposed.

Using the boundary conditions to solve for F_{1_g} and F_{2_g} yields

$$F_{1_g} = \frac{i}{f} \left[1 - \frac{\cosh(\alpha z)}{\cosh(\alpha H)} \right] \quad (3.9)$$

and

$$F_{2_g} = \frac{-i\mathcal{D}}{\alpha f} \left[(e^{-\alpha H} + \alpha H) \frac{\cosh(\alpha z)}{\cosh(\alpha H)} - e^{\alpha z} + \alpha z \right], \quad (3.10)$$

where $\alpha = \frac{1+i}{d} = \sqrt{\frac{if}{A_z}}$ is the complex inverse of the Ekman Depth ($d = \sqrt{\frac{2A_z}{f}}$). This gives the flux in terms of complex surface slope N and depth H (both y dependent), and the complex scaled density gradient \mathcal{D}

$$R = \int_0^B \left(\frac{igN}{\alpha f} [\alpha H - \tanh(\alpha H)] + \frac{i\mathcal{D}}{\alpha^2 f} [1 - e^{-\alpha H} + \frac{1}{2}(\alpha H)^2 - (e^{-\alpha H} + \alpha H) \tanh(\alpha H)] \right) dy. \quad (3.11)$$

If net flux is prescribed, then the density gradient is

$$\mathcal{D} = \frac{Rf\alpha^2 i - \alpha g \int_0^B N [\tanh(\alpha H) - \alpha H] dy}{\int_0^B [(e^{-\alpha H} + \alpha H) \tanh(\alpha H) - (1 - e^{-\alpha H} + \frac{1}{2}(\alpha H)^2)] dy} \quad (3.12)$$

and the geostrophic velocity, \mathcal{U}_g , at each location of the cross-section as a function of y and z is

$$\mathcal{U}_g(y, z) = gN(y)F_{1_g}(z) + F_{2_g}(y, z). \quad (3.13)$$

3.2.2 Wind stress solution

I now introduce the impact of wind forcing as outlined in [Huntley and Ryan \[2018\]](#). Similar to geostrophic velocity, a solution for velocity due to wind stress is sought, \mathcal{U}_τ , in terms of barotropic, F_{1_τ} , and baroclinic, F_{2_τ} , components of the form

$$\mathcal{U}_\tau(y, z) = gN(y)F_{1_\tau}(y, z) + F_{2_\tau}(y, z). \quad (3.14)$$

Utilizing a bottom no-slip condition as previously stated and top surface condition appropriate to wind stress,

$$\rho_0 A_z \frac{\partial(u + iv)}{\partial z} \Big|_{z=0} = \tau, \quad (3.15)$$

the barotropic and baroclinic terms due to wind stress were found to be

$$F_{1\tau} = \frac{\tau_1}{\alpha \rho_0 g A_z N} [\tanh(\alpha H) \cosh(\alpha z) + \sinh(\alpha z)] \quad (3.16)$$

and

$$F_{2\tau} = \frac{\tau_2}{\alpha \rho_0 A_z} \left[e^{(\alpha z)} - e^{(\alpha H)} \frac{\cosh(\alpha z)}{\cosh(\alpha H)} \right] \quad (3.17)$$

τ , wind stress at the surface, is derived from wind speed \mathcal{U}_{air} thus

$$\tau = C_D \rho_{\text{air}} |\mathcal{U}_{\text{air}}| \mathcal{U}_{\text{air}} \quad (3.18)$$

where ρ_{air} is the density of air, here set to 1.225 kg m^{-3} and C_D is the drag coefficient. I will explore a range of values for the drag coefficient to identify the effects of wind on an ice-free channel and with mobile ice in the model.

3.3 Adding an Ice Cover to the Model

Finally I modify the model to introduce the presence of a land-fast ice cover; this is equivalent to a no-slip upper boundary. Solving for a velocity of the form:

$$\mathcal{U} = c_1 \cosh(\alpha z) + c_2 \sinh(\alpha z) + \frac{igN}{f} - \frac{i\mathcal{D}}{f}z \quad (3.19)$$

with boundary condition: $\mathcal{U} = 0|_{z=0}$, we find:

$$c_1 = -\frac{igN}{f} \quad (3.20)$$

and boundary condition $\mathcal{U} = 0|_{z=-H}$ gives us c_2 :

$$c_2 = \frac{igN}{f} \left[\frac{1}{\tanh(\alpha H)} + \frac{1}{\sinh(\alpha H)} \left(\frac{\mathcal{D}}{Ng} H - 1 \right) \right] \quad (3.21)$$

Solving for \mathcal{D} :

$$R = \frac{ig}{\alpha f} I_6 + \frac{i\mathcal{D}}{2\alpha f} I_7 \quad (3.22)$$

where

$$I_6 = \int_0^B N \left(\frac{2 - 2 \cosh(\alpha H)}{\sinh(\alpha H)} + \alpha H \right) dy \quad (3.23)$$

and

$$I_7 = \int_0^B H \left(\frac{2 - 2 \cosh(\alpha H)}{\sinh(\alpha H)} + \alpha H \right) dy \quad (3.24)$$

so that

$$\mathcal{D} = \frac{-2i\alpha f R - 2g I_6}{I_7}. \quad (3.25)$$

3.4 Applying the Model to Nares Strait

3.4.1 Parameterization

I seek to show flow patterns as simulated in the model for a cross section of Nares Strait where moorings were deployed for the CATS program between 2003 and 2009. Assumptions include an internal radius of deformation $R_i = 10$ km, which yields a Kelvin number of 3.8. This manifests in the model by controlling spatial extent of the across-channel surface slope. The model relies on a constant eddy viscosity A_z that is expressed through the Ekman number chosen. [Huntley and Ryan \[2018\]](#) vary the Ekman number to explore a range of relative channel depths. I also vary the Ekman number to demonstrate implications of viscosity and the sensitivity of the model to the assumed constant viscosity.

The across-channel slope is defined in the fashion of [Valle-Levinson \[2008\]](#) in terms of the internal radius of deformation R_i and a prescribed $N_{y0} = -10^{-6}$ which is the slope at $y = 0$, thus

$$N_y = N_{y0} e^{-(y/R_i)^2}. \quad (3.26)$$

The along-channel slope is set to

$$N_x = -10^{-6} \quad (3.27)$$

The model requires a number of additional parameters to be prescribed. These are shown in Table 3.1 for each run in this study of Nares Strait.

3.4.2 Run 1

I first run the model without wind stress to show geostrophic flow. Net flux is assumed to be 1.0 Sv. This is the midpoint of the observed range of multi-year mean fluxes in Nares Strait [Münchow, 2016]. Ekman number is varied to demonstrate the impact of viscosity assumption on geostrophic flow.

3.4.2.1 Low viscosity

I set the Ekman number $E_k=0.0005$. This corresponds to an Ekman depth $\left(d = \sqrt{\frac{2A_z}{f}} = \sqrt{2E_k H_0^2}\right)$ of 12 m, following Rabe et al. [2012] and Münchow [2016]. H_0 here is defined as the depth of the channel which is 385 m. Figure 3.5 (A), shows modeled velocities for a cross section of Nares Strait with these assumptions. Asymmetry in along-channel velocities is demonstrated with western intensification and near zero surface flow for the eastern two thirds of the channel. Highest along-channel velocity 0.23 m s^{-1} is found in an outflow jet located near 300 m depth within 10 km of Ellesmere Island. The western intensification results from the surface slope which decays exponentially and is scaled to the internal Rossby Radius of deformation. The along-channel intensified surface flow found by Rabe et al. [2012] in geostrophic flow is not observed in this flow pattern. Comparing this to observations (Figure 3.2 (A)), where the strongest observed flow is found in the central channel near the surface, the flow structures are not similar. However, those observations were influenced by winds.

	Identifier	Value				
Constant						
Across slope at $y = 0$	N_{y0}	-10^{-6}				
Air Density(kg m $^{-3}$)	ρ_{air}	1.225				
Along slope	N_x	-10^{-6}				
Coriolis (s $^{-1}$)	f	1.44×10^{-4}				
Depth (m)	H_0	385				
Gravitational const.(m s $^{-2}$)	g	9.8				
Int. Rossby rad. of def. (km)	R_i	10				
Kelvin number	K_E	3.8				
Reference density (kg m $^{-3}$)	ρ	1025				
Volume flux (Sv)	R	1.0				
Width of the channel (km)	B	38				
Variable						
		Panel	Run 1	Run 2	Run 3	Run 4
Eddy viscosity (m s $^{-2}$)	A_z	A	0.0111	10.7	10.7	10.7
		B	10.7	10.7	10.7	0.35
Ekman depth (m)	D_E	A	12	385	385	385
		B	385	385	385	70
Ekman number	E_k	A	0.0005	0.5	0.5	0.5
		B	0.5	0.5	0.5	0.0165
Wind stress (Pa)	τ	A	0	3.85	12.0	0
		B	0	6.1	18.9	0
Wind velocity* (m s $^{-1}$)	\mathcal{U}_{air}	A	0	4.3 D	4.3 D	0
		B	0	5.4 U	5.4 U	0
Drag Coefficient	C_D	A	0	0.17	0.53	0
		B	0	0.17	0.53	0
Non-Dimensional		Relationship				
Ekman Number	E_k	$\frac{A_z}{fH_0^2} = \frac{d^2}{2H_0^2}$				
Kelvin Number	K_E	$\frac{B}{R_i}$				

* U indicates up-channel and D indicates down-channel wind direction.

Table 3.1: Parameter values for model runs.

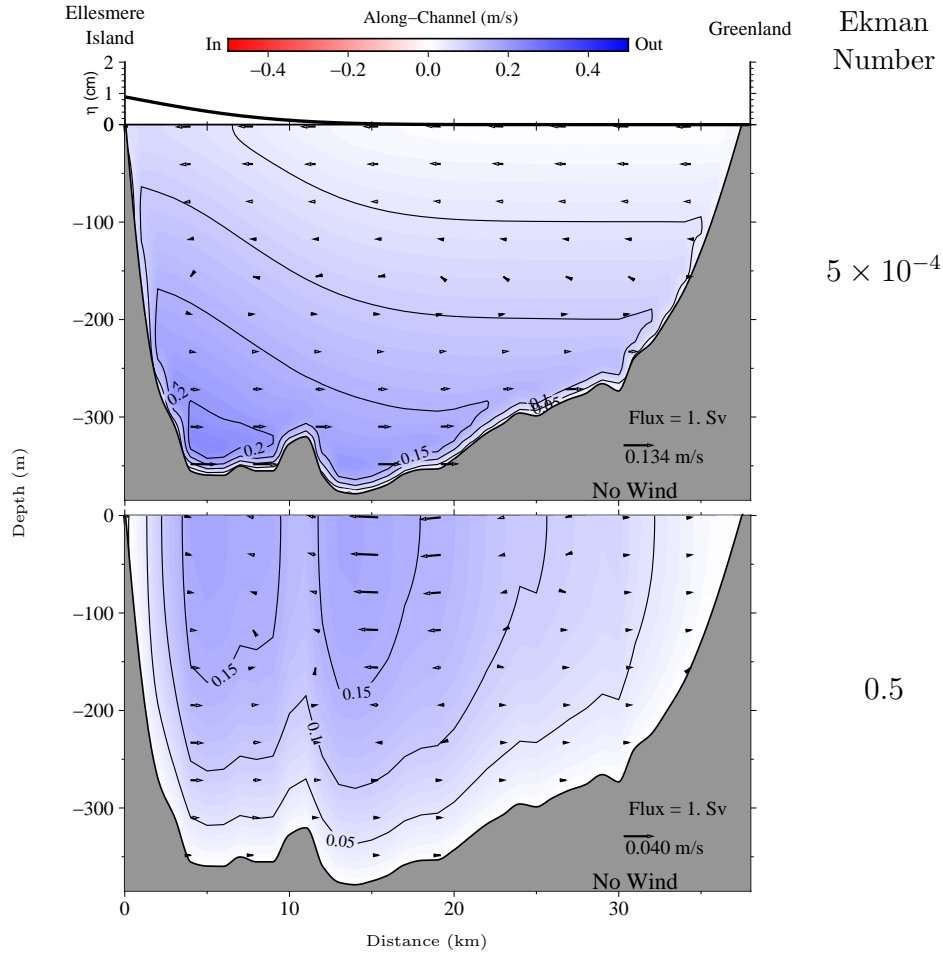


Figure 3.5: Run 1 - Modeled geostrophic velocities. Ekman depth is 12 m (top) and 350 m (bottom).

3.4.2.2 High viscosity

I now adopt the assumption for viscosity in a fashion similar to [Huntley and Ryan \[2018\]](#), thus decreasing E_k to 0.5. This corresponds to an Ekman depth of 385 m. All other assumptions remain the same as above. [Figure 3.5 \(B\)](#), shows the modeled velocities. This increased viscosity results in a flow pattern that is much closer to calculated geostrophic velocities than the prior run. More specifically, surface flow intensity is not restricted to the western channel but spans the central channel and is therefore compatible with observations.

3.4.3 Run 2

I next run the model assuming wind forcing. I utilize an atmospheric model [Samelson and Barbour, 2008] to provide wind velocity data (see section 2.8). Figure 3.6, a scatter plot of wind velocities, reveals the degree to which along-channel winds dominate in Nares Strait. I therefore limit my study to these winds. Median along-channel wind velocity is 5.02 m s^{-1} from the north, it ranges from 18 m s^{-1} from the south to 28 m s^{-1} from the north. Strongest down-channel winds occur in the months of December through February when they exceed 10 m s^{-1} on average. Given the canyon-like structure of Nares Strait where the land rises to nearly 1000 m on the Ellesmere Island coast and perhaps half that on the Greenland coast, assumption of uniform wind stress across the channel is unrealistic. In order to address the frictional effects of these grand walls, I scale the wind stress near the coast. Figure 3.7 demonstrates a sample wind stress profile.

Wind velocities chosen, 4.3 m s^{-1} from the north and 5.4 m s^{-1} from the south, are the mean of modeled along-channel winds during the periods of observation shown in panels A and B of Figure 3.2. The presence of ice is implemented in the model through the drag coefficient. Starting with $C_D = 0.0017$ for open water through $C_D = 0.0053$ for rough ice following Anderson [1987], there was little effect on modeled channel flow at these wind velocities. To achieve results that approach observations of wind induced surface velocities, the parameter needs to be two orders of magnitude higher. This is a consequence of the high viscosity chosen. Figure 3.8 shows the results for winds from the north (A) and from the south (B) when $C_D = 0.17$. Comparing these to Figure 3.2, panels A and B respectively, the flow structures resemble observations. Modeled central channel surface velocities are 0.18 m s^{-1} and 0.09 m s^{-1} while observed velocities are 0.38 m s^{-1} and 0.01 m s^{-1} for panels A and B respectively.

3.4.4 Run 3

To demonstrate the range of surface velocities the model achieves with the amplified drag coefficient, it is increased to 0.53. This is 100 times the value that

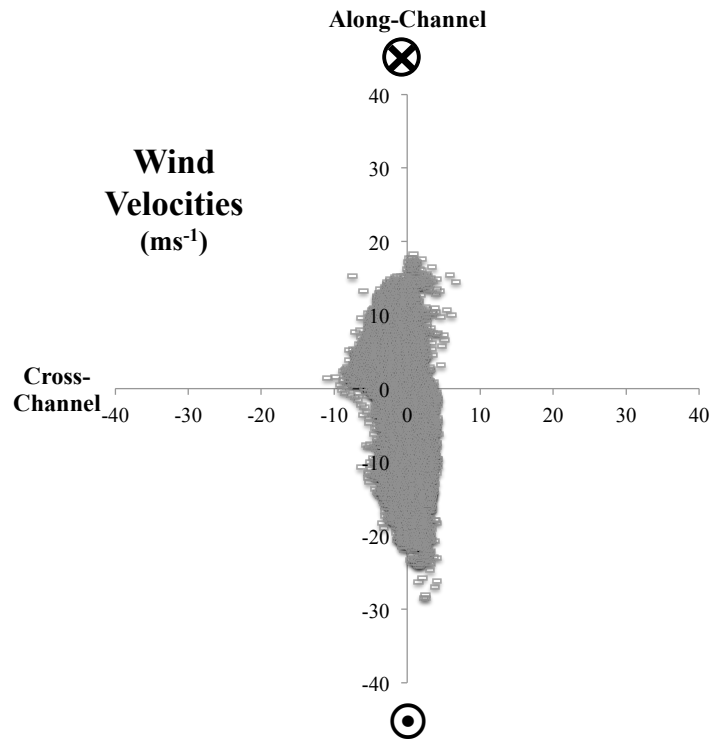


Figure 3.6: Scatter plot for wind velocity.

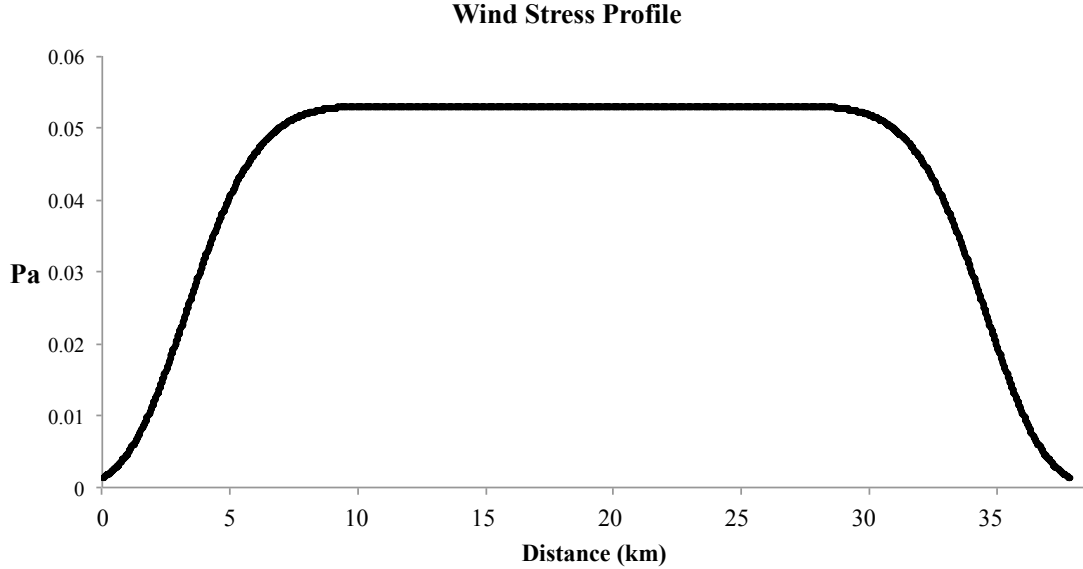


Figure 3.7: Profile of wind stress applied to the model to account for the canyon-like geometry of Nares Strait.

would be appropriate for rough ice. Figure 3.9 shows the resulting modeled flow. The velocity at the central channel for winds to the south (A) is 0.25 m s^{-1} , still somewhat lower than the observed 0.38 m s^{-1} . Whereas that for winds to the north is -0.01 m s^{-1} compared to 0.01 m s^{-1} . It should be noted that in August, when the up-channel wind occurred there would not have been rough ice. But rather that tuning drag coefficient used in the model might improve its ability to simulate flows under wind stress. However, the 100-fold amplification of the parameter is not a comfortable accommodation to achieve these results.

3.4.5 Run 4

Finally, I run the model assuming land-fast ice. As the ice cover is assumed to span the channel, wind velocity is not considered. I run it for both the high viscosity that is used in Run 2, $E_k = 0.5$, and a lower viscosity $E_k=0.0165$. I again consider how a change to the viscosity changes the modeled flow structure.

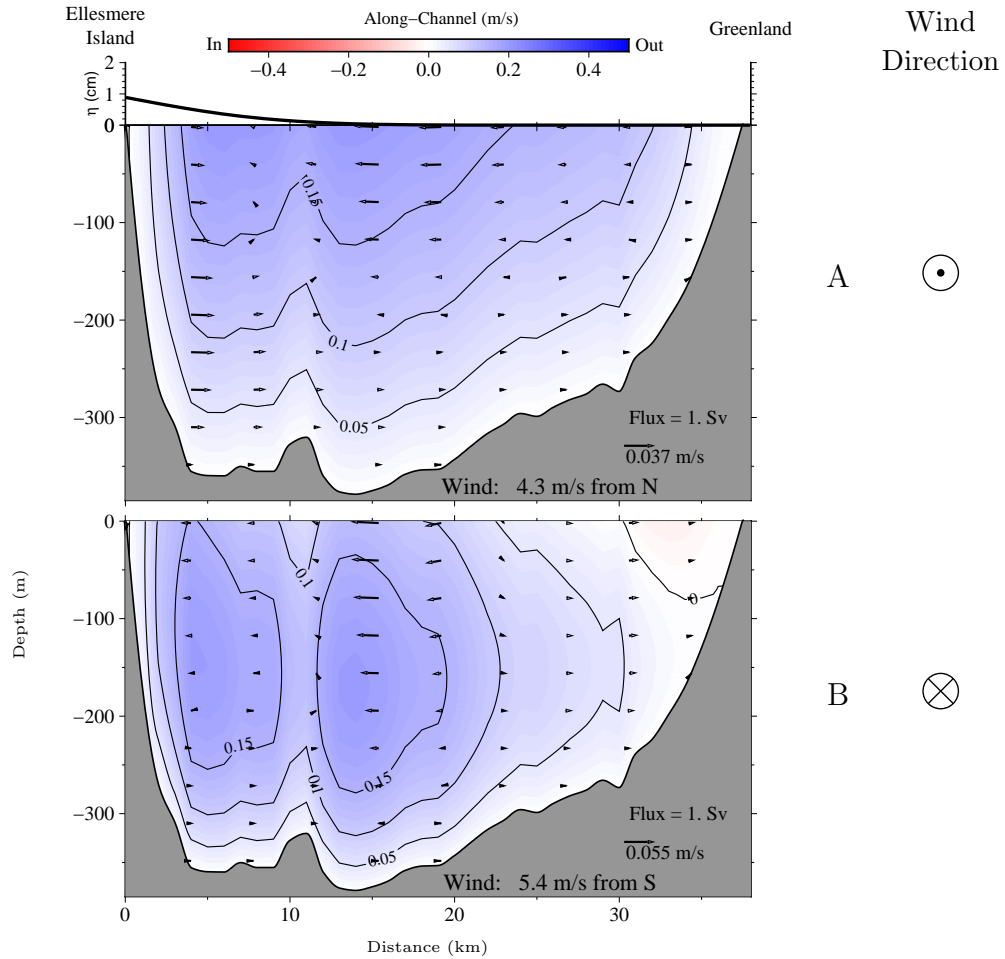


Figure 3.8: Run 2 - Modeled velocities with wind effects and amplified drag coefficient for open water. Windspeed is 4.3 m s^{-1} from the North (A) and 5.4 m s^{-1} from the south (B). These are the average along-channel wind velocities during the observation periods for the respective panels of Figure 3.2.

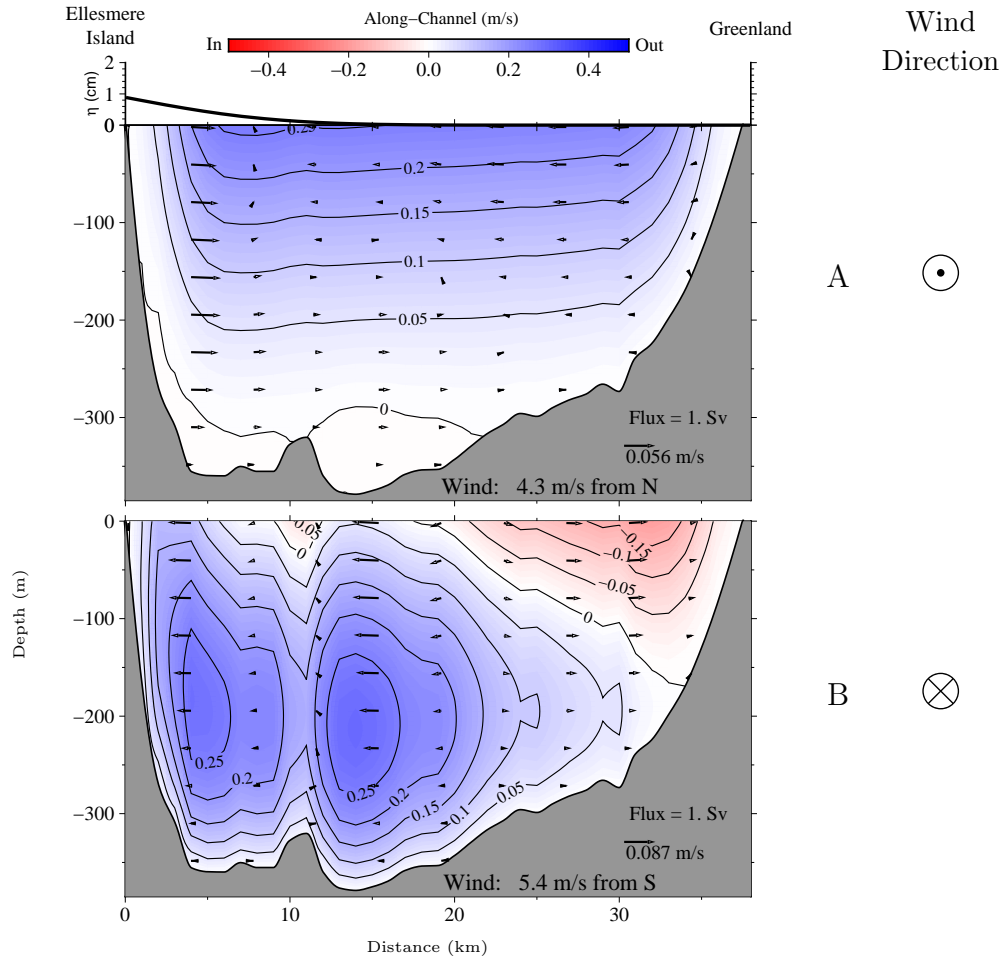


Figure 3.9: Run 3 - Modeled velocities with wind effects amplified drag coefficient for rough ice. Windspeed is 4.3 m s^{-1} from the North (A) and 5.4 m s^{-1} from the south (B). These are the average along-channel wind velocities for the respective panels of Figure 3.2.

3.4.5.1 High viscosity

With Ekman depth of 350 m as it is set in Run 2, Figure 3.10 A shows the modeled flow with the highest velocities in a jet near the central channel. Whereas, observations (Figure 3.3) where water velocity is measured below 40 meters depth, indicate lowest measured water velocities in that location.

3.4.5.2 Low viscosity

By moderately reducing the viscosity to reflect an Ekman depth of 70 m, the model does a somewhat better job of simulating the flow in the channel. This is shown in Figure 3.10 B. Although the jet is at least 100 m lower in the water column and weaker than observed, it is positioned closer to the jet at the westernmost mooring. It should be noted, however, that strong flow spans the channel between 150 and 300 m depth and this is contrary to observations.

3.5 Conclusions

A semianalytic model, that allows for varying both wind stress and ice roughness to simulate surface velocities and thereby supplement ice velocity observations was implemented. Parameterization with realistic values for Kelvin and Ekman numbers in the model results in a flow structure that is inconsistent with observations for the channel. Intensified outflow near Ellesmere Island is associated with the imposition of an across-channel slope that exponentially decays as a function of the internal Rossby Radius of deformation. This assumes that flow in the channel will be almost geostrophic. However, Münchow [2016] found that observations during the 2007-2009 period were not well-described by geostrophy. He attributes this to the lack of land-fast ice seasons that lead to wind dominated flow patterns. Furthermore, LeBlond [1980] suggests that the channels of the CAA are often characterized by across-channel density interface that slopes in opposition to surface slope (Figure 3.11). Such a density structure would lead to a quiescent bottom flow under geostrophy. However, the model's algorithms are based on a density gradient independent of depth and constant across the channel,

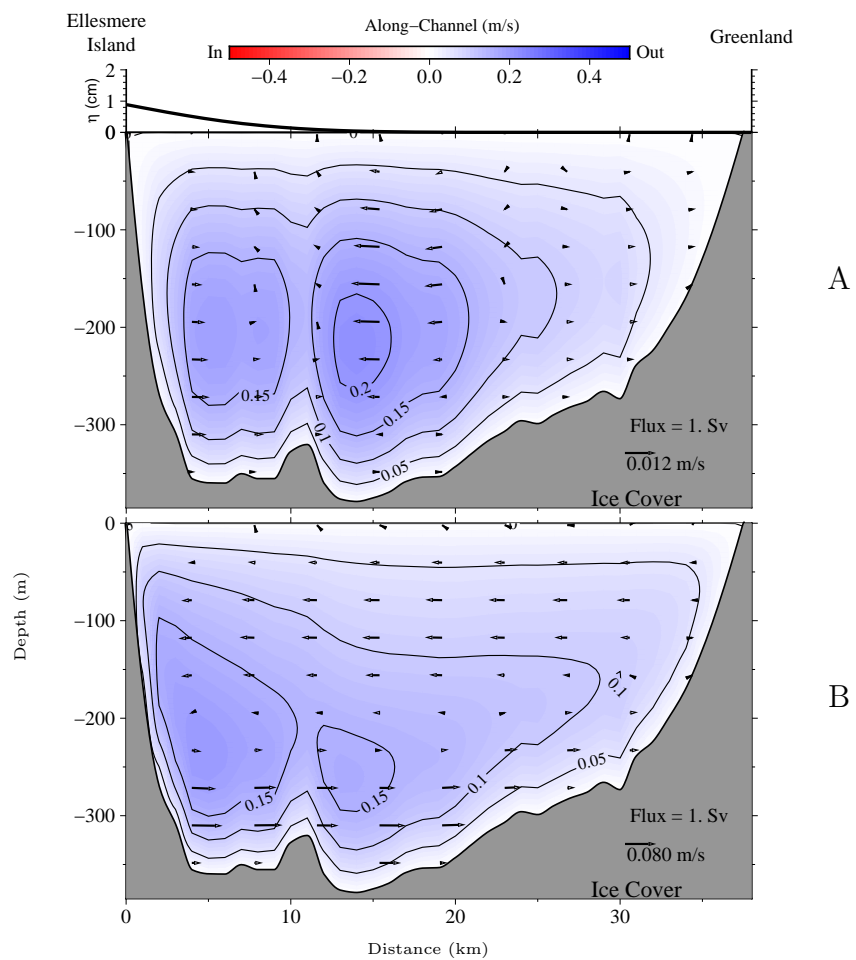


Figure 3.10: Run 4 - Modeled velocities for a land-fast ice cover. Ekman depth is 350 m (A) and 70 m (B).

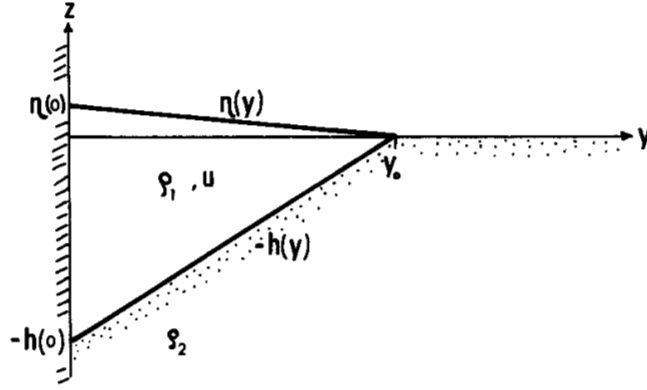


Figure 3.11: Schematic cross-section of a coastal upper layer flow of speed u (out of the page) driven by a sea-surface slope $\eta(y)$; the lower layer, of density ρ_2 is at rest because the interface $h(y)$ slopes in a direction opposite to that of the free surface. y_0 is the distance from the coast at which the thickness of the upper layer vanishes. [LeBlond, 1980].

that is, $\frac{\partial D}{\partial z} = \frac{\partial D}{\partial y} = 0$. This limitation prevents any consideration of an oppositional across-channel density gradient below the surface. Another limiting factor in the model is the assumption of constant viscosity. Allowing this parameter to vary with depth would permit the frictional effects of winds and those of the bottom boundary to be uncoupled.

Adopting a high viscosity assumption in the model does result in a flow pattern that approaches observations. I have identified that the range of winds present in Nares Strait effects the flow of water and ice in the channel. Persistent strong up-channel winds will result in a surface flow reversal. However, simulating this response in the model requires amplification of the drag coefficient to adequately reflect the effects of wind stress. This amplification is unsupported in the literature. The potential exists that tuning the model further could produce surface velocities that more closely match observations. However, I hesitate to pursue this tactic and will attempt to calculate ice flux in the next chapter without use of the model's simulations.

To study channel flow during land-fast ice periods, and to explore if geostrophic flow patterns could be achieved by the model when winds are not a factor, a frictional

no-slip surface modification was implemented. The model does a better job of simulating observations with a lower viscosity assumption than required by the wind stress version. However, this is not helpful for my stated goal of supplementing sparse ice velocity data.

Chapter 4

ICE FLUX THROUGH NARES STRAIT 2003-2009

4.1 Introduction

Of the two pathways for ice to advect from the Arctic to the North Atlantic, Fram Strait to the east of Greenland dominates ice export year-round in terms of volume [Aagaard and Carmack, 1989]. However, the thickest ice, may leave the Arctic via the Canadian Arctic Archipelago. Bourke and Garrett [1987], Haas et al. [2006], Maslanik et al. [2007] find the thickest ice in the Arctic to be located north of the CAA. Nares Strait, which forms the eastern boundary of the CAA, separates Northwest Greenland from Ellesmere Island, Canada. It is a conduit of multi-year ice from the Arctic Ocean to the North Atlantic [Kwok et al., 2010, Ryan and Münchow, 2017]. The channel, that narrows to nearly 20 km, has been estimated to transport between 33 km³ (2003) and 254 km³ (2007) of ice annually [Kwok et al., 2010]. In comparison, Fram Strait has been estimated to transport 2400 km³ yr⁻¹ [Widell et al., 2003] to 2600 km³ yr⁻¹ [Spreen et al., 2009].

Due in large part to its width, Nares Strait has been generally parameterized rather than explicitly modeled in global climate models. In order to increase our understanding of the ice that is transported through the channel, estimate temporal variability and to provide insight to modelers who must incorporate this narrow channel into global climate simulations, I now seek to estimate the potential advective flux of this Arctic ice to the south. More specifically, I will quantify ice volume flux for the 2003 to 2009 period from sensors moored in Nares Strait. During this period, the channel was open to free-flowing ice nearly year-round for several years. In changing climate conditions, the land-fast-free condition may become more probable. This study

will provide physical insight to facilitate dynamical prediction through observations of both ice velocity and draft variations in a changing climate. Thus by validation of prior estimates of ice flux by Kwok et al. [2010], I provide another metric against which to evaluate model predictions of climate physics and their changes over time.

Earlier ice transport estimates for Nares Strait [Kwok, 2005, Kwok et al., 2010] were derived using remote sensing techniques for ice area and velocity at daily time scales. Ice thickness estimates were averaged annually and at a channel-wide scale in space. Here, I use ice draft and velocity time series from Ryan and Münchow [2017] to estimate ice flux and annual volume transport through the channel. This in-situ monitoring with moored instruments provides high temporal resolution ice thickness ($dt = 15$ s) and velocity ($dt = 3$ hr) measurements. Between 2003 and 2006, ice drafts were measured with ice profiling sonars at two locations in the channel [Ryan and Münchow, 2017]. Simultaneously, ice velocities were recorded using acoustic doppler current profilers at four locations (Figure 4.1). I also evaluate the period between 2007 and 2009 where only one IPS measured the ice drafts passing through the channel and five ADCP's measured velocity (Figure 4.2). I then use these time series to quantify how ice flux varies at monthly to inter-annual time scales.

4.2 Data Methods

4.2.1 Ice flux and volume transport

I herein calculate ice flux R as along-channel ice velocity V , multiplied by the ice thickness H , integrated across the channel of width B

$$R = \int_0^B H(y, t)V(y, t) dy \quad (4.1)$$

where $H = \frac{D}{0.9}$ and D is the ice draft with an assumed draft to thickness ratio of 0.9. The ice volume transport T , through a channel between times t_1 and t_2 is the time integral of flux

$$T = \int_{t_1}^{t_2} R dt. \quad (4.2)$$

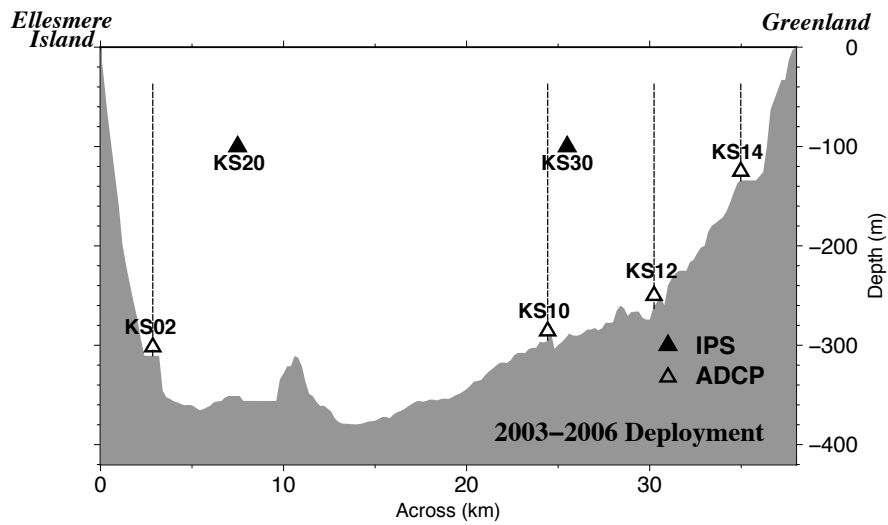


Figure 4.1: Cross-section of Nares Strait with symbols showing location of the IPS and ADCP moorings between 2003-2006.

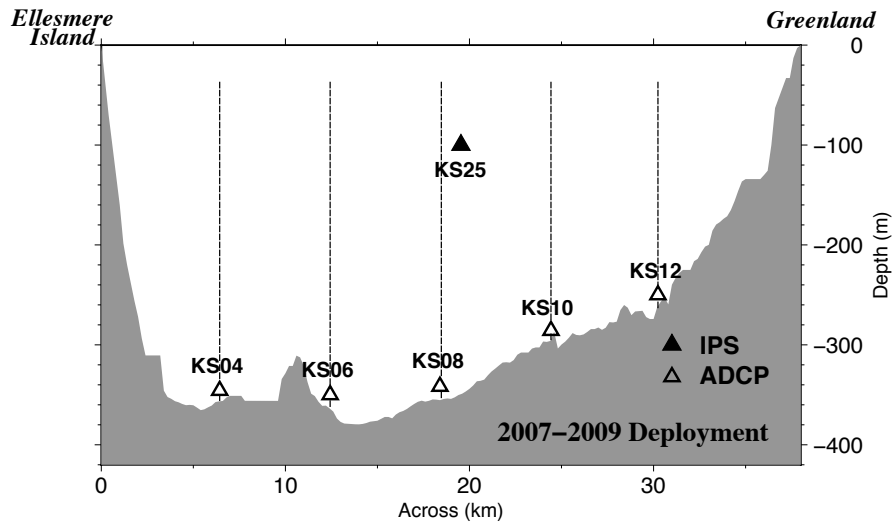


Figure 4.2: Cross-section of Nares Strait with symbols showing location of the IPS and ADCP moorings between 2007-2009.

4.3 Across-channel Variability

In order to calculate annual ice transport and flux with discrete observations in space, assumptions must be made as to how ice velocity and thickness vary across the channel. I here describe the methods used to estimate both ice draft and ice velocity at each point across the channel from our time series of observations.

4.3.1 Ice draft

Two IPS provide ice draft in the channel from 2003 to 2006. For this period, I assume that ice draft varies linearly across the channel. Between 2007 and 2009, there is only one ice draft measurement when an IPS was moored at KS25, a central location in the channel (Figure 4.2). I seek an estimate of how the thickness of mobile ice varies across the channel. I exploit the data from the two ice profiling sonars of the first deployment to estimate the across-channel variation in draft for the second deployment. I thus assume that ice draft varies across the channel with constant slope of -2.96×10^{-5} which is the mean for all free-flowing ice periods between 2003 and 2006.

4.3.2 Ice velocity

Münchow [2016] finds surface velocity that is strongest in the central channel. The ADCP locations for the 2003-2006 deployment were not evenly distributed across Nares Strait (Figure 4.1). Approximately 18 km of the central channel lack ice velocity observations. Three of the four ADCP moorings are in the half of the channel nearest Greenland and the remaining one is within 3 km of Ellesmere Island. However, ice velocity data during the 2007-09 period is well-resolved in the central channel (Figure 4.2). I compare mean ice velocity observations at each location for both periods. Figure 4.3 shows the mean velocity during free-flow ice periods at each location by deployment. Solid circles and squares mark the observed data. Dotted lines connect observations that are further than 6 km apart. The most intense mean flow is found at KS08. This is the location of the channel where data is lacking in the first deployment. This

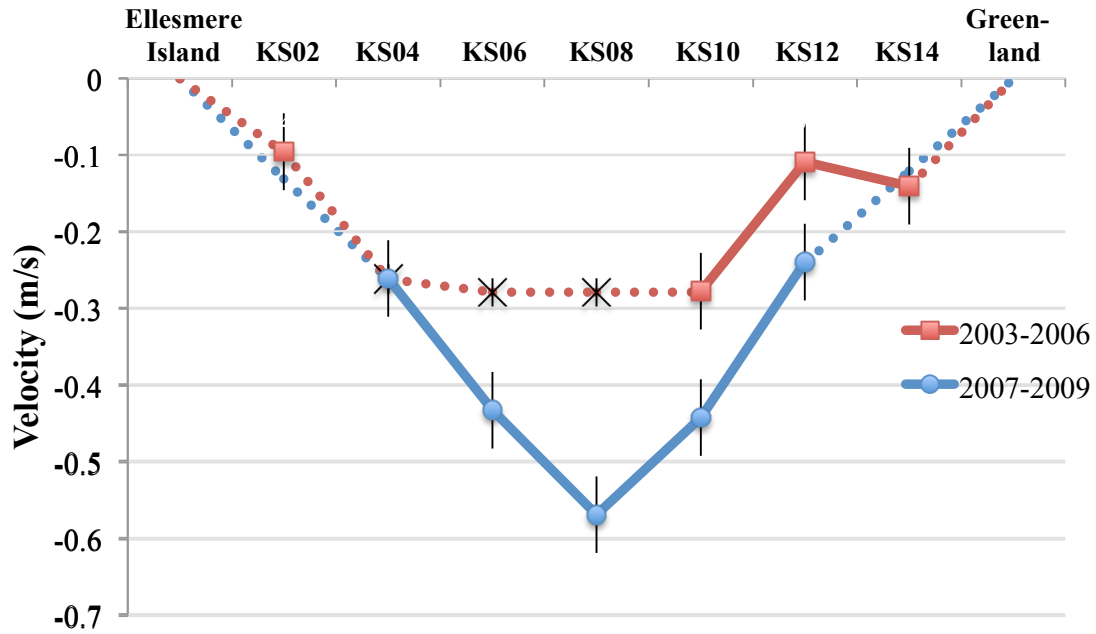


Figure 4.3: Mean ice velocity during free flow ice periods 2003-06 (red) and 2006-09 (blue). Black symbols indicate mean velocity assumption between 2003 and 2006. Dotted lines connect observations separated by more than 6 km.

indicates that a simple linear assumption is inappropriate to approximate ice velocities across the channel given the observation locations between 2003 and 2006.

4.3.3 Piece-wise linear velocity profile

For the 2007-09 deployment, I will assume that ice velocity at each coast is zero and varies linearly between each of the observation locations. However, assuming linearity between KS02 and KS12 would be expected to result in underestimating ice velocity for the 2003-06 deployment. To estimate velocity in the central channel, I consider two methods of compensation for the spatial gap in data. The first is to estimate ice velocity at KS08 by a linear extrapolation of the the well-resolved eastern portion of the channel. I do this with a linear fit to the observations at KS10 and KS12 to find the velocity at any point between KS08 and KS12. To test the validity of this method, I apply it to the 2007-09 deployment. The resulting root mean square error

(RMSE) between derived and observed ice velocities at KS08 is 0.41 m s^{-1} and for the average across all stations is 0.13 m s^{-1} . Generally, this results in a higher outflow velocity.

The second method is an assumption that the ice velocity between the KS04 and KS10 locations is constant and equal to the observation at KS10. For this method, the RMSE is 0.26 m s^{-1} at KS08 and for the average across all stations it is 0.10 m s^{-1} . This assumption generally results in lower outflow velocities than observed at KS08. I will adopt the second method to estimate along-channel ice velocities for the first deployment period.

4.4 Ice Flux

Ice flux is computed hourly assuming that ice velocities estimated every 3 hours are constant over the period. Figure 4.4 shows this ice flux; a low-pass Lanczos filter with a half-power point near 30 days was applied. Ice flux thus varies from tidal to decadal scales about a mean of $291 \pm 88 \text{ km}^3 \text{ yr}^{-1}$. Integrating this from 1 September through 31 August of each year provides annual ice transport. Inter-annually, this varies from 138 ± 76 to $532 \pm 154 \text{ km}^3$ (Table 4.1). As ice flux is a product of two independent data sets, draft and velocity, each subject to random error, δD (0.1m) and δV (0.05 m s^{-1}) respectively, my error estimate is $\delta R = |R| \sqrt{\left(\frac{\delta D}{D}\right)^2 + \left(\frac{\delta V}{V}\right)^2}$. This error was calculated for the draft and velocity record for each year.

I note that the velocity profile chosen for the early period effects the estimate of flux. To assess the impact this assumption has on the 2003-2006 estimates, I calculate the flux for 2007-2009 using similar assumptions. That is the velocity measured at KS10 is used for the section of the channel between KS04 and KS10. This resulted in a two percent difference in the flux estimate for the period.

4.4.1 Analysis

Comparing the two deployments, annual ice volume transport for the early period is lower with an average between 2003 and 2006 of $171 \pm 62 \text{ km}^3$ as compared

to $472 \pm 126 \text{ km}^3$. This is consistent with the ice bridge formation that persisted from 3 to 6 months of the first three years while it did not in the later period. Winds were stronger and ice velocities were higher between 2007 and 2009.

To put these values into the context of other estimates for ice transport through Nares Strait, Figure 4.5 compares my estimates of ice transport for each year of our record to those that overlap from Kwok et al. [2010]. My estimates are higher in each instance. Whereas Kwok et al. [2010] estimate ice transport from the Arctic basin through the Lincoln Sea entrance to Nares Strait, my observations are more than 200 km down-channel. They therefore include the ice from the Arctic basin, ice that forms or thickens in the channel and ice that enters the channel from inlets and fjords that open into Nares Strait between the Lincoln Sea and the moorings. Nonetheless, the comparison is interesting. My estimate of ice transport is always higher. In three of the four years of overlap, the difference between the two is roughly 50 to 100 km^3 and is less than my error estimate in 2003-04. However, in the 2007-08 year, my estimate exceeds that of Kwok et al. [2010] by nearly 350 km^3 .

There are several possible explanations for this disagreement.

- The method I use to estimate across-channel ice thickness variability is different than in the other overlapping years due to the single IPS deployment. Generally, ice is thicker near Ellesmere Island, so that an overstatement in the magnitude of the slope $\overline{m_{D_1}}$ might lead to a high transport estimate. In order to assess the possible contribution of this assumption, I calculate ice flux with a constant ice thickness across the channel based on a single observation at KS25. That is, in effect, assuming $\overline{m_{D_1}}=0$. That assumption reduces the annual transport by 13 km^3 . Likewise, I calculate the ice flux between 2003 and 2006 assuming the constant slope and the IPS ice draft observation at KS30. This results in a +12% to -19% difference in the calculated flux each year. So the difference in transport estimates in 2007-08 is not likely to be solely due to errors in the assumed across-channel ice draft profile.

- Whereas I measure ice drafts over the entire time period, estimates by Kwok

et al. [2010] are based on an average ice thickness from earlier field observations. Perhaps this estimate is low. Perhaps velocity estimates by Kwok et al. [2010] are biased low during this typically land-fast ice season? Could the feature tracking algorithm used by Kwok et al. [2010] have been less effective with smaller, thinner or more rapidly moving ice? This is a plausible explanation.

- Much more ice could have formed in Nares Strait and its fjords than in other years. As this ice would not have passed through the Lincoln Sea as ice sufficiently thick to be detected remotely, it would not have been observed by Kwok et al. [2010]. Without a land-fast ice cover to insulate the ocean from the atmosphere and a bridge in the channel to block ice flow, new ice can form throughout the winter and would be allowed to freely advect.

I conclude that all but the first proposition are plausible explanations for the difference in our ice flux estimates. I suggest that the most likely causes are a low ice thickness estimate in the summer of 2007 and/or opportunistically forming first year ice that would not have been able to form in other years. The former highlights the benefit of a moored system to provide observations at high temporal resolution. If we assume feature tracking of smaller, thinner and faster ice floes is to blame, it is not the temporal resolution but the moored system's sensitivity to measure ice of smaller scales (both horizontally and vertically) that recommends it.

To put this ice flux into a broader perspective, I compare ice transport through Nares Strait to that for Fram Strait. The along-channel winds and strong currents in Nares Strait control ice velocity during the mobile ice season. Average ice velocity in Nares Strait during mobile ice season exceeds 0.35 m s^{-1} . In Fram Strait ice velocities are about half that [Widell et al., 2003]. However, the seasonal blockage characteristic of Nares Strait does not occur in Fram Strait where flow is year-round. Whereas ice flux through Fram Strait has been estimated to be $2400 \text{ km}^3 \text{ yr}^{-1}$ [Widell et al., 2003] to $2600 \text{ km}^3 \text{ yr}^{-1}$ [Spren et al., 2009], our record average indicates that Nares Strait transports approximately 12% of that volume. Due to inter-annual variability, however, we found that Nares Strait ice transport varies between 6 and 21% of that for Fram

Ice Flux

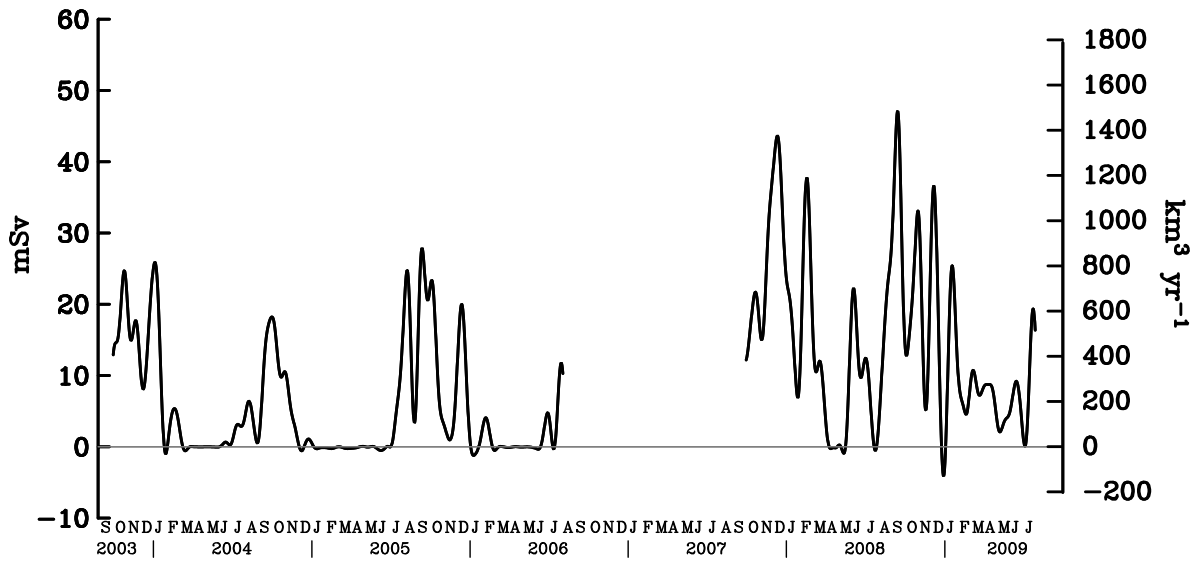


Figure 4.4: Ice flux through Nares Strait from 2003 to 2006 and from 2007 to 2009. A low-pass Lanczos filter was applied (~ 30 days half-power point). Positive values are down-channel outflows.

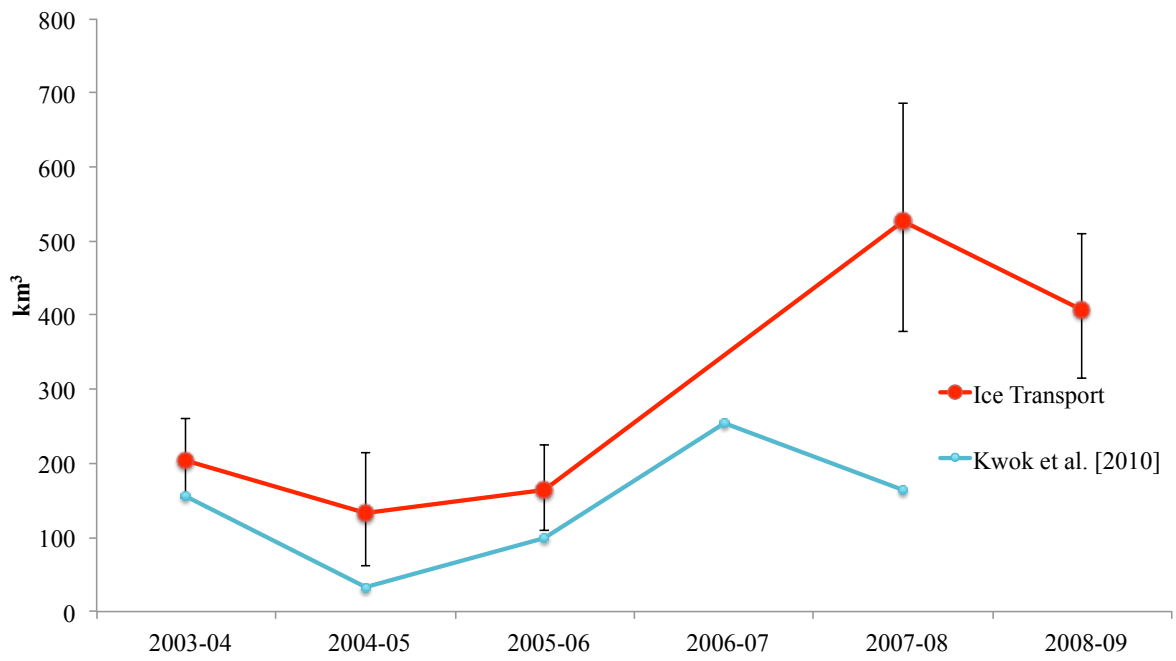


Figure 4.5: Annual ice transport through Nares Strait from 2003 to 2006 and from 2007 to 2009. My estimates (red) are compared to those of [Kwok et al. \[2010\]](#) (blue).

Table 4.1: Ice transport statistics.

Year		Ice Transport (km ³)	Land-fast Ice Season (Days)
2003-04		207 ±53	102
2004-05		138 ±76	182
2005-06	*	167 ±58	122
2007-08		532 ±154	47
2008-09	*	412 ±98	0
Average		312 ±89	91

*Data terminates on 9 August 2006
and on 31 July 2009.

Strait.

Moreover, the timing of our largest transport of ice, in 2007-08, coincides with the thinning trend observed between 2003-2008 in Fram Strait by [Hansen et al. \[2013\]](#) and [Renner et al. \[2014\]](#). In contrast, observations indicate no such trend in Nares Strait [[Ryan and Münchow, 2017](#)].

4.5 Conclusion

I have shown here that despite limitations that arose due to instrument failure or loss, I was able to exploit data from each deployment to make informed assumptions about the other. Across-channel ice thickness variability from the first deployment provided an across-channel thickness profile for the second, and ice velocity profiles from the second provided insight on appropriate methods of interpolation for the first. The calculations based on these informed assumptions result in a time series of ice flux through Nares Strait over 5 years. The record includes years of long-lasting land-fast ice seasons of up to 6 months as well as one year with no land-fast season at all. When an ice bridge fails to form or collapses quickly in Nares Strait, as it did in 2007 and 2008, the channel is open to ice transport year round. The traditional land-fast season coincides with the strongest wind velocities in Nares Strait. This strong

atmospheric forcing led to amplified ice velocities in 2007 through 2008. This resulted in ice transport nearly 4 times that of 2004-05. Since Nares Strait has been generally parameterized rather than explicitly modeled in global climate models, I hope that these ice flux estimates under a variety of land-fast ice scenarios will improve modelers' ability to incorporate the relatively narrow channel into large-scale models.

Chapter 5

DISCUSSION OF FINDINGS

Here I summarize the findings of my research as presented in this dissertation. I also seek to answer the questions posed in Chapter 1 within the context of this summary.

5.1 Ice Draft and Velocity

I calculated ice draft from a 9-year data set of ice profiling sonar observations. These time series of ice draft along with ice velocity observations from Nares Strait between 2003 and 2012 provide new insights on the statistical properties of sea ice leaving the Arctic to the Atlantic Ocean. Whereas median ice draft is 0.8 m, it varies annually from 1.5 m (2007-08) to 0.5 m (2008-09). Probability density distributions of sea ice draft depend on location across the channel with thicker ice near Canada and thinner ice near Greenland. Likewise, ice velocities vary across the channel, increasing with distance from the coasts. They are strongest mid-channel where average velocity approached 0.6 m s^{-1} (2007-09). However, sea ice motion usually stops seasonally due to arching land-fast ice that spans the channel for up to 190 days per year as it does during the 2011-12 winter. In contrast the 2006 to 2010 period exhibits a single ice arch lasting 47 days in April/May of 2008. When a land-fast cover does not form as the result of a down-channel ice bridge, ice flux is enhanced by strongest winds characteristic of the typically land-fast ice season.

5.2 Multi-year Ice Trends

As we witness the loss of multi-year ice in the Arctic, climate modelers seek to predict the seasonal conditions in that region under a changing climate. Nares Strait

has the potential to influence the longevity of the multi-year ice cover that insulates the polar sea from the warming effects of summer's solar radiation. Rather than a thinning trend found in Fram Strait, I find high inter-annual variability in the distribution of thick ice (> 5 m). This constitutes between 9% (2003-04) and 16% (2007-08) of the observed sea ice. The probability $g(D)$ of this thick, ridged, multi-year ice decays exponentially with draft D at an e-folding scale D_0 of 3.0 ± 0.2 m. The trend of D_0 with time is statistically indistinguishable from zero. This observation suggests a steady export of multi-year sea ice at decadal time scales.

5.3 Semianalytic Model of Channel Flow

Seeking to calculate ice flux through Nares Strait, I implemented a semianalytic model to simulate ice velocity at various locations across the channel. I used wind stress and a drag coefficient to model ice motion along the water surface. Unfortunately, I found limitations in the ability of the model to simulate surface velocities with realistic parameters of Kelvin and Ekman numbers for Nares Strait. I therefore used a method of regression to estimate along-channel ice velocity as it varies across the channel.

5.4 Ice Flux

Inter-annually, ice transport through Nares Strait varied from 138 ± 76 to 532 ± 154 km³ about a mean of 291 ± 88 km³. I attribute most of this variability to the duration of land-fast ice seasons in Nares Strait. Ice transport through the channel averages 12% of that through Fram Strait. However, due to inter-annual variability, the ratio ranges from 6% to 21%. Should Nares Strait be subject to shorter or less frequent land-fast ice seasons, I would expect this ratio to rise over time. To assess an upper limit, flux has approached 1600 km³ yr⁻¹ at time scales of several weeks. If this rate were to persist year-round, Nares Strait would transport up to 70% of the Fram Strait transport.

5.5 Conclusion

I have demonstrated that ice plays an important role in Nares Strait and that Nares Strait plays an important role with respect to ice that leaves the Arctic. I have examined the ice of the channel over nine years. Most years, a supply of sufficiently thick ice passes through the channel and converges to form a resilient ice bridge. At that time, all ice motion up-channel of the bridge ceases. When Nares Strait was open to free flowing ice year-round, annual transport of ice was increased by a factor of nearly 3 as compared to during years that the seasonal ice bridge formed to block ice flow. This increased flux leads to the conclusion that recurrent absence of a land-fast ice bridge in Nares Strait would hasten the onset of an ice-free Arctic Basin. Although Nares Strait is unlikely to exceed Fram Strait in transport of sea ice, its relative contribution to Arctic ice export is not trivial. Furthermore, as the Arctic Ocean's reservoir of multi-year ice dwindles, the last of this climatologically precious resource found to the north of Ellesmere Island and Greenland may exit the Arctic Basin through Nares Strait rather than Fram Strait.

5.6 Future Work

In working with the channel-flow model, I became interested in air/ice/ocean transfers of momentum. Calculation of these require measurements of ice draft into the water column and freeboard height into the atmosphere as well as roughness scales at both surfaces. Ice draft measurements provide a direct means to estimate roughness at the bottom of the ice. If a hydrostatic balance is assumed, freeboard and perhaps even a top surface roughness estimate could also be achieved.

Despite my inability to use the model to derive ice velocities in this work, I enjoyed programming and working with it. It would be interesting to explore allowing the viscosity to vary with depth and the density gradient to vary in both depth and across the channel. I believe that these modifications could improve its ability simulate flows in an Arctic channel like Nares Strait.

Having gone to sea for research several times, I am generally inclined to seek observational data. To develop a better understanding of temporal trends in Nares Strait, extending the time series of ice draft and velocity with additional observations would be beneficial. Nine years of Arctic data is admittedly quite long. The opportunity to study Nares Strait at a time of such variability was invaluable in many ways. However, that very variability may have masked an underlying trend. By adding a few years of observational data, one might be able to discern changes as they evolve over time.

BIBLIOGRAPHY

- K. Aagaard and E. C. Carmack. The role of sea ice and other fresh water in the Arctic circulation. *Journal of Geophysical Research-Oceans*, 94(C10):14485–14498, 15 Oct 1989. doi: 10.1029/JC094iC10p14485.
- R.J. Anderson. Wind stress measurements over rough ice during the 1984 marginal ice-zone experiment. *Journal of Geophysical Research-Oceans*, 92(C7):6933–6941, 30 Jun 1987. ISSN 2169-9275. doi: 10.1029/JC092iC07p06933.
- D. R. Blidberg, R. W. Corell, and A. S. Westneat. Probable ice thickness of the Arctic Ocean. *Coastal Engineering*, 5(2-3):159–169, 1981. ISSN 0378-3839. doi: 10.1016/0378-3839(81)90013-2.
- R. H. Bourke and R. P. Garrett. Sea ice thickness distribution in the Arctic Ocean. *Cold Regions Science and Technology*, 13(3):259–280, Apr 1987. ISSN 0165-232X. doi: 10.1016/0165-232X(87)90007-3.
- Canadian Ice Service. Sea ice climatic atlas northern Canadian waters 1981-2010. Technical report, Canadian Ice Service, Ottawa, Ontario, Canada, 2011.
- J. C. Comiso and F. Nishio. Trends in the sea ice cover using enhanced and compatible AMSR-E, SSM/I, and SMMR data. *Journal of Geophysical Research-Oceans*, 113 (C2), 22 Feb 2008. ISSN 2169-9275. doi: 10.1029/2007JC004257.
- D. Dumont, Y. Gratton, and T. E. Arbetter. Modeling the dynamics of the North Water Polynya ice bridge. *Journal of Physical Oceanography*, 39(6):1448–1461, Jun 2009. ISSN 0022-3670. doi: 10.1175/2008JPO3965.1.
- M. Dunbar. Ice regime and ice transport in Nares Strait. *Arctic*, 26(4):282–191, 1973.
- M. Dunbar and M. J. Dunbar. 21.—The History of the North Water. *Proceedings of the Royal Society of Edinburgh. Section B. Biology*, 72:231–241, Jan 1972. ISSN 0269-7270. doi: 10.1017/S0080455X00001788.
- H. Eicken and M. A. Lange. Sea ice thickness data - the many vs the few. *Geophysical Research Letters*, 16(6):495–498, Jun 1989. ISSN 0094-8276. doi: 10.1029/GL016i006p00495.

- S. L. Farrell, N. Kurtz, L. N. Connor, B. C. Elder, C. Leuschen, T. Markus, D. C. McAdoo, B. Panzer, J. Richter-Menge, and J. G. Sonntag. A first assessment of IceBridge snow and ice thickness data over Arctic sea ice. *IEEE Transactions On Geoscience And Remote Sensing*, 50(6):2098–2111, Jun 2012. ISSN 0196-2892. doi: 10.1109/TGRS.2011.2170843.
- C. Haas, S. Hendricks, and M. Doble. Comparison of the sea-ice thickness distribution in the Lincoln Sea and adjacent Arctic Ocean in 2004 and 2005. volume 44 of *Annals of Glaciology*, pages 247–252, Lensfield Rd, Cambridge CB2 1ER, England, 2006. Int Glaciol Soc; Univ Otago; Natl Inst Water & Atmospher Res; Royal Soc New Zealand, Int. Glaciological Society. ISBN 978-0-946417-39-1. doi: 10.3189/172756406781811781. International Symposium on Sea Ice, Dunedin, New Zealand, 05-09 Dec 2005.
- E. Hansen, S. Gerland, M. A. Granskog, O. Pavlova, A. H. H. Renner, J. Haapala, T. B. Loynning, and M. Tschudi. Thinning of Arctic sea ice observed in Fram Strait: 1990-2011. *Journal of Geophysical Research-Oceans*, 118(10):5202–5221, Oct 2013. ISSN 2169-9275. doi: 10.1002/jgrc.20393.
- W. D. Hibler. Dynamic thermodynamic sea ice model. *Journal of Physical Oceanography*, 9(4):815–846, 1979. ISSN 0022-3670. doi: 10.1175/1520-0485(1979)009<0815:ADTSIM>2.0.CO;2.
- H. Huntley and P. A. Ryan. Wind Effects on Flow Patterns and Net Fluxes in Density-Driven High-Latitude Channel Flow. *Journal of Geophysical Research-Oceans*, 123(1):305–323, Jan 2018. ISSN . doi: 10.1002/2017JC012748.
- M. E. Johnston. A decade of probing the depths of thick multi-year ice to measure its borehole strength. *Cold Regions Science and Technology*, 99:46–65, Mar 2014. ISSN 0165-232X. doi: 10.1016/j.coldregions.2013.12.002.
- A. Kasai, A. E. Hill, T. Fujiwara, and J. H. Simpson. Effect of the Earth’s rotation on the circulation in regions of freshwater influence. *Journal of Geophysical Research-Oceans*, 105(C7):16961–16969, 15 Jul 2000. ISSN 0148-0227. doi: 10.1029/2000JC900058.
- J. E. Kay, M. M. Holland, and A. Jahn. Inter-annual to multi-decadal Arctic sea ice extent trends in a warming world. *Geophysical Research Letters*, 38, 11 Aug 2011. ISSN 0094-8276. doi: 10.1029/2011GL048008.
- N. T. Kurtz, S. L. Farrell, M. Studinger, N. Galin, J. P. Harbeck, R. Lindsay, V. D. Onana, B. Panzer, and J. G. Sonntag. Sea ice thickness, freeboard, and snow depth products from Operation IceBridge airborne data. *Cryosphere*, 7(4):1035–1056, 4 July 2013. ISSN 1994-0416. doi: 10.5194/tc-7-1035-2013.

- R. Kwok. Variability of Nares Strait ice flux. *Geophysical Research Letters*, 32(24): L24502, Dec 2005. ISSN 0094-8276. doi: 10.1029/2005GL024768.
- R. Kwok. Sea ice convergence along the Arctic coasts of Greenland and the Canadian Arctic Archipelago: Variability and extremes (1992-2014). *Geophysical Research Letters*, 42(18):7598–7605, 28 Sep 2015. ISSN 0094-8276. doi: 10.1002/2015GL065462.
- R. Kwok and G. F. Cunningham. Contribution of melt in the Beaufort Sea to the decline in Arctic multiyear sea ice coverage: 1993-2009. *Geophysical Research Letters*, 37, 19 Oct 2010. ISSN 0094-8276. doi: 10.1029/2010GL044678.
- R. Kwok and G. F. Cunningham. Contributions of growth and deformation to monthly variability in sea ice thickness north of the coasts of Greenland and the Canadian Arctic Archipelago. *Geophysical Research Letters*, 43(15):8097–8105, 16 Aug 2016. ISSN 0094-8276. doi: 10.1002/2016GL069333.
- R. Kwok, L. T. Pedersen, P. Gudmandsen, and S. S. Pang. Large sea ice outflow into the Nares Strait in 2007. *Geophysical Research Letters*, 37:L03502, Feb 2010. ISSN 0094-8276. doi: 10.1029/2009GL041872.
- R. Kwok, G. F. Cunningham, M. Wensnahan, I. Rigor, H. J. Zwally, and D. Yi. Thinning and volume loss of the Arctic Ocean sea ice cover: 2003-2008. *Journal of Geophysical Research-Oceans*, 114, 7 Jul 2009. ISSN 0148-0227. doi: 10.1029/2009JC005312.
- R. Kwok, G. Spreen, and S. Pang. Arctic sea ice circulation and drift speed: Decadal trends and ocean currents. *Journal of Geophysical Research-Oceans*, 118(5):2408–2425, May 2013. ISSN 2169-9275. doi: 10.1002/jgrc.20191.
- S. W. Laxon, K. A. Giles, A. L. Ridout, D. J. Wingham, R. Willatt, R. Cullen, R. Kwok, A. Schweiger, J. Zhang, C. Haas, S. Hendricks, R. Krishfield, N. Kurtz, S. Farrell, and M. Davidson. CryoSat-2 estimates of Arctic sea ice thickness and volume. *Geophysical Research Letters*, 40(4):732–737, 28 Feb 2013. ISSN 0094-8276. doi: 10.1002/grl.50193.
- P. H. LeBlond. On the surface circulation in some channels of the Canadian Arctic Archipelago. *Arctic*, 33(1):189–197, 1980. ISSN 0004-0843.
- J. Maslanik, J. Stroeve, C. Fowler, and W. Emery. Distribution and trends in Arctic sea ice age through spring 2011. *Geophysical Research Letters*, 38, 14 Jul 2011. ISSN 0094-8276. doi: 10.1029/2011GL047735.
- J. A. Maslanik, C. Fowler, J. Stroeve, S. Drobot, J. Zwally, D. Yi, and W. Emery. A younger, thinner Arctic ice cover: Increased potential for rapid, extensive sea-ice loss. *Geophysical Research Letters*, 34(24), 22 Dec 2007. ISSN 0094-8276. doi: 10.1029/2007GL032043.

- G. A. Maykut and N. Untersteiner. Some results from a time-dependent thermodynamic model of sea ice. *Journal of Geophysical Research*, 76(6):1550–&, 1971. ISSN 0148-0227. doi: 10.1029/JC076i006p01550.
- P. C. McIntosh. Oceanographic data interpolation - objective analysis and splines. *Journal of Geophysical Research-Oceans*, 95(C8):13529–13541, 15 Aug 1990. ISSN 0148-0227. doi: 10.1029/JC095iC08p13529.
- G. A. Meehl, W. M. Washington, J. M. Arblaster, A. Hu, H. Teng, C. Tebaldi, B. N. Sanderson, J-F Lamarque, A. Conley, W. G. Strand, and J. B. White, III. Climate system response to external forcings and climate change projections in CCSM4. *Journal of Climate*, 25(11):3661–3683, 1 Jun 2012. ISSN 0894-8755. doi: 10.1175/JCLI-D-11-00240.1.
- H. Melling and D. A. Riedel. The underside topography of sea-ice over the continental-shelf of the Beaufort Sea in the winter of 1990. *Journal of Geophysical Research-Oceans*, 100(C7):13641–13653, 15 Jul 1995. ISSN 0148-0227. doi: 10.1029/95JC00309.
- H. Melling, P. H. Johnston, and D. A. Riedel. Measurements of the underside topography of sea-ice by moored subsea sonar. *Journal of Atmospheric and Oceanic Technology*, 12(3):589–602, Jun 1995. ISSN 0739-0572. doi: 10.1175/1520-0426(1995)012.
- H. Melling, Y. Gratton, and G. Ingram. Ocean circulation within the North Water Polynya of Baffin Bay. *Atmosphere-Ocean*, 39(3):301–325, Sep 2001. ISSN 0705-5900.
- A. Münchow. Volume and Freshwater Flux Observations from Nares Strait to the West of Greenland at Daily Time Scales from 2003 to 2009. *Journal of Physical Oceanography*, 46(1):141–157, Jan 2016. ISSN 0022-3670. doi: 10.1175/JPO-D-15-0093.1.
- A. Münchow and H. Melling. Ocean current observations from Nares Strait to the west of Greenland: Interannual to tidal variability and forcing. *Journal of Marine Research*, 66(6):801–833, Nov 2008. ISSN 0022-2402.
- A. Münchow, H. Melling, and K. K. Falkner. An observational estimate of volume and freshwater flux leaving the Arctic Ocean through Nares Strait. *Journal of Physical Oceanography*, 36(11):2025–2041, Nov 2006. ISSN 0022-3670.
- A. Münchow, K. K. Falkner, and H. Melling. Spatial continuity of measured seawater and tracer fluxes through Nares Strait, a dynamically wide channel bordering the Canadian Archipelago. *Journal of Marine Research*, 65(6):759–788, Nov 2007. ISSN 0022-2402.
- A. Münchow, K. K. Falkner, H. Melling, B. Rabe, and H. L. Johnson. Ocean warming of Nares Strait bottom waters off northwest Greenland, 2003-2009. *Oceanography*, 24(3, SI):114–123, Sep 2011. ISSN 1042-8275.

- A. Münchow, L. Padman, and H. A. Fricker. Interannual changes of the floating ice shelf of Petermann Gletscher, North Greenland, from 2000 to 2012. *Journal of Glaciology*, 60(221):489–499, 2014. ISSN 0022-1430. doi: 10.3189/2014JoG13J135.
- D. Perovich, J. Richter-Menge, C. Polashenski, B. Elder, T. Arbetter, and O. Brennick. Sea ice mass balance observations from the North Pole Environmental Observatory. *Geophysical Research Letters*, 41(6):2019–2025, 28 Mar 2014. ISSN 0094-8276. doi: 10.1002/2014GL059356.
- A. Preußner, G. Heinemann, S. Willmes, and S. Paul. Multi-Decadal Variability of Polynya Characteristics and Ice Production in the North Water Polynya by Means of Passive Microwave and Thermal Infrared Satellite Imagery. *Remote Sensing*, 7(12):15844–15867, Dec 2015. ISSN 2072-4292. doi: 10.3390/rs71215807.
- B. Rabe, A. Münchow, H. L. Johnson, and H. Melling. Nares Strait hydrography and salinity field from a 3-year moored array. *Journal of Geophysical Research-Oceans*, 115:C07010, Jul 2010. ISSN 0148-0227. doi: 10.1029/2009JC005966.
- B. Rabe, H. L. Johnson, A. Münchow, and H. Melling. Geostrophic ocean currents and freshwater fluxes across the Canadian polar shelf via Nares Strait. *Journal of Marine Research*, 70(4):603–640, Jul 2012. ISSN 0022-2402.
- T. A. S. Rasmussen, N. Kliem, and E. Kaas. Modelling the sea ice in the Nares Strait. *Ocean Modelling*, 35(3):161–172, 2010. ISSN 1463-5003. doi: 10.1016/j.ocemod.2010.07.003.
- T. A. S. Rasmussen, N. Kliem, and E. Kaas. The effect of climate change on the sea ice and hydrography in Nares Strait. *Atmosphere-Ocean*, 49(3):245–258, 1 Sep 2011. ISSN 0705-5900. doi: 10.1080/07055900.2011.604404.
- A. H. H. Renner, S. Gerland, C. Haas, G. Spreen, J. F. Beckers, E. Hansen, M. Nicolaus, and H. Goodwin. Evidence of Arctic sea ice thinning from direct observations. *Geophysical Research Letters*, 41(14):5029–5036, 28 Jul 2014. ISSN 0094-8276. doi: 10.1002/2014GL060369.
- C. Reyes-Hernandez and A. Valle-Levinson. Wind Modifications to Density-Driven Flows in Semienclosed, Rotating Basins. *Journal of Physical Oceanography*, 40(7):1473–1487, Jul 2010. ISSN 0022-3670. doi: 10.1175/2010JPO4230.1.
- P. A. Ryan and A. Münchow. Sea ice draft observations in Nares Strait from 2003 to 2012. *Journal of Geophysical Research-Oceans*, 122(4):3057–3080, Apr 2017. ISSN 2169-9275. doi: 10.1002/2016JC011966.
- R. M. Samelson and P. L. Barbour. Low-level jets, orographic effects, and extreme events in Nares Strait: A model-based mesoscale climatology. *Monthly Weather Review*, 136(12):4746–4759, Dec 2008. ISSN 0027-0644. doi: 10.1175/2007MWR2326.1.

- R. M. Samelson, T. Agnew, H. Melling, and A. Münchow. Evidence for atmospheric control of sea-ice motion through Nares Strait. *Geophysical Research Letters*, 33(2), 28 Jan 2006. ISSN 0094-8276. doi: 10.1029/2005GL025016.
- P. Schledermann. Notes on Norse finds from the east coast of Ellesmere Island, NWT. *Arctic*, 33(3):454–463, 1980. ISSN 0004-0843.
- J. A. Screen, I. Simmonds, and K. Keay. Dramatic interannual changes of perennial Arctic sea ice linked to abnormal summer storm activity. *Journal of Geophysical Research-Atmospheres*, 116, 4 Aug 2011. ISSN 2169-897X. doi: 10.1029/2011JD015847.
- H. Shibata, K. Izumiyama, K. Tateyama, H. Enomoto, and S. Takahashi. Sea-ice coverage variability on the Northern Sea Routes, 1980-2011. *Annals of Glaciology*, 54(62, 2):139–148, 2013. ISSN 0260-3055. doi: 10.3189/2013AoG62A123.
- E. L. Shroyer, L. Padman, R. Samelson, A. Münchow, and L. Stearns. Seasonal control of peterrmann gletscher ice-shelf melt by the ocean’s response to sea-ice cover in nares strait. *Journal of Glaciology*, 63:324–330, 2017.
- E. L. Shroyer, R. M. Samelson, L. Padman, and A. Münchow. Modeled ocean circulation in Nares Strait and its dependence on landfast-ice cover. *Journal of Geophysical Research-Oceans*, 120(12):7934–7959, Dec 2015. ISSN 2169-9275. doi: 10.1002/2015JC011091.
- S. D. Smith, R. D. Muench, and C. H. Pease. Polynyas and leads - an overview of physical processes and environment. *Journal of Geophysical Research-Oceans*, 95 (C6):9461–9479, 15 Jun 1990. ISSN 0148-0227. doi: 10.1029/JC095iC06p09461.
- G. Spreen, S. Kern, D. Stammer, and E. Hansen. Fram Strait sea ice volume export estimated between 2003 and 2008 from satellite data. *Geophysical Research Letters*, 36, 9 Oct 2009. ISSN 0094-8276. doi: 10.1029/2009GL039591.
- J. Stroeve, M. Serreze, S. Drobot, S. Gearheard, M. Holland, J. Maslanik, W. Meier, and T. Scambos. Arctic sea ice extent plummets in 2007. *EOS Trans. AGU*, 89(2): 13, 2008.
- J. C. Stroeve, V. Kattsov, A. Barrett, M. Serreze, T. Pavlova, M. Holland, and W. N. Meier. Trends in Arctic sea ice extent from CMIP5, CMIP3 and observations. *Geophysical Research Letters*, 39, 25 Aug 2012. ISSN 0094-8276. doi: 10.1029/2012GL052676.
- A. Thorndike. Sea ice thickness as a stochastic process. *Journal of Geophysical Research-Oceans*, 105(C1):1311–1313, 15 Jan 2000. ISSN 0148-0227. doi: 10.1029/1999JC900271.

- A. S. Thorndike and R. Colony. Sea ice in motion in response to geostrophic winds. *Journal of Geophysical Research-Oceans and Atmospheres*, 87(NC8):5845–5852, 1982. ISSN 0148-0227. doi: 10.1029/JC087iC08p05845.
- A. S. Thorndike, D. A. Rothrock, G. A. Maykut, and R. Colony. Thickness distribution of sea ice. *Journal of Geophysical Research-Oceans and Atmospheres*, 80(33):4501–4513, 1975. ISSN 0148-0227. doi: 10.1029/JC080i033p04501.
- A. Valle-Levinson. Density-driven exchange flow in terms of the Kelvin and Ekman numbers (vol 113, art no c04001, 2008). *Journal of Geophysical Research-Oceans*, 113(C5):C05025, May 2008. ISSN 0148-0227. doi: 10.1029/2008JC004853.
- A. Valle-Levinson, W. C. Boicourt, and M. R. Roman. On the linkages among density, flow, and bathymetry gradients at the entrance to the Chesapeake Bay. *Estuaries*, 26(6):1437–1449, Dec 2003. ISSN 0160-8347. doi: 10.1007/BF02803652.
- S. J. Vavrus, M. M. Holland, A. Jahn, D. A. Bailey, and B. A. Blazey. Twenty-First-Century Arctic Climate Change in CCSM4. *Journal of Climate*, 25(8):2696–2710, Apr 2012. ISSN 0894-8755. doi: 10.1175/JCLI-D-11-00220.1.
- Timo Vihma, Priit Tisler, and Petteri Uotila. Atmospheric forcing on the drift of Arctic sea ice in 1989-2009. *Geophysical Research Letters*, 39, 18 Jan 2012. ISSN 0094-8276. doi: 10.1029/2011GL050118.
- R. F. Vincent, R. F. Marsden, P. J. Minnett, and J. R. Buckley. Arctic waters and marginal ice zones: 2. An investigation of arctic atmospheric infrared absorption for advanced very high resolution radiometer sea surface temperature estimates. *Journal of Geophysical Research-Oceans*, 113(C8), 27 Aug 2008. ISSN 2169-9275. doi: 10.1029/2007JC004354.
- P. Wadhams. Sea-ice topography of the Arctic Ocean in the region 70-degrees-w to 25-degrees-e. *Philosophical Transactions of the Royal Society A-Mathematical Physical and Engineering Sciences*, 302(1464):45–85, 1981. ISSN 1364-503X. doi: 10.1098/rsta.1981.0157.
- P. Wadhams, A. E. Gill, and P. F. Linden. Transects by submarine of the east Greenland and polar front. *Deep-Sea Research Part A-Oceanographic Research Papers*, 26(12):1311–&, 1979. ISSN 0198-0149. doi: 10.1016/0198-0149(79)90001-3.
- K. Widell, S. Osterhus, and T. Gammelsrod. Sea ice velocity in the Fram Strait monitored by moored instruments. *Geophysical Research Letters*, 30(19), 4 Oct 2003. ISSN 0094-8276. doi: 10.1029/2003GL018119.
- G. J. Wong, E. C. Osterberg, R. L. Hawley, Z. R. Courville, D. G. Ferris, and J. A. Howley. Coast-to-interior gradient in recent northwest Greenland precipitation trends (1952-2012). *Environmental Research Letters*, 10(11), Nov 2015. ISSN 1748-9326. doi: 10.1088/1748-9326/10/11/114008.